UNIVERSITÀ
DEGLI STUDI
DI PADOVA

DIPARTIMENTO
DI INGEGNERIA
DELL'INFORMAZIONE

MASTER THESIS IN COMPUTER ENGINEERING

Decoding and analysis of EEG signals during the Motor Observation of robotic arm movements

JULY 13, 2023

MASTER CANDIDATE

Pietro Cimarosto

Student ID 2027173

SUPERVISOR

Prof. Luca Tonin

University of Padova

CO-SUPERVISOR

Prof. Gernot Müller-Putz

Technical University of Graz

ACADEMIC YEAR
2022/2023

Abstract

There are knowledge gaps in the state of the art on the topic of electrophysical neural activity correlated to the observation of movements, especially when coming to its application in brain-computer interfaces. In fact, recent studies showed that in the invasive domain, the neural activity during the observation of robotic movements during a reach-and-grasp task can be useful for enhancing the active control of the robotic device through the decoding of brain signals. Nevertheless, it is not clear how this principle translates to non-invasive brain activity measurement.

In order to fill this gap, I designed an experimental paradigm to explore how the observation of center-out target-oriented reaching movements performed by a robotic arm in the 2D plane are encoded in the brain electroencephalography (EEG). Moreover, the possibility of decoding the measured activity into movement-related information, being that the target of the movement or the kinematic state of the robot itself, was investigated through the design of a classification and a regression task. To solve the task, several approaches were followed, through features selection and the search for the best-performing machine learning models.

After measuring and analyzing the experimental data collected from the participants, what was found is that the EEG during the observation of the motor act shows time and frequency features that are known from the literature to be associated with the observation of movement, and that patterns characteristics of the direction of movement are present in the event-related de-synchronization (ERDS) in several phases of the action. Moreover, through the design of algorithms and custom models, it was possible to decode low-frequency EEG both in the classification and the regression task with accuracy significantly above the chance-level, proving that the neural activity measured non-invasively during a motor observation task encodes sufficient quantities of movement-related information for being applied in BCI systems. All this adds to the existing knowledge of the neural correlates of the observation of movements in the EEG, and could have a positive impact on the performance of EEG-based brain-computer interfaces for the neural control of robotic devices.

Sommario

Ciò che conosciamo del campo dell'attività elettrofisica neurale correlata con l'osservazione dei movimenti presenta delle lacune, soprattutto per quanto riguarda la sua applicazione nelle interfacce cervello-computer (BCI). Infatti, recenti studi hanno dimostrato che nel dominio invasivo, l'attività neurale durante l'osservazione dei movimenti robotici durante un'attività di reach-and-grasp può essere utile per migliorare il controllo attivo del dispositivo robotico attraverso la decodifica dei segnali cerebrali. Tuttavia, non è chiaro come questo principio si traduca nel contesto della misurazione non invasiva dell'attività cerebrale.

Per colmare tale lacuna, ho progettato un paradigma sperimentale per esplorare il modo in cui l'osservazione di movimenti center-out e target-oriented eseguiti da un braccio robotico nel piano 2D venga codificata nell'elettroencefalogramma (EEG). Inoltre, la possibilità di decodificare l'attività misurata in informazioni relative al movimento, siano esse il bersaglio del movimento o lo stato cinematico del robot stesso, è stata approcciata attraverso la progettazione di una task di classificazione e una di regressione. Per risolvere quest'ultime sono stati seguiti diversi approcci, attraverso la selezione delle caratteristiche e la ricerca dei modelli di machine learning più performanti.

Dopo aver misurato e analizzato i dati sperimentali raccolti dai partecipanti, è emerso che l'EEG durante l'osservazione dell'atto motorio mostra caratteristiche di tempo e frequenza che sono note in letteratura per essere associate all'osservazione del movimento, e che i pattern caratteristici della direzione del movimento sono presenti nella event-related de-synchronization (ERDS) in diverse fasi dell'azione. Inoltre, grazie alla progettazione di algoritmi e modelli personalizzati, è stato possibile decodificare l'EEG a bassa frequenza sia nella task di classificazione che in quella di regressione con un'accuratezza significativamente superiore al caso fortuito, dimostrando che l'attività neurale misurata in modo non invasivo durante un processo di osservazione motoria codifica quantità di informazioni legate al movimento sufficienti per essere applicata in sistemi BCI. Tutto ciò si aggiunge alle conoscenze esistenti sui correlati neurali dell'osservazione dei movimenti nell'EEG e potrebbe avere un impatto positivo sulle prestazioni delle interfacce cervello-computer basate sull'EEG per il controllo neurale di dispositivi robotici.

Contents

List of Figures

Introduction

The aim of this thesis work is to answer the questions that may arise from the knowledge gaps in the state of the art regarding non-invasive measurement of neural activity related to the observation of movement.

In the thesis, Chapter 1 gives an overview of the main concepts behind the measurement of brain activity and the application of brain-computer interfaces (BCI), proceeding then to introduce the neural correlates of the observation of movement. In fact, various studies explored the task of Movement Observation in the context of upper-limb reach-and-grasp actions of a robotic arm, through the measurement of electrophysiological signals in the invasive domain, i.e. with microelectrodes surgically inserted on the surface of the brain cortex. It was found that invasively-measured brain activity contained enough information to fit a model able to translate neuronal firing rates into kinematic controls for the robotic arm. Then, the model played the role of a starting point for gradually introducing the full neural control of the device through BCI. However, many well-known complications have to be taken into account within the information extraction process if the activity is recorded non-invasively instead, i.e. through sensors on the scalp, or in general external with respect to the head surface, for instance with the EEG. Therefore, it is not clear if the aforementioned principles and results could apply in the same way in the non-invasive domain.

To answer that, with the help of the Institute of Neuroengineering of the TU Graz, I designed an experimental paradigm for investigating the neural correlates of the observation of center-out target-oriented movements performed by a JACO robotic arm in the 2D plane. 15 human participants took part in the experiment and provided experimental data as EEG measurements. The data was processed through a sophisticated pipeline to obtain clean signals where the effects of artifacts and eye movements were attenuated or removed, then the effects of the observation of movement were investigated through the analysis of the event-related de-synchronization (ERDS) and through the design of two decoding tasks, namely a classification task where the EEG trials were classified into their respective movement's target code, and a regression task where EEG readings were decoded sample-by-sample into the kinematic state of the robotic hand at the sampling time instant, defined as a 2D position and a 2D velocity vector. All the details of the experimental paradigm and the instrumentation, the processing pipeline, the models and algorithms used, and the performance measures adopted are described in Chapter 2 of the thesis.

The results of the three analyses (ERDS patterns, classification task and regression task) are provided in Chapter 3, and are analyzed and discussed in Chapter 4: what has been found is that the "mu-suppression" phenomenon, well-described by the literature as occurring during the observation of movement, is present during the observation of our robotic motor act in a predictable way, but also it shows patterns that are specific for the target the action was directed to. Regarding the classification task, it has been shown that the low-frequency component of the EEG trial could be restricted to informative time windows that give the best classification accuracy using simple models. For the regression, custom models were designed to improve the performance of the state of the art in the decoding of the multi-dimensional kinematic state of an observed robotic hand from the low-frequency EEG, showing that under the constraints dictated by the scarcity of data and limited computational capabilities, the found solutions still brought enhancements in 62.5% of the performance indexes.

Lastly, the Conclusion summarizes this study's findings, focusing on describing the limitations that affected the experimental sessions and the analyses and providing insight into possible improvements and applications to be introduced in future works.

CHAPTER 1

State of the art

This chapter aims to give an overview of the methods and processes behind the measurement of brain activity, as well as the significant progress, carried out during the last decades, of their decoding for the control of robotic devices.

The first section introduces the measurement and collection of brain signals, including the nature of the signals collected by the main state-of-the-art techniques for measuring cerebral activity, and specifically Electroencephalography (EEG). The EEG is further explored to investigate the path from the bioelectrical source to the digital representation. The section successively describes the details of patterns and features of the EEG signals, the processing steps to obtain them, and how they are exploited in the field of Brain-Computer Interfaces (BCIs). Finally, it contains a brief introduction to the basics of non-invasive BCI.

The second section describes how EEG signals encode the observation of movement, which is one of the focal points of the thesis. This includes the variables that have an impact on the representation of such content, and how the representation itself has to be interpreted.

The third section narrows the attention to a particular aspect of the representation, namely kinematics, such as position and velocity, of an observed movement.
In the fourth section, the discussion shifts away from the observation of movement to explore the application of continuous EEG decoding for BCI control. There, details are provided regarding how the encoded information that was largely investigated in the previous section can be actively used to provide control on external devices. The fifth and final section explains the motivation behind this thesis, building upon the principles explored in the previous part and the knowledge gaps that were revealed as a result.

1.1 EEG and BCI

1.1.1 Measuring brain signals

The activity of the brain is a complex orchestration of electrochemical reactions associated to neurons in the cortex and other areas of the nervous system. At cellular level, the process is caused by the flow of Potassium, Chloride and Sodium ions managed by cell gates, and by the accumulations or discharges of electrical current that derives from them. These events take place at the so-called *source level*, where by *source* we mean the single *discharging* neuron. The electrical field generated with the discharge is in the order of tens of microvolts, it has a duration of less than a millisecond and propagates from the sources through the surrounding tissues, the skull bones and the scalp [20]. Signals can be measured at different levels and with several technologies and methods. Indirectly, they can be measured as changes in blood oxygenation level through fMRI (functional Magnetic Resonance Imaging) or NIRS (Near-Infrared Spectroscopy), or as emission of radioactive material with PET (Positron Emission Tomography). Directly, as electrical fields at different levels, — invasively and non-invasively. Invasively, ECoG (Electrocorticography) is a way to measure charge spikes through arrays of microelectrodes inserted into specific areas of the brain cortex through a surgical procedure. Non-invasively, the activity of groups of neurons can be measured at the scalp with MEG (Magnetoencephalography) or EEG (Electroencephalography) as, magnetic or electric fields respectively [37].

EEG

EEG is a completely non-invasive procedure that can be applied repeatedly to patients, normal adults, and children with virtually no risk or limitation. It measures in real time the brain activity produced by large populations of active neurons, and specifically pyramidal neurons positioned perpendicular to the cortex, that are able to generate electrical activity intense enough to be recorded on the head surface. The so-called action potentials from individual neurons would be too small and have too high frequency to be detected by the EEG. However, when many neurons fire action potentials simultaneously, their collective activity is strong enough to penetrate through skin, skull and neural tissues and be detected in EEG recordings. The weak electrical signals detected by the scalp electrodes are then massively amplified and displayed [20] [61].

Electrodes allow measurement of potential changes between active electrode and a reference (REF) electrode, the ground (GND) electrode is needed to reject any common-mode noise that might be present in the EEG (e.g., powerline interference). Active channel configurations can span from the simplest possible configuration with only one active electrode, to more complex ones with 128 to 256 of them. Noninvasive electrodes themselves can be of different types: disposable (gel-less, and pre-gelled types), reusable disc electrodes (gold, silver, stainless steel or tin), saline-based electrodes, headbands and electrode caps. The second one is the most common, with Ag-AgCl reusable discs connected by a cabling system to the amplifier. For these types, a conductive electrolyte gel is applied between the electrode and the skin, serving as media to ensure the lowering of contact impedance at the interface to acceptable levels, typically around $5 - 20k\Omega$ [61].

It should be mentioned that in the last decades, dry electrodes have undergone a remarkable development: they require no special preparation of the subject and are simply placed on the scalp [9]. Di Flumeri et al. [15] conducted a performance analysis on different types of dry electrodes, comparing traditional Ag-AgCl disc wet electrodes to three types of dry electrodes: active gold-coated single pin electrodes, hybrid multiple-spikes based electrodes and passive solid-gel based electrodes, showing interesting results regarding signal measurement accuracy and comfort compared to wet electrodes. Nevertheless, the gap between the two is not closed yet, hence the latter type is still being considered the gold standard by the scientific community for its reliability, and is vastly employed in

EEG research worldwide.

When estimating the relationship between functional activity and regions of the brain, the montage — the general configuration of electrodes — plays an important role. EEG is not able to directly indicate the location of the active neurons in the brain due to the ambiguity of the underlying static electromagnetic inverse problem [37]. Uniform spacing of 2-3 cm seems to be the best choice to avoid distortions of the scalp potential distribution caused by spatial aliasing, which is a side effect of the attenuation by the skull's "low-pass filtering" effect. It has also been shown that a minimum of 128 sensors is necessary to adequately sample the human EEG across the complete surface of the head, and cover the full range of spatial detail in the brain's electrical fields at the scalp [59]. Moreover, there is a nonlinear relationship between the number of electrodes and the source localization precision, increasing from 25 to around 100 electrodes and then reaching a plateau, suggesting that in practice a fairly good level of accuracy in source localization can be already obtained with 60 evenly-spaced electrodes [37].

The electrodes' signals need to be amplified to make them compatible with devices such as displays, recorders, or A/D converters. Amplifiers that are suitable to measure these signals have to satisfy very specific requirements: they have to provide amplification selective to the physiological signal, reject superimposed noise and interference signals, and guarantee protection from voltage and current surges for both patients and electronic equipment [5].

A successive crucial step in the acquisition of information from the brain's activity is the conversion of the measured electrical analog signals, sampled at a constant sampling rate, to a digital representation to be handled by computers and other devices. This is achieved through devices known as A/D converters, which are characterized by a resolution and a sampling rate.

1.1.2 Processing brain activity

After having acquired signals from the brain, the next step is to apply digital signal processing techniques to transform the signals and facilitate the extraction of useful information.

Filtering

Digital filtering can be applied to the output of the previous stage using more refined computational techniques, applying for instance Finite Impulse Response (FIR) or Infinite Impulse Response (IIR) to remove unwanted parts of the signal. Generally, a filter is a “pass-through” function that is characterized by an order, i.e. for an input, the number of previous input lags used to calculate the current output, and an impulse response or transfer function that describes the input-output relation. The filtering step in EEG systems is very important, and understanding the process behind it is necessary to choose the best type of filter depending on the objective and the requirements. In fact, in many cases, pass-band filtering is performed to select specific frequency bands of interest (e.g., in sleep patter analysis or motor tasks) to discriminate components associated with certain brain events, for example in sensory-motor rhythms-based BCI, sleep pattern analysis, or in general to discriminate components associated with certain brain events. A further trade-off for which such signal processing knowledge is necessary is the transition from offline to online EEG decoding: the delay added by the wrong choice of filter may become non-negligible and affect the usefulness of an application. It is the case of Mondini et al. [38], where the type and order of each filter added a delay that was necessarily taken into account to synchronize EEG, visual stimuli and robot movement to realize online control.

Event and pattern selection

Knowing the task we aim to accomplish, well-known patterns and peculiarities in the EEG signals can be exploited for feature selection, analysis and decoding. This can be done either in the time, frequency, or time-frequency (e.g. wavelet) domain, and these patterns can be either spontaneous or evoked by certain stimuli. All of these types are frequently employed in EEG applications and analyses, especially in BCIs.

Spontaneous EEG The activity that goes on permanently in living individuals can be measured by the EEG, lying in the range of 75 to 100 microvolts, with frequency content approximately between 1 and 40 Hz (in some cases, also up to 100 Hz). The dynamically changing connectivity gives origin to short-lived oscillations at frequencies that favor different types of connections and different levels of computation. These are classified into smaller functional bands, specifically Delta (from 0.5 to 4 Hz), Theta (from 4 to 8 Hz), Alpha (from 8 to 12 Hz), Beta (from 12 to 30 Hz) and Gamma (over 30 Hz). Spontaneous brain rhythms can be time-locked to an event but are never phase-locked, therefore it is not possible to extract meaningful information by directly analyzing them after averaging the EEG over trials. This "oscillatory loudness" feature in the EEG can be rather easily quantified by Fourier analysis and constructing the power spectrum of the signals. Then, comparing the power during activity with the one during rest it is possible to construct the so-called Event-Related (de)synchronization (ER(D)S) time-frequency map [40] [7].

Event-related potentials An ERP is «a transient wave complex elicited by a certain stimulus or event that is repeated only once» (Regan et al. (1989) in [40]), its effect is independent of the previous stimuli and is reliable if the stimulus is submitted during a resting condition. ERPs are time- and phase- locked, therefore averaging presentation-response trials increases SNR and allows their detection. There are different types of ERPs

- Evoked Potentials (EP) by stimulation through perception and sensory stimuli. They are divided into types depending on the set of senses employed (visual, auditory, somatosensory), resulting in different shapes of wave responses and location of appearance.
- Error-related Potentials (ErrP) are caused by the acknowledgment of an incorrect stimulus that mismatches expectation. They may have different shape depending on the underlying process of error.
- Steady-state EPs (SSEP) are caused by «a sensory stimulus delivered at a sufficiently high rate so that relevant neuronal structures are prevented from returning to a resting state» (Regan et al. (1989) in [40]). This results in EEG oscillations with the same frequency as the stimulation frequency.

1.1.3 Brain-Computer Interfaces

Brain signals that are measured with the techniques mentioned at the beginning of the chapter can be exploited for several purposes through a so-called BCI (or BMI, Brain-Machine-Interface). These are systems that translate information encoded in the activity of the central nervous system into artificial outputs such as commands and actions to restore, replace, enhance, supplement or improve the nervous system's output, but also modify the interaction between the latter and the environment [69].

In general, BCI systems can be classified into the ones that exploit "externally triggered" features of any type, and are therefore called “cue-based” or “synchronous”, and systems that continuously analyze signals to detect event-related potentials or transient changes that are called “noncue-based” or “asynchronous” BCI systems [49].

The design of a BCI system can be partitioned into the design of solutions for each of three stages:

- Measurement of signals reflecting the brain's activity using one or more methods from those discussed in Subsection 1.1.1 to extract intent.
- Activity processing and feature extraction, starting from the measured activity the aim is to manipulate and analyze the signal to extract the relevant information in a compact representation. This is done, for instance, through space and frequency filtering and time/frequency analysis as described in Subsection 1.1.2., usually including an artifact rejection step as well. Specific features can be selected according to different strategies: evaluating the direct relationship between a feature and a target evaluation measure (filter approach) or with the aid of an ad-hoc built model to select a subset of features (wrapper and embedded approaches) [33]
- Feature translation or Decoding, from the extracted information to the correct output corresponding to the intention that was encoded in the measured signals. It may include advanced techniques such as machine learning, deep learning, artificial intelligence and control strategies.

BCI outputs can be classified into the ones to select goals (goal-selection protocol) and the ones to achieve goals (process-control protocol). In the first case the user sends the "intent" which is managed by a software or an application that ensures the achievement of the goal. For example, sending a location command to a wheelchair software that autonomously handles path planning and obstacle avoidance to reach it. In the second, the user produces continuous commands to manage all details of the intent to reach the goal. In the same example, the user rather sends continuous x and y trajectories or "break" and "turn" commands to drive the wheelchair.

The difference between the two, when designing a BCI system, is a tradeoff in the demands and effort put on the user, rather than on the BCI (and vice-versa) when decoding the intention: the first option allows to easily and reliably reach a finite set of goals or commands, the second option offers more adaptivity to unexpected conditions and a higher degree of control. Nevertheless, this does not rule out the possibility to combine the two types of process into a single decoding processes to enhance the BCI's rapidity, reliability and ease of use [69].

Fundamentals in feature selection from EEG Restricting to the EEG as measurement system for the first stage, several types of BCIs have been designed in the past years exploiting the features described in Section 1.1.2. For instance, one of the first BCIs used Evoked Potentials' so-called P300 component to select the "goal" i.e. the desired letter of a keyboard when it flashed [49]. P300 component is «an indicator of information processing in relation to attentional and memory mechanisms» [40] defined by a positive peak of activity 250-300 ms after the presentation of the stimulus, further divided in P3a (250-280 ms, frontal and central areas) and P3b (250-500ms, midline parietal areas) [16] [23] [57]. ErrP is also commonly employed in discrete and continuous BCI control for error detection and correction or inhibition of erroneous outputs, thanks to a distinguishable component appearing on the frontal midline, defined by a negative peak within 100-500 ms after the onset of the erroneous stimulus [40] [10] [22] [29]. Evoked Potentials of the MRCP type (Movement-related Cortical Potential) are also used thanks to the high amount of motor information they carry. They consist of a negative component emerging from 1.2 s before an executed or imagined movement onset, in regions related to the type of movement within the motor and sensorimotor areas [40] [35].

Regarding spontaneous brain activity, it is easy to recognize its potential as information carrier for BCI applications. One of the first strategies built around it included the pairing with Motor Imagery (MI) tasks: this involves the same mental rehearsal of a motor task but without its execution, and the extension of it to include the latter would represent Motor Execution (ME) [40]. They realize an efficient way for a user to voluntarily modulate brain rhythms to communicate information and intention of movement [55] [63] [42].

Decoder models for BCI Regarding the decoding part, state-of-the-art BCI decoder models are based on machine learning and require two phases: an offline calibration necessary for reliable performance, and an operational online test. Working with a goal-selection protocol or a process-control protocol reflects on the type of model to be implemented, which will be either a binary/multi-class classifier or a regression model.

The most common machine learning classifiers used in the BCI literature are linear classifiers such as Linear Discriminant Analysis (LDA) and Support Vector Machines (SVM), neural networks (NN) such as Multi-Layer Perceptron (MLP), non-linear Bayesian Networks like Hidden Markon Models (HMM), Nearest Neighbour classifiers and Decision Trees or Random Forests.

These models can map manually selected features in a finite set of classes but alternatively, avoiding feature selection, it is possible to rely on Riemannian Geometry Classifiers (RGC) with different manifolds. More complex models can be used for automatic feature selection based on transfer learning or deep learning. With transfer learning the model inherits knowledge acquired while learning a given task for solving a different but related task. With deep learning, the model learns both the features and the classifier weights. State-of-the-art deep learning models in BCI binary classification tasks include Restricted Boltzmann Machine (RBM), Convolutional NN (CNN), Recurrent NN (RNN), Extreme Learning Machines (ELM), Deep Belief Network (DBF) and Autoencoders (AE) [33] [21].

Expanding from the domain of binary classification, multi-label classification can be tackled in two ways: either directly for those architectures that allow it (decision trees, multilayer perceptrons, naive Bayes classifiers or k-nearest neighbors) or decompose it in several binary classifications based on strategies like one-vs-all, one-vs-one or others [33].

At last, switching from classification to regression is more complicated, as it requires the prediction of a numerical value, virtually extending the binary-to-multiclass adaptation to a theoretically infinite number of classes, that is the subset defined by the set of real numbers. While this invalidates the decomposition approach from the binary-to-multiclass adaptation, some model architectures can still be directly re-structured to generate a suitable output, and further refined toward regression with specific techniques. This is the case of Linear and Polynomial Models, Decision Trees, SVM, NN and DNN (Deep Neural Networks e.g. CNN and RNN). As an alternative approach, some models are specifically designed for regression, such as the Kalman Filter (KF) and its variations (Extended Kalman Filter - EKF - and Unscented Kalman Filter - UKF): they take advantage of the past state and the current measurement to predict the current state in the $\mathbb{R}^N$ domain, providing very solid performances for continuous and online state-space decoding.

1.2 Observation of movement in EEG

Proceeding now to investigate the neural correlates of observation of movements, it can be said that the process of understanding an action requires a mixture of perceptual, motor, and memory processes [64]. Results have been found that link observation of movement with activation of the human mirror-neuron system (hMNS), i.e., a complex of neuronal structures located between the inferior frontal, the superior temporal and the anterior intraparietal areas of the brain. In monkeys, activation of the mirror neuron system is associated with observation of object-based actions (such as pinching), but not of motorically equivalent movements that are not directed to an object (e.g., an empty pinching movement without an object present) [17] [50] [39].

In humans, execution and observation of movement elicit suppression of alpha rhythms over the sensorimotor and occipital cortex [34], a phenomenon called "mu suppression", usually reflecting ERD relatively to a motor task. This refers to oscillations in the mu band, that are in the same frequency range of the alpha band but with different location and functional significance, with the alpha rhythm typically observed in the occipital region during relaxation, and the mu rhythm observed in the sensorimotor cortex during motor planning and execution.

Mu suppression is observed differently in certain electrodes, at certain sub-bands depending on the observer's viewpoint (allocentric vs egocentric — viewing the action from the front vs from the back). Specifically, ERD within the mu band is different in lower alpha (8-10 Hz) and upper alpha (10-12 Hz): in the lower alpha EEG desynchronizes both for executed and observed, in the second only the execution condition shows this effect. Suppression is also observed in the theta range (4-8 Hz) and it is more prominent during observation of hand movement with respect to non-biological movement. Furthermore, suppression in alpha with respect to rest showed to be dominant in posterior parietal and occipital regions (where alpha rhythms are known to be more commonly appearing), whereas the difference in suppression magnitude between observation of biological and non-biological movements is located mostly in the frontal and central areas (reflecting the link between mu-rhythms and the hMNS) [6]. Regarding the hemispherical-specific localization of mu suppression, literature shows inconsistent results, while, regarding the viewpoint, suppression showed to be stronger in the allocentric than egocentric viewpoint [17].

It has been observed that mu suppression is stronger when a precision grip is observed rather than an empty movement. This is further accentuated if the grip is oriented towards an external object (effector-object interactions), as the parietal lobe shows strong somatotopically organized activation for object-targeted actions, that also depends on the effector used [6]. Still, the fact that suppression happens at a lesser degree if the object is not present, represents a significant difference with the monkey motor neuron behavior, which does not fire at all in that condition [39]. Therefore it is possible to state that human sensorimotor mu rhythm is associated with activity in a human brain system that has functional similarities with the monkey mirror neuron system [39].

Considering the multispectral nature of the mu rhythms, effects of observation of hand movement and grasp types have been observed not only in the alpha band, but also in the lower and upper beta bands: this includes desynchronization as soon as the observed movement starts until 400-600 ms after its termination. The desynchronization is followed by a power rebound that differs between the three said bands, following the same difference pattern as of executed movement. This validates further the contribution of the mirror mechanism in transforming the observed motor act into a motor pattern. Greater beta band modulation in this context was observed in parieto-central areas. Furthermore, the primates' mirror neuron codes the target of the movement, but it is apparently not sensitive to the kinematics of the observed motor acts. Differently, the hMNS also responds to the velocity profile of single movements [1].

Regarding the movement velocity, it has been observed that increasing the speed, hMNS has maximum activation (in terms of mu suppression) at moderate level, then decreasing and stabilizing. This happened when the inter-stimulus interval (ISI) fell into the limit of 360–2,000 ms suggested for accessing visual short-term memory and activate visual–spatial attention [34] [12] [4].

At last, it is not straightforward to state if the aforementioned principles could or not extend from the observation of human movements to the observation of robotic movements, and many variables are accounted for the human perception of movement [43]. It has been demonstrated that everyday object manipulation actions performed by a robot, including reaching and grasping, induce mu suppression with and without target objects, and in general, effects in the mu band non-significantly distinguished from the ones evoked by the same human actions [43]. Moreover, the contribution of memory in the recognition (and therefore, perception) of action can be investigated through theta oscillations in frontal areas. Whereas cortical mu oscillations are not modulated by the human likeness of the observed agent, theta rhythms at frontal and central sites showed to have significantly increased power during the observation of robotic movements compared to the observation of android or human ones. This suggests that observing robot movements has higher demands on memory systems compared to observing the same movements performed by a human or an android, possibly due to increased difficulty in the mapping between visual perception and the semantic representation in the memory [64].

1.3 Decoding kinematics of observed target movements from the EEG

We now focus on how the kinematics of a hand or cursor movement are encoded in the brain's activity during its observation.

Such topic has been explored in a study by Clanton [11], where the kinematic and dynamic BCI control of a robotic arm was achieved. Two monkeys were provided with the possibility to control 7 degrees of freedom (DoF) of a robotic arm by recording invasively their brain activity in a target-oriented reach-and-grasp task. A decoder model was designed to convert neuronal firing rates into a 3D translation and a 3D rotation, eventually adding the grasp action to fulfill the 7 DoF of control of the robotic device. The decoder used a Preferred Direction (PD) model paired with a Population Vector Algorithm (PVA) for prediction, and it was fitted during a first "movement observation phase" where the monkey observed the movement of the robotic arm as it autonomously reached the target, through a two-steps succession of a 3D translation and a 3D rotation, from a starting position to the target position. Both position and orientation change at each trial, with the start selected from 6 possible orientations at the center of the workspace and the target from 6 possible locations in the workspace. Each reach-and-grasp trial was defined by: 1) the monkey pressing a button to start the trial, 2) presentation of starting positions, 3) audible cue (start of the movement), 4) hand opening, 5) reach movement (linear translation toward the target), 6) orienting movement (rotation of the robot hand with no translation), 7) target approximation, 8) grasp. The monkey received a reward if the task was completed successfully — the target was grasped correctly. While the monkeys' natural arms were constrained, anthropomorphic configuration of the arm joints and links, as well as horizontal mounting, were adopted in the experiment to approximate the joint configuration of the primate shoulder and match natural subject movements.

The decoder model links linear and rotational velocities of the hand to firing rates of individual motor neurons with the linear relation defined by the PD model, it is trained in the observed movement phase through Optimal Linear Estimation (OLE) at the beginning of each session, gradually increasing the amount of direct neural control through a Bimodal Shared Control (BSC) system to reach full BCI control of the 7 DoF robot movement. The Observation-based model calibration is fundamental for setting the weights of the PD model by taking advantage of the mirroring phenomenon described in the previous section. Separation of the action into movement types (translation and rotation) was important to discriminate the correspondence between a specific type of movement and its cortical representation, in terms of firing rates, from those of other types of movement. Also, it resulted in an easier model fitting, requiring fewer trials, and it made the task easier to understand and accomplish.

A similar approach, extended to 7 DoF by Clanton, was previously adopted by Velliste et al. [66] for neural control of a robotic arm in 3D translation and 1D grasp, employing an observation-based model calibration at the beginning of the experimental session with the monkey observing automatic task performances. Extending such results to humans, Collinger et al. [13] achieved online control of a robotic arm through invasive neural recording of a participant affected by tetraplegia. The subject progressively achieved control of all 7 degrees of freedom of a robotic prosthetic to accomplish reach-and-grasp tasks and even complex object manipulation tasks. Similarly, the decoder was based on a linear model to map the relationship between firing rates and robot velocities and was calibrated through a daily observation-based phase before introducing direct neural orthoimpedance-assisted control.

At last, noninvasive decoding of kinematics from human subjects gave proof that low-frequency EEG (LF-EEG) in parietal and occipital areas contain enough information to allow the decoding of directional information of hand movement [67] [3], and position and velocity of an observed cursor moving in the 2D plane. Such information can be decoded from the LF-EEG using a Partial Least Squares (PLS) regression, Kalman Filter (KF) or Unscented Kalman Filter (UKF), eventually adding to the latter the ability to use non-directional kinematics. Correlation and SNR of the decoded kinematics with respect to the true ones were lower for the observation condition compared to the execution condition, coherently with the conclusions from the previous section. Therefore, LF-EEG encodes information about the instantaneous target position and velocity, the second at a lesser degree with respect to the execution of the movement in fronto-central and sensorimotor regions, and further non-directional kinematics such as distance and speed of the movement in parietal and occipital regions [24] [26].

1.4 BCI control of robotic devices through EEG decoding

Kinematics of a robot movement passively observed can be decoded from the observer's EEG, but the other way around is also possible, leading to active control of a robotic device through decoding of movement intention. The feasibility of such application has already been proven in the invasive BCI domain by the studies of Velliste et al., Clanton and Collinger et al. reported in the previous section [66] [11] [13], where to an observation-based calibration succeeded a gradual introduction to the active control of the robot's degrees of freedom.

In general, controlling movements of external robotic devices with EEG requires the subjects to perform motor imagery (MI), motor execution (ME) or motor attempt (MA) task, decoding the related cortical activity into robot commands [49]. As largely argued in the previous section, activity in mu and beta bands in sensorimotor and parieto-occipital areas is highly informative and can therefore be used together with these types of tasks. Alternatively, low-frequency (LF) EEG can be used for the detection of movement intention in the form of Movement-Related Cortical Potentials (MRCPs), — neural correlates of movement planning and execution that are characterized by a slow negative inflection that is time- and phase- locked to the movement onset, and can be useful in self-paced movement decoding [47] [48]. On top of that, LF-EEG itself inherently encodes movement direction [67] [3] [24] [44] and amplitude [26] that can be extracted for center-out ME, MI and MA tasks.

Nevertheless, online decoding for continuous control is more complicated than offline decoding, due to its closed-loop nature and due to the effects of mutual decoder-subject learning and brain plasticity [38] [49] [52] [53]. Many more factors need to be taken into account: the type of paradigm, that needs to be suitable for online control, the delay of the feedback effect, and the strategy to achieve full neural control, which has to be gradually introduced both to avoid subject stress and fatigue and to adjust the decoder model's parameters smoothly. If the necessary attention to all details is provided, closed-loop BCI control or robotic devices is feasible even in motor-impaired subjects with a high degree of accuracy [38] [53] [36] [41].

Even further, aiming for a more "natural" BCI control is often desirable, putting aside body and eye movement constraints that are usually adopted to avoid lowering of SNR in the EEG signals. A common practice is, in fact, to force a participant to fixate the sight toward a specific point to avoid blinks, saccades and effects of visual processing that could overshadow features of interest, and also restrict head and body movements to avoid heavy artifacts. The recent development of techniques that, if added to the artifact rejection step, allow these otherwise possibly problematic actions have had a great impact on the path toward a more natural BCI control [27] [56] [28] [25].

1.5 Motivation of the work

In the previous sections, it has been established how the observation of movement is encoded in the brain's activity, and how important it is for building a base to reach high-performance BCI control of robotic devices. The operations and variables to account for during the translation from intention to commands were also explained, with a particular focus on how they change when switching from offline to online control.

In this context, some knowledge gaps start to appear: in the study of Collinger et. al. the extension of Clanton's results from the monkey to the human was investigated successfully, in a restriction to the invasive domain. But how does this translate to the non-invasive domain? How does EEG encode observed center-out translations performed by a robotic arm? Then regarding the state-of-the-art BCI control of robotic devices with EEG decoding, in the recent studies of Mondini et.al. and in general of the Feel Your Reach ERC Project [41], an observation-based calibration has never been considered. Would such a component, if added to the pipeline, increase the performance of EEG-based BCIs? In this thesis, I try to answer these questions. With the help of the research team of the Institute of Neuroengineering of the Technical University of Graz, I designed an experimental paradigm for investigating the observation of target-oriented center-out movements performed by a robotic arm with EEG. I collected the EEG data of 15 participants and analyzed it to study the neural correlates of the observed movements, and designed a decoder model to detect the target of the movement and reconstruct the robotic arm's observed kinematics from the EEG.

The results of this study could hopefully provide meaningful insight into the explored topics and build a link between different but affine studies in the literature, aiding the progress toward new solutions and better performance in non-invasive BCI control of robotic devices and prosthetics.

CHAPTER 2

Materials and Methods

An experiment was designed to collect data from human participants performing the specific task of observing the movement of a robot, in order to explore its neural correlates. Such data was elaborated, analyzed and decoded using several techniques of signal processing, machine learning and statistics. The purpose of this chapter is to give a detailed overview of these techniques and their involvement in the steps from the design of the experimental paradigm and the collection of bioelectrical signals, through the elaboration workflow resumed by Figure 2.6 to extract the useful components of the signals, to the decoding of external information that is there inherently represented.

The content of this chapter is based on and influenced by the concepts presented in Chapter 1, and provides an overview of the methodologies used to produce the findings presented in Chapter 3 and discussed in Chapter 4.

2.1 Experimental setup and paradigm

2.1.1 Participants and setup

The participants in the study were 15 healthy people of age 22.85±3.67 with an outlier of age 56. All participants were right-handed and had normal or corrected-to-normal vision, eight were females and seven were males. They will be referred to as FK1, FK2, FK2, FK4, FK5, FK6, FK7, FK8, FK9, FL1, FL2, FL3, FL4, FL5, FL6. All participants gave their written informed consent to take part in the study. The experimental procedure conformed to the Declaration of Helsinki and was approved by the ethics committee of the Medical University of Graz.

The workstation is shown in Figure 2.2 and consisted of a desk supporting a screen (LG Smart TV) and a JACO robotic arm (Kinova Robotics) mounted on the desk between the participant and the screen. JACO had 6 DoF: One frame/base rotation joint, one shoulder joint, one elbow joint, three rotation joints for the wrist. 7 DoF could be considered if fingers were included, which was not the case of this paradigm. The participant was seated on one side of the desk facing the screen, from an egocentric viewpoint with respect to JACO.

To record the data, 64 active EEG electrodes (actiCAP Brain Products GmbH, Germany) were placed on the scalp according to the 10–10 system (Figure 2.1). The reference and ground electrodes were placed at the right mastoid and AFz, respectively. Four additional active electrodes were positioned at the inferior, superior and outer canthi of the left eye and to the outer canthi of the right eye to record the electro-oculographic signals (EOG). Electrodes 54 and 55 were placed in the parieto-central area to increase the spatial resolution in the area of interest, specularly in both hemispheres with respect to the central sulcus, one (CPP1h) at the midpoint of CPz, CP1, Pz and P1, the other (CPP2h) at the midpoint of CPz, CP2, Pz and P2. The EEG and EOG signals were recorded at a sampling rate of 200 Hz through biosignal amplifiers (BrainAmp, Brain Products GmbH, Germany).

The custom scripts for the paradigm, the pre-processing phase and the processing phase were developed in Matlab (Mathworks Inc. USA, mainly Versions 2019b and 2022b). The presentation of stimuli made use of Psychotoolbox for Matlab. The data was recorded and synchronized through the lab streaming layer (LSL) protocol, implemented in Matlab.

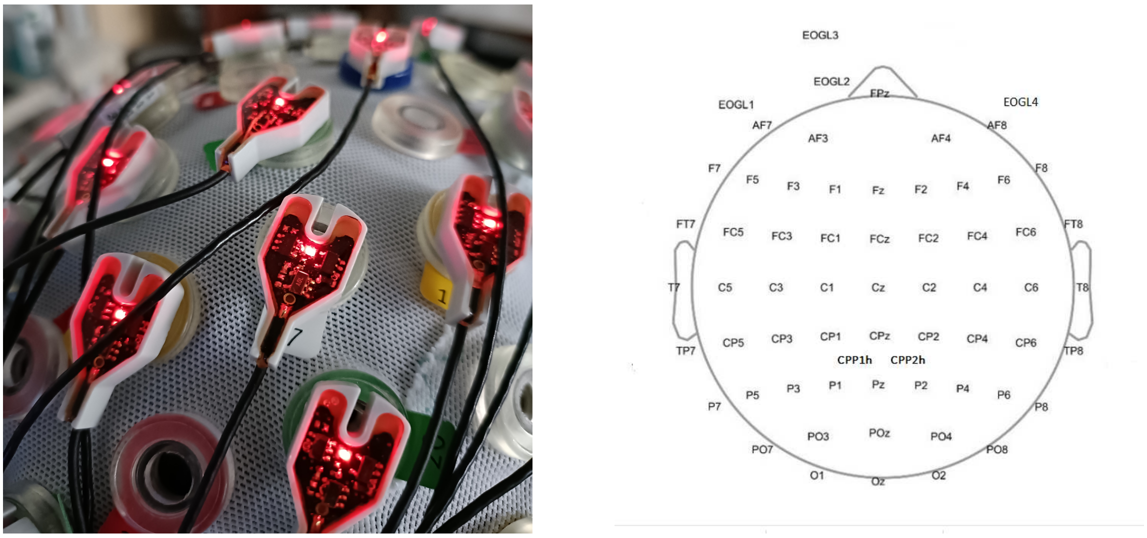

Figure 2.1: Left: Detail of the active actiCAP electrodes used in the measurements of EEG; Right: labeled placement of electrodes on the scalp

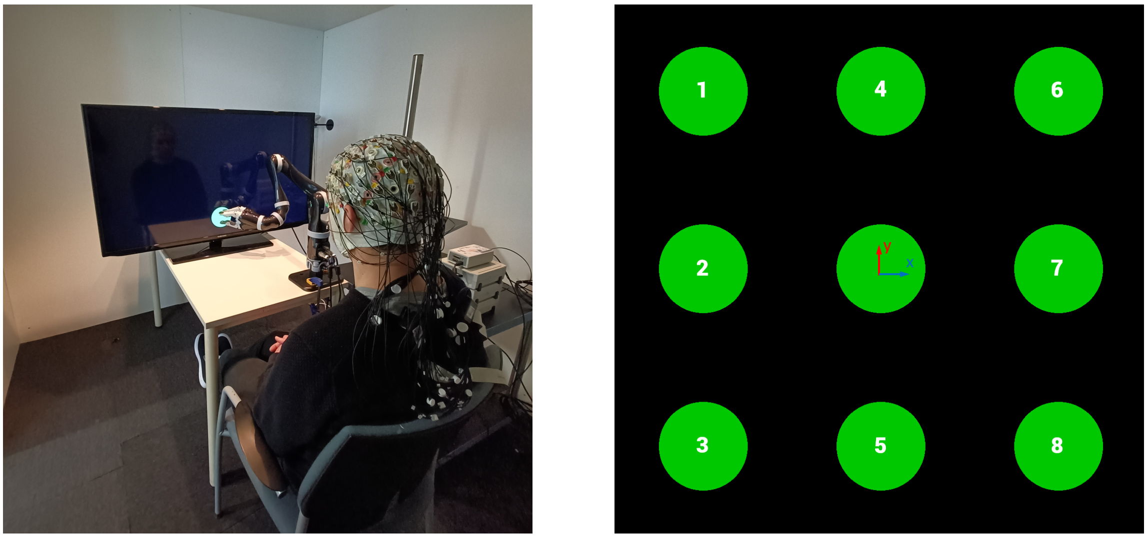

Figure 2.2: Left: Workstation and configuration of the participant-setup environment during a *robotrun*; Right: target enumeration in the paradigm

The duration of an experimental session was 4 to 5 hours, consisting of several steps. After a first briefing with an introduction to the task and the setup, the handedness test and the rest of the documentation were submitted. The system setup included placement of the EEG cap, application of the conductive electrolyte gel, entrance in the box and placement in the workstation, plugin to the rest of the system, impedance and signals check. After the EEG was visually checked, and the subject was ready and in place, the actual recording could be started, lasting approximately two hours.

Recording runs were of two types: *eyerun* and *robotrun*, whose detailed structure will be explained later. In the first run of each type, the participant was instructed on the paradigm, and could briefly see it in action without the EEG being recorded to get familiar with the task. At the end of each run the participant could choose to rest as long as desired (generally not more than some minutes). The sequence of the recording runs is depicted in Figure 2.3 and consisted of: 1) First *eyerun*, 2) First subsequence of six *robotruns*, 3)Major break, in which the subject was unplugged from the system and could exit the workstation to walk around for some minutes, 4) Second *eyerun*, 5) Second subsequence of six *robotruns*, 6) Third *eyerun*.

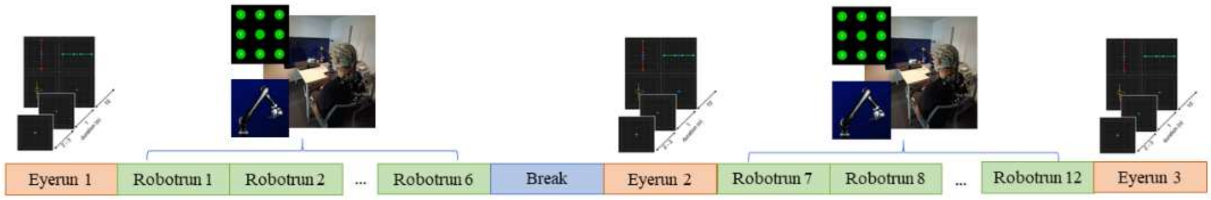

Figure 2.3: Schematic representation the sequence of *eyeruns* and *robotruns* that composed an experimental session.

2.1.2 Paradigm

The experimental paradigm of the *robotruns* implemented a motor observation (MO) task. At the beginning of each run, JACO's configuration was set to the initial position, defined in the joints space to have JACO with the hand at the center of the screen. The screen was positioned perpendicularly to the robot, at 5 cm from its fingers at the initial configuration.

At this point, the trials started: each run was structured in 24 trials, at the beginning of each trial the target is randomly selected between the 8 possible positions from boxes of a 3x3 grid centered at JACO's initial position, not including the central position. The enumeration of classes is depicted in Figure 2.2. After a random waiting time between 1.5 s and 3 s the target green dot appeared on the black screen and the subject could look at it and acknowledge its location, then after 1 s from the appearance an auditory cue was delivered, at which the subject had to move its gaze and attention towards the robot's hand. After 2 s from the sound, JACO started the target-oriented center-out straight movement from the initial position to the target position, which lasted exactly 2.5 s. The robot stayed still with the hand at the target position for 1 s, then went rapidly (about 1 s circa) to the initial position. The participants were instructed to follow JACO's hand with their gaze and to imagine they were observing their own hand moving. After the hand reached the initial position, the subjects could rest for 2 s before the beginning of the next trial. One run lasted a total of approximately 4 minutes. The schematic representation of the *robotrun*'s trial phases is depicted in Figure 2.4

During the *robotrun*, markers were sent on an LSL stream, as well as the target code, the 64-channels EEG and the current state of JACO — a 18-D vector with the 9-D commanded state and the 9-D current state, concatenated and both in the cartesian space (except for the fingers, that have joint space values). JACO's state and the EEG were streamed at 60 Hz and 200 Hz respectively, while markers were sent asynchronously to mark the phases of a trial. All streams, both of *eyeruns* and *robotruns*, were collected at a central point and recorded in a *xdf* file using LabRecorder (Version 1.12c).

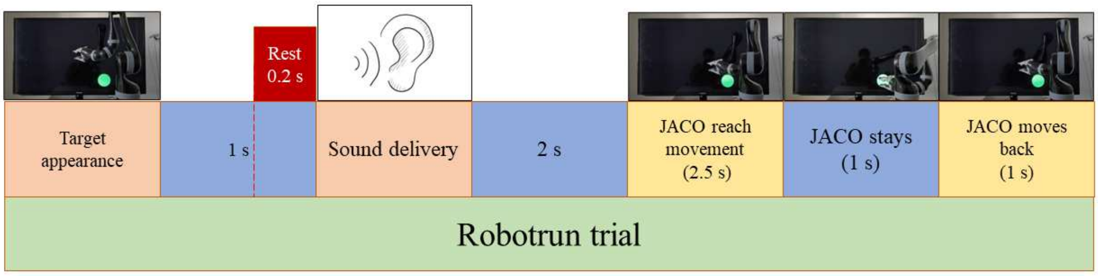

Figure 2.4: Schematic representation of a *robotrun*'s trial phases, including the rest period.

Eye-removal paradigm and processing The purpose of the *eyeruns* is solely to recognize and attenuate the effect of blinks and saccades artifacts by means of the EEG. This requires a separate paradigm, pre-processing and processing pipeline, implemented adapting the code kindly made available by Pulferer H. *Eyeruns* are based on the work of Kobler et.al. [28] [25], Mondini et.al. [38] and Pulferer et.al. [52] [53], who used such paradigm to remove saccades and blinking artifacts from the *robotruns*. Such paradigm allows to collect EEG waveforms related to blinks, saccades and eye rest (target fixation) in a controlled environment. The EEG is then used to build a model able to recognize such artifacts, which have very specific shapes for each subject, and remove them from the paradigm runs.

In this study, participants were instructed to avoid blinking or moving too much, if possible, during significant parts of the *robotruns*. Still, resorting to this method to remove eye artifacts as a step of the processing phase consistently contributed to the extraction of cleaner recordings.

The participants were instructed to perform one out of four oculomotor tasks described by the behavior of a blue dot on the screen. For every trial, a task was selected randomly between rest (the dot stays still, the subject has to stare at it), blink (the dot pulsates at the frequency the subject has to blink at), horizontal and vertical (the dot moves along a line, the subject follows it with the glance) conditions. The data is transformed through an Eyerun-specific pre-processing slightly different from the one of the *robotruns*, consisting of channel interpolation, first-order high-pass filtering at cut-off frequency of 0.18 Hz and anti-aliasing filtering, then *eye derivatives* are computed and added as channels to the EEG, which was finally downsampled at 100 Hz.

A first instance of the model is trained using the set of all trials, and single-trial performances were manually inspected to detect the subset of trials with bad removal performance. This would happen if the task was not detected correctly, e.g. the subject blinked or moved too much during some rest or saccade condition. Another instance of the model is then trained using only good trials, and its goodness in the removal of artifacts could be evaluated at the end by inspecting the topoplots before and after the application of the model to the *eyeruns*' EEG.

A final evaluation could be made using a batch of *eyeruns* data pre-processed with the common pipeline in Section 2.2, to which the model obtained from the processing part was applied. After completing the removal of artifacts, it is possible to inspect such pre-processed *eyeruns* EEG for visual feedback (Figure 2.5) of how the artifact removal would affect the *robotruns*.

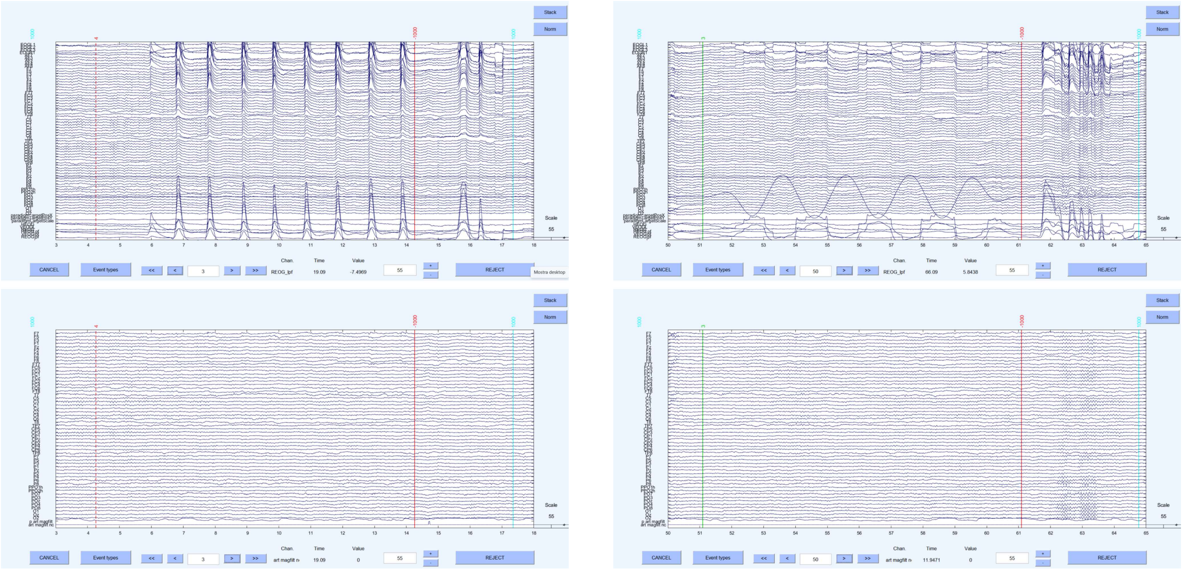

Figure 2.5: EEG signals of an *eyerun* of subject FK3 before (above) and after (below) the removal of artifacts. On the left, the signals refer to the execution of a "blink" task. On the right, of a "vertical saccade" task.

2.2 Pre-processing

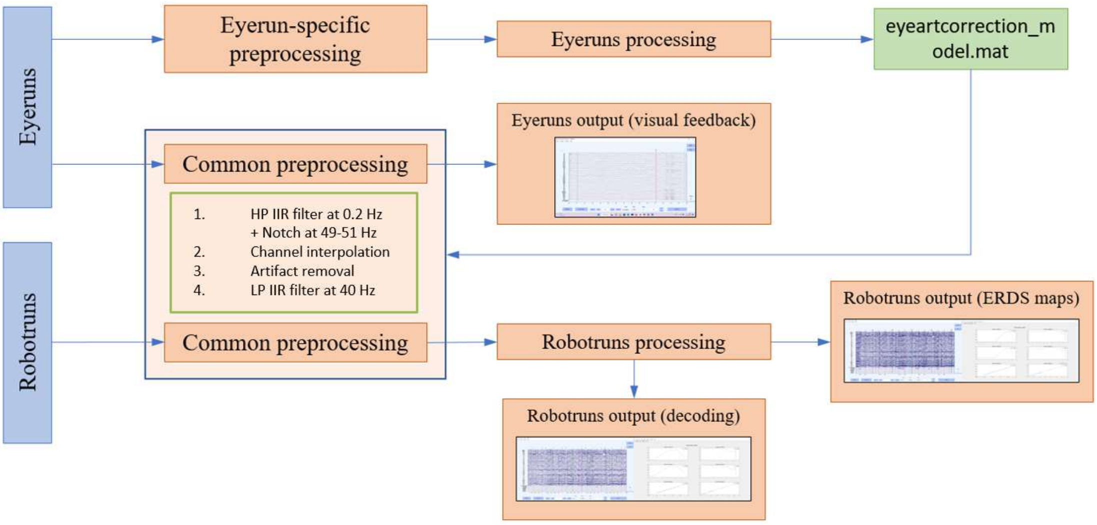

Figure 2.6: Schema of the relationship between the different pre-processing and processing types and the input and output blocks

The pre-processing phase used to transform the *robotruns* included several steps, the first of which was the conversion from the set of *xdf* files of the runs to a unique EEGLAB dataset (*.set* format). This required extracting the streams and aligning them, taking into account the delay from the generation of a marker (and so, the generation of input) and the delivery of the correspondent output at the workstation, — e.g. the correspondent display of the stimulus on the screen or state command finalization by JACO. We assume the cognition-related delay to process the visual information of the robotic movement to be negligible. Markers are converted to events in the EEGLAB dataset, the other streams are upsampled and, if necessary, interpolated to EEG's sampling rate, then added as "channels" with the relative channel properties.

The output of the conversion is an EEGLAB dataset containing a $(64+c) \times T$ "extended EEG" data matrix, where T is the number of time samples of a trial collected at 200 Hz, and c is the number of streams, different from the EEG, that were upsampled and concatenated to the latter so that for each EEG sample there is a correspondent value of that stream. In the case of *robotruns*, $c = 3$: one "stimuli"-type channel for the target code, and two "JACO trajectories"-type channels containing the JACO state values describing the position in the space of the end effector (hand) as abscissa and ordinate in the 2D plane at every time instant. The dataset also contains events bounded to start and duration, enabling to mark trial phases as segments of the data matrix.

The second step is the filtering: a first-order IIR non-causal high-pass filter is applied to the EEG with a cut-off frequency of 0.2 Hz, then two notch second-order butterworth non-causal filters are used at frequencies of 49 Hz and 51 Hz.

The third step of the pre-processing is the channel interpolation and removal of artifacts: bad channels were marked during the experimental session for each participant. Across subjects, an average of 1.13 ± 1.55 channels were interpolated (often in the neighborhoods of electrodes T7 and T8). Removal of eye artifacts is performed using the eye artifact correction SGEYESUB model extracted from the *eyeruns* (see Subsection 2.1.1). Attenuation of pops and drifts is done by applying the HEAR algorithm [27] to the EEG. After that, EOG and AF types of electrodes are removed from the EEG which is then spatially filtered with the CAR filter.

As the fourth and last step, a first-order butterworth low-pass filter is applied to the EEG with a cut-off frequency of 40 Hz.

An exceptional pipeline has been adopted for subject FL4 due to the fact that its *eyeruns* performance was too poor for an acceptable removal of the artifacts through a model built on it. Therefore, the channel interpolation and artifact rejection steps have been performed with Independnt Component Analysis (ICA), removing the components related to the eyes, to channel noise and power-line noise, performing all the filtering steps afterwards (except for the notch, which is not applied any more). A comparison of signals after the "classic" aforementioned pre-processing phase and the "exceptional" one has been made with the data of subjects FK1 and FK2 to ensure that the decoding performance would not suffer the difference in terms of performance. Results showed the same behavior or curves in the output of the time window selection subroutine (see Section 2.4.1) with a slight lowering of their magnitude. Therefore removing artifacts with ICA instead of the standard pipeline adopted in this work may result in lightly lower decoding performance, but does not alter the reasoning that can be built upon its characteristics.

Moreover, exceptions in the dataset dimension are present for subject FK4, who had markers of *robotrun* 4 corrupted that resulted in the removal of such run from the set, and the same for *robotruns* 4 and 8 of subject FL3. For subject FL6, only *robotruns* 1 to 6 have been used for decoding in the same conditions as all others participants, the reasons behind that will be explained in Chapter 3. Using a fewer number of runs for the decoding surely affects the performance due to the smaller dimensions of the training and testing dataset. Still, this showed to affect only marginally the decoding performance of this restricted subset of participants.

2.3 Processing

The processing phase is needed to extract, from the pre-processed EEGLAB dataset of the *robotruns*, a dataset with clean data partitioned in trials to be used for the decoding part. The process starts with using the dataset's events (previously markers) to reduce the trials to the meaningful part centered around the robot movement, which was fixed from 4 s before to 2.5 s after the event associated with JACO reaching the target (marker code 1004).

At this point, since "JACO trajectories"-type channels contain only the position of the hand, the computation of robot velocities must be performed by applying a third-order polynomial FIR smoothing Savitzky-Golay Filter to the x and y positions, and finally, adding them to the EEGLAB dataset as "METRIC"-type channels. Trials were then selected to be removed automatically, being marked for rejection if either the EEG of any channel exceeded a threshold of $\pm 100\mu V$ or if they had an abnormal probability or kurtosis (more than five standard deviations from the mean) [38]. An average of $55.43 \pm 18.56 (20.5\%)$ trials per subject were rejected by this method. The EEG and the kinematics can be visualized at the end of the process as in Figure 2.7.

For the same pre-processed *robotruns* dataset, two processing outputs were produced: one with the trial cut in the aforementioned window, to be used for decoding, and one from 7 s before to 2.5 s after the event associated with JACO reaching the target, containing a "rest" period to be used for the ERDS maps.

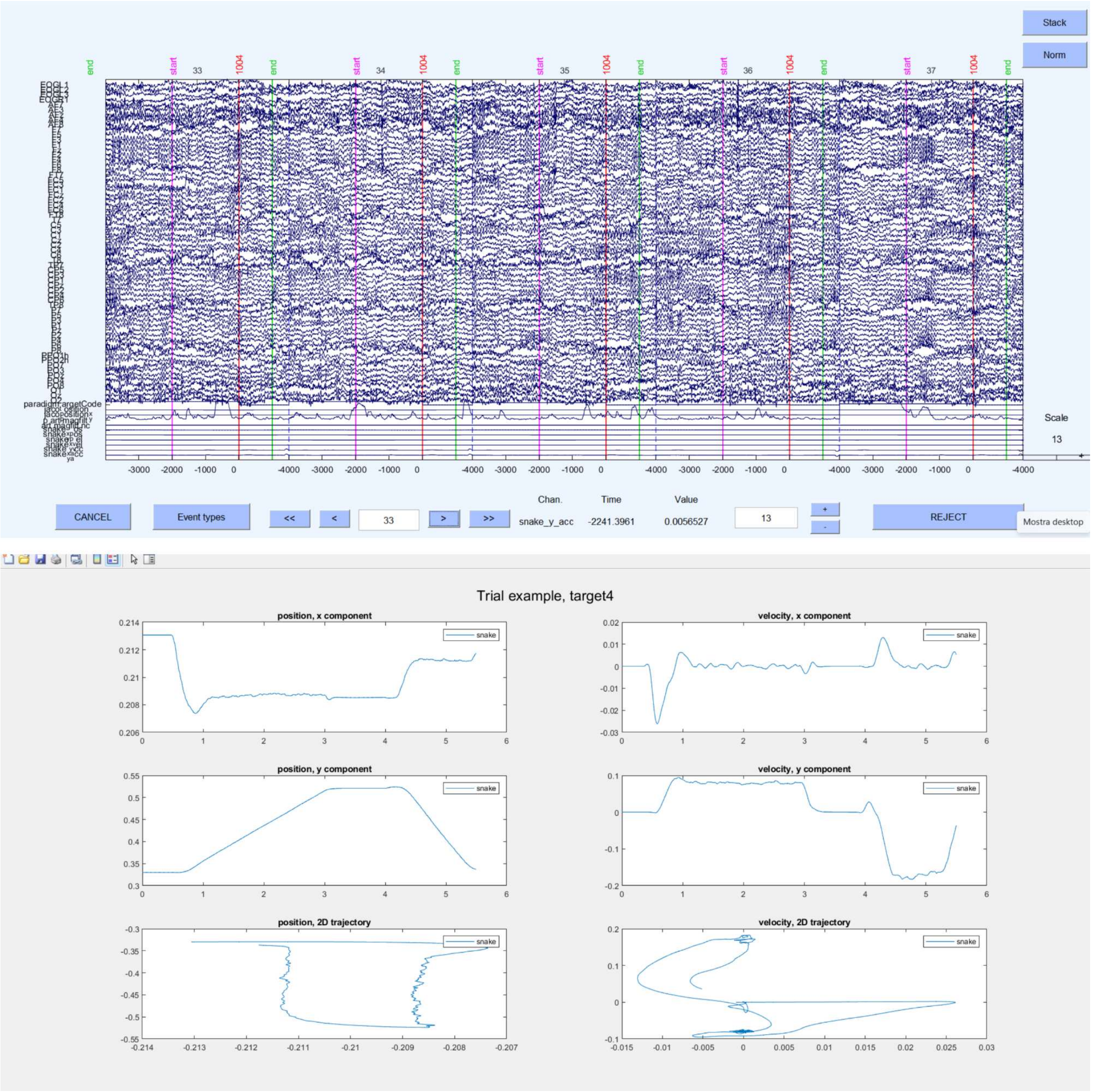

Chan. snake_y_acc
Time -2241.3961
Value 0.0056527

Figure 2.7: Processing output of a *robotrun* for decoding. Markers are displayed to show the beginning and the end of a trial cut for the decoding, around the reference "1004" marker defining the moment when JACO reachs the target. Below, the kinematics of a random trial are displayed after being epoched.

2.4 Decoding

In this thesis, two decoding tasks have been investigated, both related to the observed robotic arm kinematics. The first task was the multi-class classification of each EEG trial into the relative target label (following the enumeration in Figure 2.2) the observed movement was directed to during the observation, e.g. predicting target 1 from the EEG recorded while the participant was observing JACO reaching for target 1. This is formalized as a function

$$f_C : e \to c \quad with \quad e \in \mathbb{R}^{N\times T}\,,\, c \in C = \mathbb{N}^{[1,8]}$$

where $N = 55$ is the number of EEG channels excluding EOG and AF electrodes, T is the number of EEG time samples used and C is the set of classes. Such function would translate, in terms of BCI output, in the decoding of a goal-selection protocol.

The second task is the regression of JACO's kinematics from the correspondent EEG time-sample at every instant during a trial, which is a function

$$f_R : e \to k \quad with \quad e \in \mathbb{R}^{N\times T}\,,\, k \in \mathbb{R}^{M\times T}$$

where $N = 55$, T as before and $k = 4$ is the number of kinematics to be regressed, namely x position, y position, x velocity and y velocity relative to the hand of JACO in the 2D plane. The BCI output corresponding to this function would be based on a process-control protocol.

The conversion from the EEGLAB dataset output of the processing phase to the predictors and responses pairs for decoding was managed by a script that manipulates its data matrix. Such matrix is split into three *.mat* variables: 1) the EEG $\mathbb{R}^{N\times T}$ matrix of predictors, 2) the stimuli part, i.e. the target code to be used as the true response for training and evaluation of the decoder in the classification task, 3) the $\mathbb{R}^{m\times t}$ true responses matrix for the regression task, extracted from the channels containing the kinematics.

2.4.1 Classification task

Relatively to the first type of task, there was no manual feature selection process, and the full $N \times T$ matrix of a trial's EEG was used as input in the function to predict the target label.

The *time-window selection subroutine (TWSS)*

For a fixed type of model, a process called *time-window selection subroutine* serves to select the values of the hyperparameters and evaluate different types of models on common ground. The "hyperparameters" in this context are the length (*winSize*) and shift (*winShift*) of a specific window in the time domain, which is used to frame the EEG before feeding it to the model. The purpose, deepened in the discussion chapter, is to investigate phases of the observed movement that contain more information when encoded in the EEG, and therefore result in a better decoding performance. The algorithm of the process is reported in Algorithm 1 and explained below.

Algorithm 1 Pseudocode of the *TWSS*

```
Data: $X \in \mathbb{R}^{N \times T \times trials}$ , $Y \in C^{trials}$ , $modelType$
$iter \leftarrow 50$ ;
$test\_fract \leftarrow 0.4$ ;
$kfolds \leftarrow 5$ ;
$windSizes \leftarrow [0, 0.25, 0.5, 0.75, ...4]$ ;                                   /* s */
$overlap \leftarrow 1/4$ ;
$fs \leftarrow 10$ ;                                                                   /* Hz */
$X \leftarrow resample(X, fs, sampling\_rate(X))$ ;
for $i \leftarrow 1$ to $iter$ do
    $train\_vs\_test \leftarrow cvpartition("HoldOut", test\_fract, Y)$ ;
    $\{X_{tr}, X_{test}, Y_{tr}, Y_{test}\} \leftarrow split(X, Y, train\_vs\_test)$ ;
    $cv\_part \leftarrow cvpartition("KFolds", kfolds, Y_{tr})$ ;
    for $windSize$ in $windSizes$ do
        $ws \leftarrow \lfloor windSize \cdot fs \rfloor$ ;
        $os \leftarrow \lfloor ws \cdot overlap \rfloor + 1$ ;
        $winShifts \leftarrow$ {vector of numbers from ws+1 to T with step os} ;
        for $k \leftarrow 1$ to $kfolds$ do
            $\{X_{train}, X_{val}, Y_{train}, Y_{val}\} \leftarrow split(X_{tr}, Y_{tr}, cv\_part(k))$
            for $winShift$ in $winShifts$ do
                $\{X_{train}, X_{val}\} \leftarrow cut(\{X_{train}, X_{val}\}, [winSize, winShift])$ ;
                $\{X_{train}, X_{val}\} \leftarrow flatten(\{X_{train}, X_{val}\}, [trials, N \cdot ws])$ ;
                $[model, p_{val}] \leftarrow fitevalModelClass(X_{train}, Y_{train}, X_{val}, Y_{val}, modelType)$ ;
                $X_{val} \leftarrow shuffle(X_{val})$ ;
                $p_{val\_chance} \leftarrow evalModelClass(X_{val}, Y_{val}, model)$
                $save([windSize, windShift, p_{val}, p_{val\_chance}])$ ;
            end
        end
    end
end
```

The inputs of the process are the set of predictors X, the set of responses Y and the string *modelType* to select the specific model type to evaluate. The constants declared at the beginning of the algorithm have values fixed based on a trade-off between the time of computation of the subroutine, the resolution of the hyperparameters space grid, and the statistical reliability of the results. Subjects FK1, FK2 and FK3 were used as "control subjects" to elaborate the trade-off and come to the final choice of the process' constants. In the beginning, the EEG is downsampled from its own sampling frequency (200 Hz) to 10 Hz applying an FIR Antialiasing Lowpass Filter with cut-off frequency of 5 Hz. This was made for two reasons: the first is that, as stated in the previous chapter, LF-EEG encodes enough directional information about observed movements. The second is that downsampling the EEG to such frequency significantly reduces the time of computation of the process without any significant impact on the performance when tested on the control subjects. The Power Spectral Density (PSD) of the data of all subjects, where trials were resampled to 10 Hz, is shown in Figure 2.8

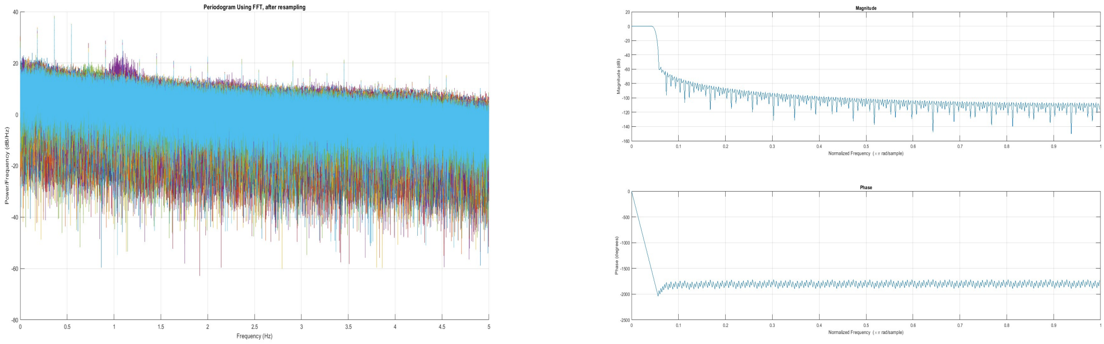

Figure 2.8: Left: Average PSD of the signal over trials and subjects after the application of *resample* and its filter; Right: frequency response of the applied anti-aliasing filter

50 iterations run with different partitioning between "training & validation", and test set, within an iteration 5 different partitions between actual training and validation for a total of 250 different training-validation-test partitions. Possible values for *winSize* go from 0 to 4 s of length, at steps of 0.25 s. *winShift* will have values that depend on the value of *winSize* at that iteration, representing ends of time-windows of length *winSize* in the past within the EEG of the trial, spaced by *winSize*/4 from each other. For example,

$$winSize = 2\,(s) \rightarrow ws = 20\,(samples), \quad winShift = 21\,(samples)$$

will result in a multi-class classification model trained on a portion of the EEG cut in samples 1 to 21, corresponding to a cut in time from 0 s to 2 s.

The function *cvpartition* returns a stratified partition of the input responses according to the input method: "Hold Out" divides the labels set in a training and testing partition according to the input test fraction, here fixed to be 40% of all the trials in the dataset. "KFolds" divides the labels set in *kfolds* partitions. The stratification ensures that all partitions, either produced by the "Hold Out" or the "KFold" method, contain a uniform distribution of classes to avoid skew data and training bias. Then the function *split* splits the actual input predictors and responses into two sets each, given the partition indexes output from *cvpartition*. The *flatten* function concatenated all EEG time samples of the same trial, producing a $trial \times (N \cdot ws)$ matrix representative of the trial from the $N \times ws \times trial$ EEG cut matrix. The output of *flatten*, jointly with the associated labels sets, is used to train the model of type *modelType* through the function *fitevalModelClass*, which outputs the model instance calibrated on the training partition and its performance evaluation on the validation partition, saved together with the set of hyperparameters. The function *evalModelClass* only computes the performance of a model prediction over a given input-output set, and it is used to compute the chance performance by shuffling the input's trials randomly before feeding it for prediction to the model.

For each subject, the saved outputs of the *time-window selection subroutine* are data structures that contain predictions, true values, confusion matrix and metadata and are unique for every iteration, combination of hyperparameters and k-fold. The accuracy of prediction is computed as fraction of correctly predicted trials over the total number of trials, then averaged over the k-folds to obtain one value for each possible combination of hyperparameters and iterations. These values are further accumulated in the data structure P to be indexed as $P(winSize, winShift, iter)$. For the same set of hyperparameters, the mean, the variance and the 95^{th} percentile of the distribution of values over iterations are computed, and values are visualized as a function of the hyperparameters and compared in order to find their best combination, as shown in the example for subject FK1 with the SLDA model in Figure 2.9. For each value of *winShift*, i.e. each subplot, a value of *winShift* is visually chosen to be a good trade-off between the time latency and the relative accuracy, it is marked by a green cross and the relative value of the hyperparameters are displayed together with its correspondent mean validation accuracy value. Together with the prediction accuracy, the chance test accuracy is computed in the same way, but on the prediction with the data whose trials were randomly interchanged by the *shuffle* function. From the point of view of the chance computation, an iteration consisted of a model being trained on an input-output relationship and evaluated before and after this relationship was broken, repeated for 50 iterations. The theoretical validity of this approach follows from the Central Limit Theorem under the hypothesis that two instances of the partitions from *randperm*'s shuffling are independent. To prove this hypothesis, and hence the statistical consistency of this computation, chance accuracies output of the *TWSS* of all subjects are stacked by *winSize*. A histogram of the chance accuracies for all trials (50 for each subject) and all subjects is computed for every *winShift*, along with a normal distribution that fits it. The distribution functions are averaged over *winShifts* to show in Figure 2.10 both for *modelType* SLDA and SVM that indeed the distribution of the values of the chance accuracies is gaussian and its mean approaches the theoretical chance level accuracy for $N = 8$ classes already at 50 iterations ($\Delta_p = (theoretical\ mean) - (actual\ mean) \in [0.0024, 0.015]$).

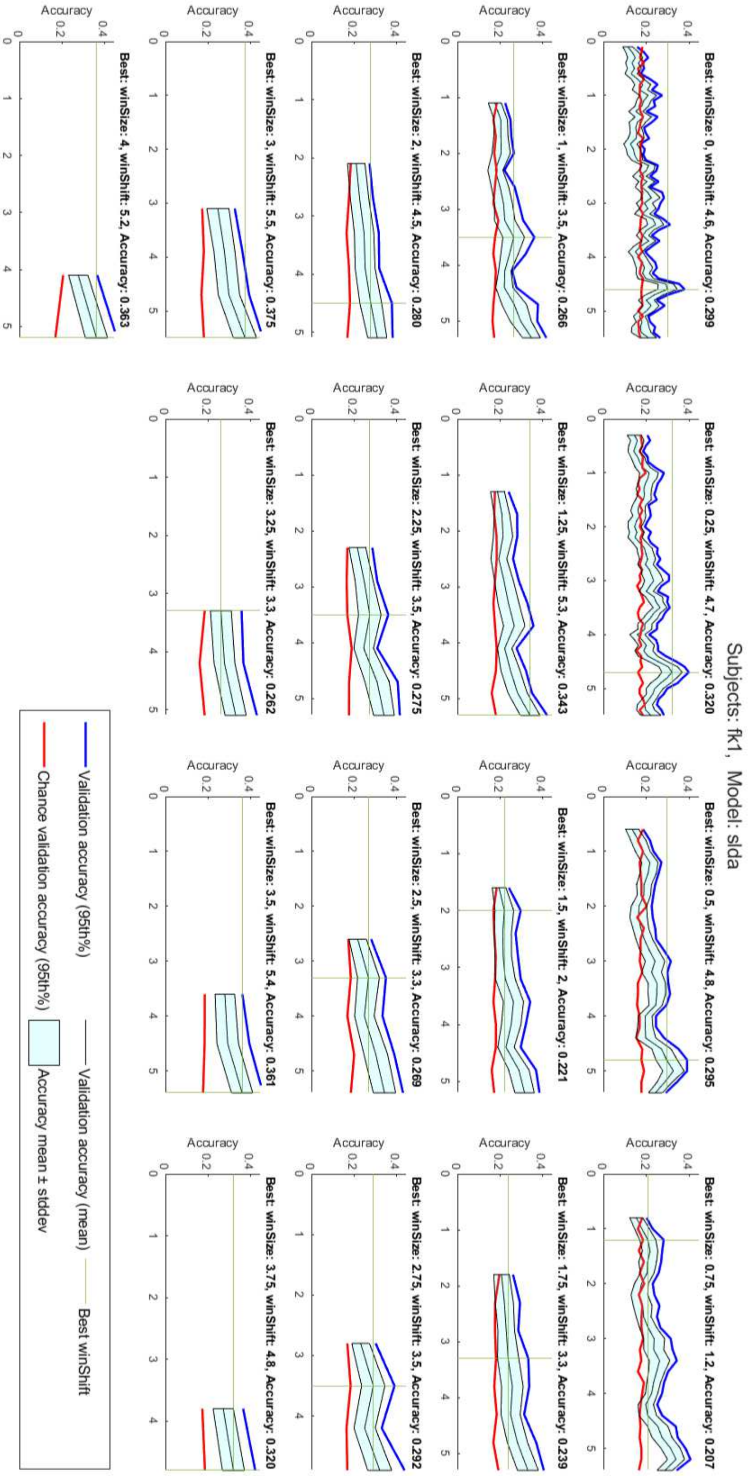

Figure 2.9: Visualization of the outputs of a *TWSS* performed with SLDA model and data of subject FK1. The 95th percentile of the distribution represented by the accuracy at all iterations, and the one of the relative chance accuracy, are displayed together with the mean accuracy and the standard deviation. In each subplot, the selected peak is highlighted by the green lines and its corresponding values of *winSize*, *winShift* and mean accuracy are reported in the text above. This plot configuration is the standard for the TWSS output and is used in all other TWSS's output figures too.

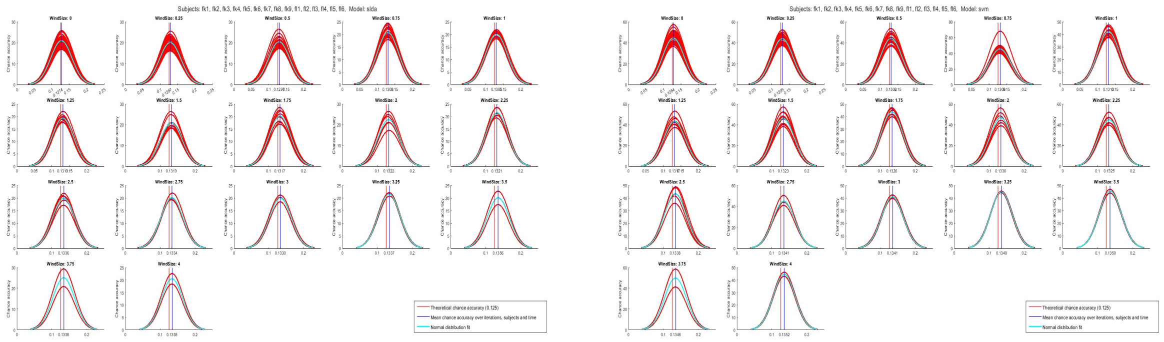

Figure 2.10: Chance level accuracy estimation consistency; Left: SLDA, Right: SVM

Through the TWSS it is possible to extract two combinations of hyperparameters: the so-called *early window* and *late window* are both defined by the combination of *winSize* and *winShift* with the highest accuracy, the first with correspondent value in time of $winShift \leq 3.5\ s$, the second with $winShift > 3.5\ s$. The choice of 3.5 s as the boundary is motivated by the fact that by the current cut of the trial, that time value corresponds to the progression of the movement where JACO just reached the target. From now on we will refer as *early window* or *late window* to the relative combination of hyperparameters values.

After the *TWSS* has been run and the windows' parameters have been selected, a similar process called *classification testing subroutine* (CTS, Algorithm 2) is started using trials cut defined by their value, wherein each of 300 iterations a model is trained on the training cut trials and evaluated on the test cut trials. In the end, the performance is stored as a confusion matrix to be handled and visualized at a later time.

2.4.2 Regression task

For the second task, the $N \times T$ matrix of a trial's EEG is used to predict the $M \times T$ matrix of the kinematics of the observed movement of JACO. For several iterations, a model is trained and tested, and its predictions are evaluated with several metrics and compared to the performance of a PLSUKF (Partial least square regression with Unscented Kalman Filter) model that we consider as a reference. Not needing to select hyperparameters, the decoding performance is collected by the *regression testing subroutine* (RTS, Algorithm 3) which is very similar to its classification version. The main differences are in the training

Algorithm 2 Pseudocode of the *classification testing subroutine* for a model with *winSize* and *winSize* fixed

```
Data: $X \in \mathbb{R}^{N \times T \times trials}$ , $Y \in C^{trials}$ , $modelType$ , $windSize$ , $windShift$
$iter \leftarrow 300$ ;
$test\_fract \leftarrow 0.4$ ;
$fs = 10$ ;                                                    /* Hz */
$X = resample(X, 10, sampling\_rate(X))$ ;
for $i \leftarrow 1$ to $iter$ do
    $train\_vs\_test \leftarrow cvpartition("HoldOut", test\_fract, Y)$ ;
    $[X_{train}, X_{test}, Y_{train}, Y_{test}] \leftarrow split(X, Y, train\_vs\_test)$ ;
    $ws \leftarrow \lfloor windSize \cdot fs \rfloor$ ;
    $[X_{train}, X_{test}] \leftarrow cut([X_{train}, X_{test}], [winSize, winShift])$ ;
    $[X_{train}, X_{test}] \leftarrow flatten([X_{train}, X_{test}], [trials, N \cdot ws])$ ;
    $[model, p_{test}] \leftarrow fitevalModelClass(X_{train}, Y_{train}, X_{test}, Y_{test}, modelType)$ ;
    $save(p_{test})$ ;
end
```

and evaluation functions, in the fact that the data is not flattened beforehand but only internally if the model needs it, and in the fact that the kinematics are down-sampled to have the same time/samples rate of the EEG at 10 Hz. Nevertheless, this is done through *downsampling* and not *resampling*, that according to the implementation and nomenclature given by Matlab, does not apply the anti-aliasing filter. The kinematic trajectories consist of position X, position Y, velocity X and velocity Y, where the X coordinate and the Y coordinate refer to, respectively, a robotic movement in the horizontal and vertical direction, as by Figure 2.2.

Another difference is that the chance level performance p_{test_chance} cannot be determined in the same way of the CTS, therefore the same approach of the TWSS is followed: the input trials are randomly shuffled, then the kinematics are predicted and paired to the true "un-shuffled" kinematics to compute the results.

2.4.3 Models

Several types of models have been used for the decoder in both tasks, all implemented starting from trusted Matlab libraries and whose details impact the processes only at training or evaluation function level in a modular way.

Algorithm 3 Pseudocode of the *regression testing subroutine*

```
Data: $X \in \mathbb{R}^{N \times T \times trials}$ , $Y \in \mathbb{R}^{M \times T \times trials}$ , $modelType$
$iter \leftarrow 50$ ;
$test\_fract \leftarrow 0.2$ ;
$fs = 10$ ;                                                      /* Hz */
$X = resample(X, 10, sampling\_rate(X))$ ;
$Y = downsample(X, 10, sampling\_rate(X))$ ;
for $i \leftarrow 1$ to $iter$ do
    $train\_vs\_test \leftarrow cvpartition(''HoldOut'', test\_fract, Y)$ ;
    $[X_{train}, X_{test}, Y_{train}, Y_{test}] \leftarrow split(X, Y, train\_vs\_test)$ ;
    $[model, p_{test}] \leftarrow fitevalModelRegr(X_{train}, Y_{train}, X_{test}, Y_{test}, modelType)$ ;
    $X_{test} \leftarrow shuffle(X_{test})$ ;
    $[p_{test\_chance}] \leftarrow evalModelRegr(X_{test}, Y_{test}, model)$ ;
    $save([p_{test}, p_{test\_chance}])$ ;
end
```

Classification task The model types tested in the classification were classic (LDA) and Shrinkage Linear Discriminant Analysis (SLDA), SVM with Linear and Gaussian kernel, linear classification through Logistic Regression, Extreme Learning Machine (ELM), MLP, Decision Tree Ensembles, GRU, BiLSTM and CNN.

Among them all, the two best-performing models were SLDA and SVM, therefore their performances are the only ones analyzed and compared in the following chapters. Shrinkage Linear Discriminant Analysis is a variation of the classic LDA model for binary classification i.e. a weighted linear combination of the features (in this context, the flattened EEG cut) for which weights are found to maximize the difference between two classes. LDA works under the assumption that the probability density function of an input belonging to a certain class is always gaussian, and that all classes have the same covariance matrix Σ. The distribution's parameters are estimated from the training data as [19]:

$$
\begin{aligned}
\hat{\pi_k} &= N_k/N \\
\hat{\mu_k} &= \sum_{g_i=k} x_i/N_k \\
\hat{\Sigma} &= \sum_{k=1}^{K}\sum_{g_i=k}(x_i-\hat{\mu_k})(x_i-\hat{\mu_k})^T/(N-K)
\end{aligned}
\tag{2.1}
$$

Where x_i are the inputs from the training set X of dimension N, $\hat{\pi_k}$ is the estimated prior probability of class k, N_k is the number of class-k observation, $\hat{\mu_k}$ is the center of the distribution of class k, $\hat{\Sigma}$ is the predicted covariance matrix, K is the number of classes. Then for two classes 1 and 2, LDA will classify to class 2 a sample x if

$$
x^T\hat{\Sigma}^{-1}(\hat{\mu_2}-\hat{\mu_1}) > \frac{1}{2}(\hat{\mu_2}+\hat{\mu_1})^T\hat{\Sigma}^{-1}(\hat{\mu_2}-\hat{\mu_1}) - log(N_1/N_2) \tag{2.2}
$$

Then the one-vs-all or one-vs-one approaches can be adopted to transpose the technique into the domain of multi-class classification. SLDA improves LDA by regularizing the estimation of the covariance matrix, adding a scaled identity matrix that shrinks the estimated covariance matrix towards a diagonal matrix. This avoids the "curse of dimensionality" issue that arises when the number of input features is much larger than the number of training samples [31] [46].

On the other hand, Support Vector Machines (SVM) are based on a non-linear mapping of inputs into a high-dimensional feature space where a linear decision optimal hyperplane is found for classification, such that training data is separated with a maximal margin [14]:

$$
\begin{aligned}
&\bar{w_0}, b_0 \quad s.t. \quad \bar{w_0}\cdot x + b_0 = 0 \\
&and \quad \rho(\bar{w_0}, b_0) = \min_{x:y=1}\frac{x\cdot\bar{w_0}}{|\bar{w_0}|} - \max_{x:y=2}\frac{x\cdot\bar{w_0}}{|\bar{w_0}|} \quad is\ maximum
\end{aligned}
\tag{2.3}
$$

The vector x above is defined as a support vector. In case the data is not perfectly separable, "soft-margin" hyperplanes can be used to allow a minimum number of errors. The non-linear mapping that transforms an input in a support vector is a function $\phi : \mathbb{R}^n \rightarrow \mathbb{R}^N$ yielding that the classification of an input feature vector x is a function $f(x) = \bar{w_0} \cdot \phi(x) + b_0$. The function $\phi(x)$ is defined by a Kernel function $K(u,v) = \phi(u) \cdot \phi(v)$ with specific properties, some of the most common types of Kernel functions for SVMs are the Linear ($K(u,v) = sum(u \cdot v)$), Polynomial type of degree d ($K(u,v) = (u \cdot v + 1)^d$) and Gaussian/RBF type ($K(u,v) = exp(-\gamma \cdot ||u - v||^2$, γ fixed in [0,1]). The transposition to multi-class classification is handled similarly to LDA.

Regression task For regression, the performance of several model types was investigated with the control subject to find the model with the highest qualitative and quantitative results, to be generalized for all subjects and compared to a PLSUKF model. The latter is based on two main components: the continuous state decoding through Unscented Kalman Filter (UKF), which takes advantage of non-linear feature combinations that can help the prediction when added to the input, and the mapping in the latent features subspace by Partial least squares (PLS) regression.

The first relies on using the same state-transition matrix F of the classic KF to estimate the current state, then directly computing and concatenating the nonlinear features to obtain the matrix X for the computation of the matrix H that relates the state to the measurement latent space. The second maps the high-dimension measurement matrix Z in Z_L defined in a latent space whose dimension N_{latent} is chosen to explain most of the input's variance, with the aim of reducing the redundancy and increase the speed in the computation of H [38] [26] [53]. In this context, X are robot kinematics and Z is represented by the EEG, $N_{latent} = 85$ explains 99% of the EEG's variance [38].

To be compared to PLSUKF, several types of models have been evaluated in the task of decoding the 4D kinematics of the robot from the EEG: Multivariate Linear Regression, SVM, simple Feed-Forward Neural Network, CNN, GRU, LSTM and BiLSTM, as well as custom models. Among them, two similar custom models were able to give a consistently better performance compared to the others, and they are the *PLSSVM* and the *PLSRTE* models.

Regarding the PLSSVM, the inspiration came from the results of the SVM model in the classification task with the experimental data, hence the idea was to carry this trend into the sequence-to-sequence multivariate regression domain, which is widely approached in the literature with Deep Learning models like CNN and RNN that have the issue of being notoriously "data-hungry", i.e. requiring big quantities of data for fitting the high quantity of parameters they are provided with. The purpose of the PLSSVM is to introduce in this domain the properties of the lightweight SVM that we knew performed well in the classification even with the small amount of data that could be collected for this study. In the implementation, the input EEG matrix of a trial X is concatenated to its "lagged" versions with lags from 1 to 12 samples in the past, in an approach similar to the PLSUKF in Mondini et.al [38]. Considering that the input data has sampling frequency of 10 Hz, each actual time-sample of the input is a N_{+}-dimensional feature vector with $N_{+} = 55 \cdot (12(past) + 1(current)) = 715$, containing the EEG from the current instant to 1.2 seconds in the past. The resulting predictors matrix $X_L \in \mathbb{R}^{N_{+} \times T \times trials}$ is used together with the responses matrix $Y \in \mathbb{R}^{M \times T \times trials}$ to train a PLS regression with dimension of the latent space $N_{latent} = 24$. The model is used for the dimensionality reduction step as in the PLSUKF, but the transformed input is fed to a set of SVMs with linear kernel function $\phi(X)$ rather than to the UKF. Hence, the set is composed of M independent models SVM_i , $i \in [1, M]$, each trained to predict only one type of kinematic trajectory $Y_i \in \mathbb{R}^{T \times trials}$ from X_L, formally [65] [58]:

$$\begin{gathered} SVM_i(X_L) =< \bar{w}, \phi(X_L) > +b = Y_i \quad with\ \bar{w} \in \mathbf{X_L} = \{domain\ of\ the\ input\} \\ where \\ minimize \quad J(\bar{w}) = \frac{1}{2}\ ||\bar{w}|| \quad subject\ to \quad \begin{cases} Y_i - < \bar{w}, \phi(X_L) > -b \leq \epsilon \\ < \bar{w}, \phi(X_L) > +b - Y_i \leq \epsilon \end{cases} \end{gathered} \tag{2.4}$$

Regarding the so-called PLSRTE custom model, it follows the same approach of the PLSSVM: the lagged EEG is mapped in the latent space of dimension $N_{latent} = 24$ for the dimensionality reduction step, then the transformed input is fed to a set of Regression Tree Ensembles (RTE), rather than to the UKF or the set of SVMs, whose structure is composed of M independent models RTE_i , $i \in [1, M]$ (one for each type of kinematic trajectory Y_i.

The mapping between the transformed input and the prediction through an element RTE_i is depicted in Figure 2.11. Such independent model is composed of L weak learners $T_1, ..., T_L$ fitted by the Least-Squares Boosting algorithm, i.e. each weak learner is fitted on the difference between the true response and the aggregated prediction of all learners grown previously while minimizing the MSE. Shrinkage can be added to this process by fixing a value for the "Learning Rate" hyper-parameter. The "weak learners" in this model are binary regression trees whose depth is fixed to be $d = 100$, and whose branch nodes and leaves have a fixed number of minimum observations. The prediction of each weak learner T_l constituting the ensemble is aggregated in a weighted average to produce the final output of the model. Finally, the predicted trajectory is smoothed through a moving average filter with a 3-sample-wide window to attenuate the jitter.

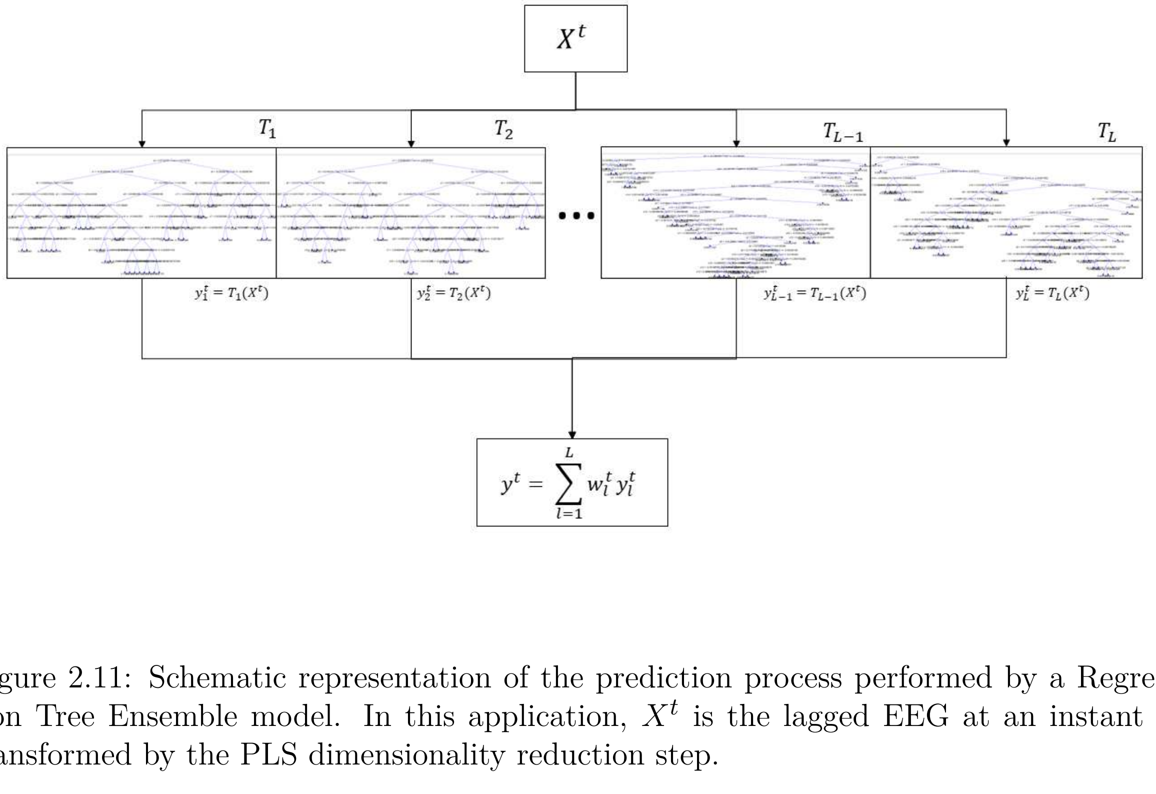

Figure 2.11: Schematic representation of the prediction process performed by a Regression Tree Ensemble model. In this application, X^t is the lagged EEG at an instant t, transformed by the PLS dimensionality reduction step.

The PLSSVM and PLSRTE models, compared to the PLSUKF, use double the number of lags (0.6 seconds more), transformed into an almost four times (compared to the

$N_{latent} = 85$ of the PLSUKF) smaller vector of latent components and used as direct input for the regression of kinematic trajectories. There is no computation of non-linear kinematics, and no auto-regressive feedback is included, as the output is uniquely determined by the lagged EEG. It must be said that the dimensionality reduction step is fundamental for a sufficient performance, since the Linear-kernel SVM and the Regression Tree Ensemble alone are not sufficient to predict the kinematics directly from the lagged EEG. On the other hand, the PLS Regression algorithm is too coarse-grained and has very poor decoding performance. Therefore, by combining the information extraction properties of the first components and the predictive capabilities of the second it is possible to resort to the flaws of each and obtain an overall satisfactory decoding.

2.4.4 Performance evaluation

The measures used to objectively evaluate the performance are the indexes commonly used in the literature to estimate the goodness of a classification or a regression, and they are chosen specifically for the task and the target property to be evaluated.

Classification After visualizing the output of the *TWSS* and having selected the best early and late window (see end of Subsection 2.4.1) for each subject based on the validation accuracy, the confusion matrix of the test predictions is obtained as the output of the *CTS* where the subject-specific hyperparameters were used. Four cases are displayed: SLDA with early and late window, SVM with early and late window, in each the confusion matrix is shown together with useful measures that can be extracted from it [2]: test accuracy, chance test accuracy, Cohen's Kappa, F-measure with $\alpha = 1$.

The accuracy of prediction (across classes) p and the chance accuracy $p0$ are computed from the matrix as:

$$p = \frac{\sum C_{i,i}}{N} = \frac{TP + TN}{TP + TN + FP + FN} \quad , \quad p \in \{\mathbb{R} \cap [0,1]\}$$

$$p0 = \frac{\sum C_{:,i} \cdot C_{i,:}}{N^2} \quad \in \{\mathbb{R} \cap [0,1]\} \tag{2.5}$$

where $C_{i,i}$ is the number of correctly predicted trials for class i, easily obtained as the trace of the confusion matrix, and N is the total number of trials.
Cohen's Kappa measures the "level of agreement" between a target model and a chance predictor and therefore it is inversely proportional to the difference between the two performances. The F-measure (also called F-beta measure with $\beta^2 = \alpha$) is the harmonic mean of the precision ((1-F), a measure of the true positives detection) and recall (H, a measure of the false detection rate) to give a complete statistic that summarizes the two under significance level α balancing the contribution of each [54]. They are formally defined as, respectively:

$$\kappa = \frac{p - p_0}{1 - p_0} \quad where \quad p_0 = \frac{\sum C_{i,:} C_{:,i}}{N^2} \tag{2.6}$$

$$F_\alpha = \frac{(1+\alpha) \cdot (1-F) \cdot H}{\alpha \cdot (1-F) + H} \quad where \quad \alpha = 1 \, , \, F = \frac{FP}{TP + FP} \, , \, H = \frac{TP}{TP + FN} \tag{2.7}$$

Regression The kinematic trajectories predicted by the decoder are compared to the true trajectories of the JACO state, the measures of similarity considered are Pearson's Linear Correlation Coefficient r and Root Mean Squared Error $RMSE$. Given the predicted time-varying trajectories $\hat{y} = [\hat{y}^{px}; \hat{y}^{py}; \hat{y}^{vx}; \hat{y}^{vy}]$ and the true trajectories $y = [y^{px}; y^{py}; y^{vx}; y^{vy}]$, the correlation coefficient captures the similarity of two trajectories in terms of mean and variance. It is computed for the kinematic quantity j as below:

$$r(j) = \frac{1}{trials} \sum_{tr=1}^{trials} \left[\frac{\sum_{t=0}^{T} (\hat{y}_t^j(tr) - mean(\hat{y}^j(tr)) \cdot (y_t^j(tr) - mean(y^j(tr)))}{\sum_{t=0}^{T} (\hat{y}_t^j(tr) - mean(\hat{y}^j(tr))^2 \cdot \sum_{t=0}^{T} (y_t^j(tr) - mean(y^j(tr)))^2} \right] \tag{2.8}$$

The RMSE captures the absolute error between the prediction and the truth at every instant, it can be imagined as a measure of how close to the ideal movement JACO would stay if it was commanded by the decoded EEG. It is computed for kinematic j over time and trials as:

$$RMSE(j) = \sqrt{\frac{\sum_{tr=1}^{trials}\sum_{t=0}^{T}(\hat{y}_t^j(tr) - \hat{y}_t^j(tr))^2}{trials \cdot T}} \tag{2.9}$$

CHAPTER 3

Results

The methods and processes described in Chapter 2 allowed to collect and analyze the experimental data, leading to the results that are shown in the upcoming chapter. Here, the first section revolves around the classification task results, with the outputs of the TWSS for the hyperparameter results and the final test results. The second section focuses on the findings of the regression task, including the qualitative and quantitative analyses of the EEG trajectory decoding. The third and last section describes the event-related desynchronization patterns during the trial timings, first in a general way, then as activation related to the movement's direction.

3.1 Classification task

The outputs of the TWSS of each subject with SLDA and SVM are accumulated, keeping in mind that, for each of them, they consist of 50 values of mean validation accuracy from the k-fold cross-validation, and are displayed in the same way as for single subjects, in order to derive conclusions that are generalized with respect to the individual. The outcome is shown in Figures 3.1 and 3.2, it can be observed how the trend of the validation accuracy within the same subplot, i.e. the same choice of *windSize*, is very similar for the two models, showing two main peaks that translate into the early and late windows, and suggesting that such behavior is indeed a time-depending property of the EEG during the task, generalizable across the employed models. While Figures 3.1 and 3.2 show the analysis using models that are trained singularly on each subject's data and whose performances are averaged over subjects, it is possible to investigate the behavior of a model that is generalized across subjects, by merging all datasets and performing a TWSS with the merged data, labeled as belonging to a virtual subject "gen". The output of such process is shown in Figures 3.3 and 3.4, it can be noted how the distribution's variance decreases thanks to the availability of a bigger dataset for training the model, tightening the distribution and the 95th percentile around the arithmetic means. Moreover, the trend of the latter in each subplot is very close to its correspondent in the previous figure, enforcing the conclusion that the existence of two main windows for trial classification can be generalized across subjects and models.

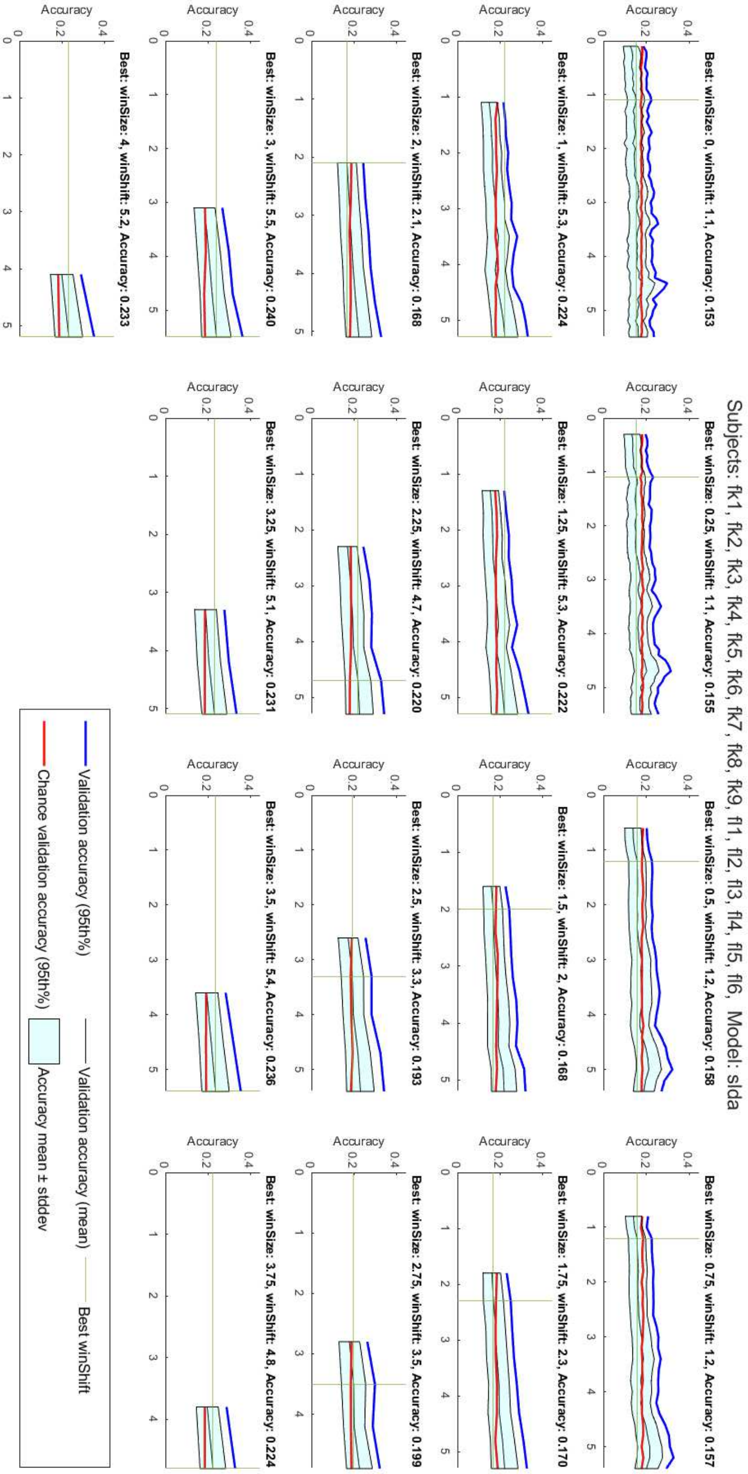

Figure 3.1: Average of single-subject TWSS using the SLDA model for all subjects and iterations.

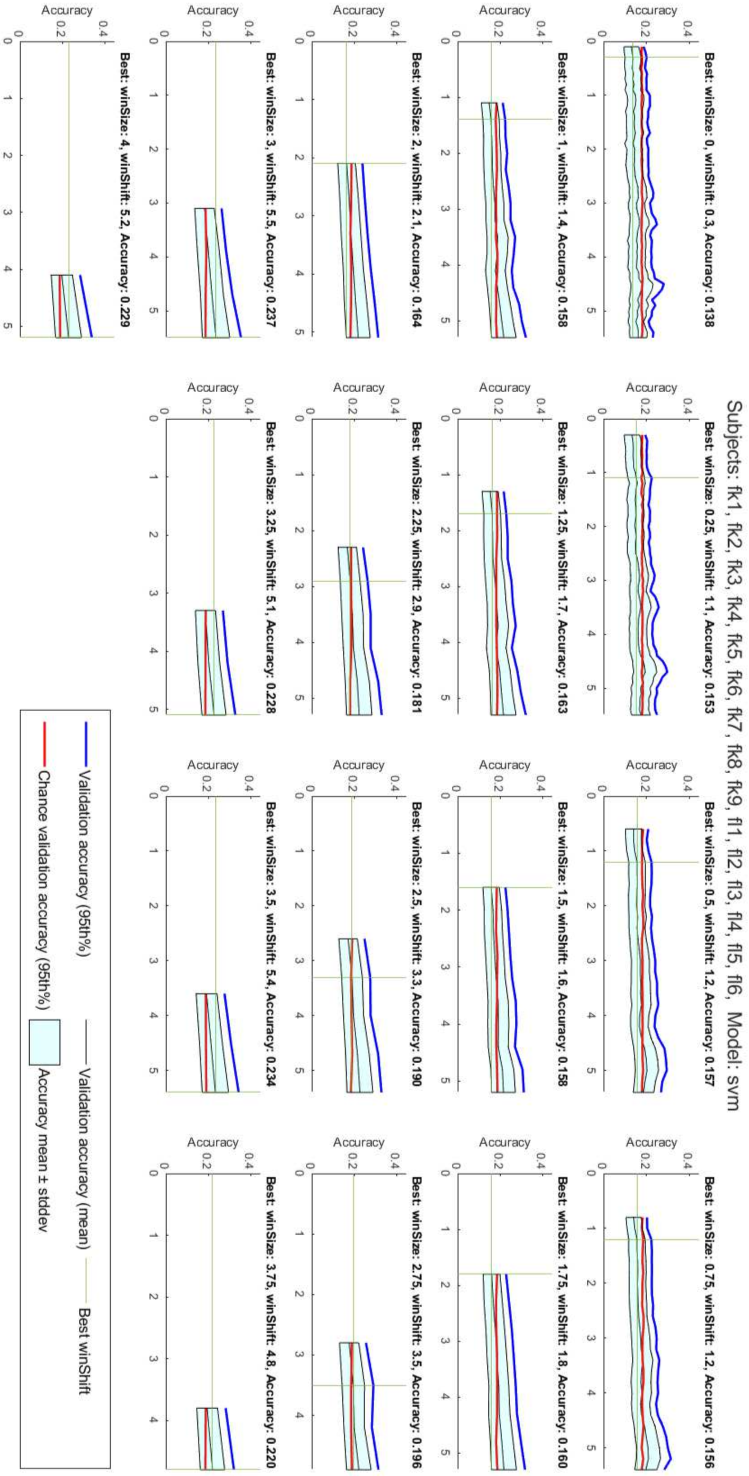

Figure 3.2: Average of single-subject TWSS using the SVM model, for all subjects and iterations.

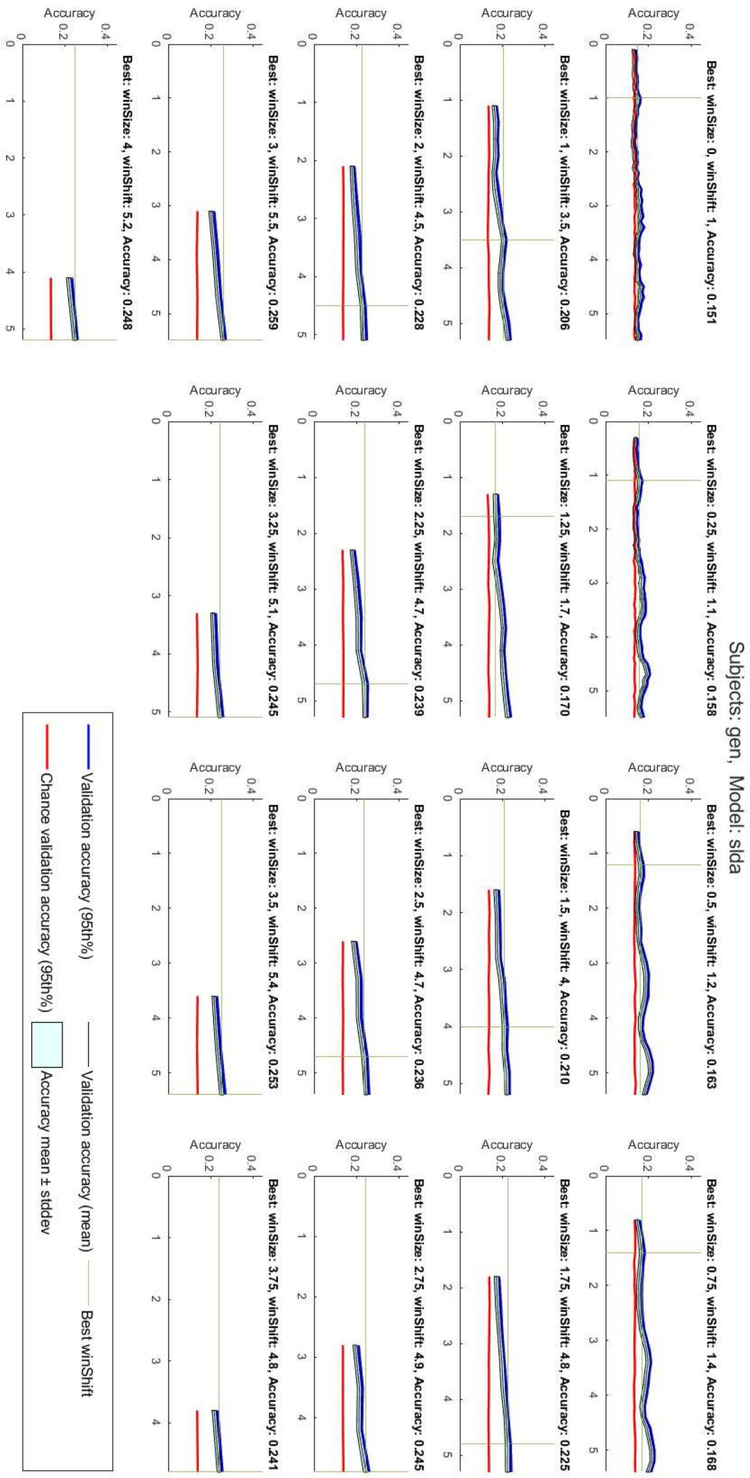

Figure 3.3: Output of the TWSS with virtual subject "gen" (resulting in the subject-generalized model) using the SLDA model. For each hyperparameter combination, the distribution comes from the iterations.

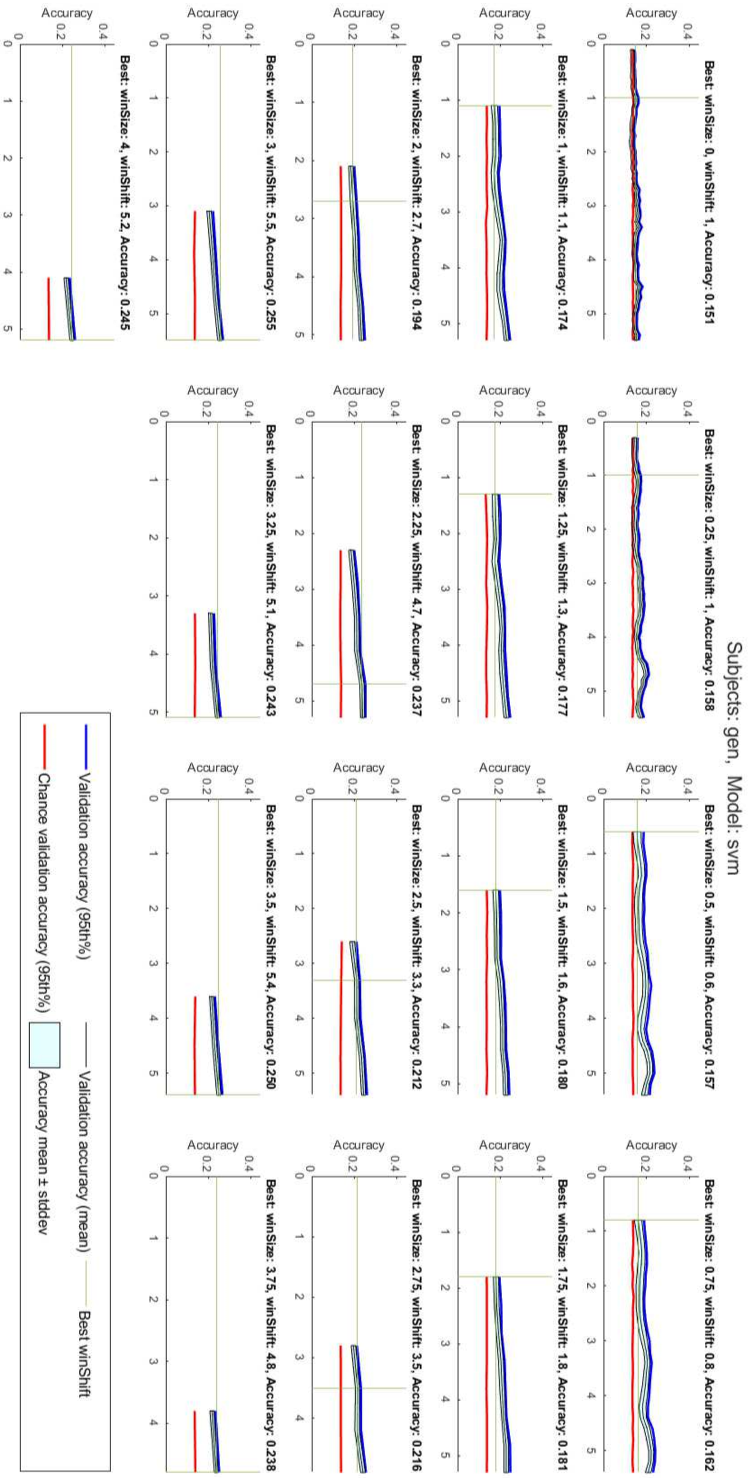

Figure 3.4: Output of the TWSS with virtual subject "gen" (resulting in the subject-generalized model) using the SVM model.

From Figure 3.1 and 3.2, the aforementioned windows are found to have optimal values of $winSize = 2.75$ and $winShift = 3.5$ for the *early window*, and $winSize = 3$ and $winShift = 5.5$ for the *late window*. The portions of movement framed by the time windows are visualized in Figure 3.5 in the vertical and horizontal position trajectories, plotted in time. Trajectories are also visualized as spanning the 2D plane JACO moves the hand on during the trial. The early and late windows are highlighted in both types of plots in red and yellow respectively, and their relative mean validation accuracy with SLDA and SVM models (i.e. their value in Figures 3.1 and 3.2) is shown.

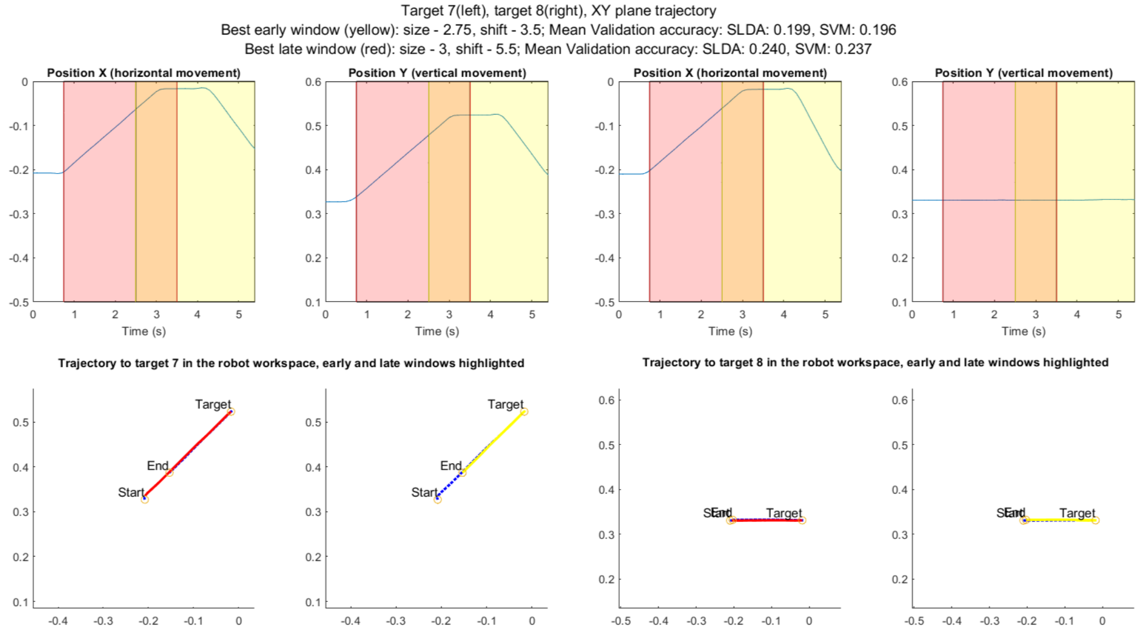

Figure 3.5: Visualization of the time-varying kinematics and the part of them that is spanned by the early and late time windows. The values of *winSize* and *winShift* are reported on the top, together with their mean validation accuracy with SLDA and SVM.

Observing the results presented at this point, it is natural to question the origin of the peak captured by the late window, as it is not appearing during the main target-oriented movement. One of the possible reasons could be attributed to the speed of the movement, considering that a faster movement may have a different impact according to Section 1.2. Given the presence of the "early window peak" during the last part of the reaching action, and assuming that the intensity of the peak can be increased by increasing its speed, to be verified by the experimental data is the hypothesis that, by increasing the movement speed, an accuracy peak will show with higher or equal intensity than the one of the observed "early window peak" during the normal, "slow" case, in the same phase of the action. To test the hypothesis, the second half of the experimental session of subject FL6 consisted of 6 *robotruns* characterized by a faster target-oriented reaching movement of duration 1 s (the same speed by which the arm goes back to the starting position) compared to the usual 2.5 s. This results in the action happening from second 1 to second 2 according to the trial times. 6 runs were recorded in such conditions and considered as belonging to a virtual subject "FL6 fast", contrasting subject FL6 under normal conditions, named in this context "FL6 slow". One TWSS was run for each of them, and the outputs are shown in Figure 3.6, below the kinematic trajectories that describe the changes between the two types of conditions. From the results, it can be observed that in the "fast" condition, despite the accuracy being generally equal or higher, the only significant peak present is around second 3 (when JACO is stable on the target), not including in any way the target-oriented movement. Therefore, the hypothesis is rejected, and the underlying assumption that the intensity of the peak relative to the reaching movement can be increased by increasing the speed of the movement must be false.

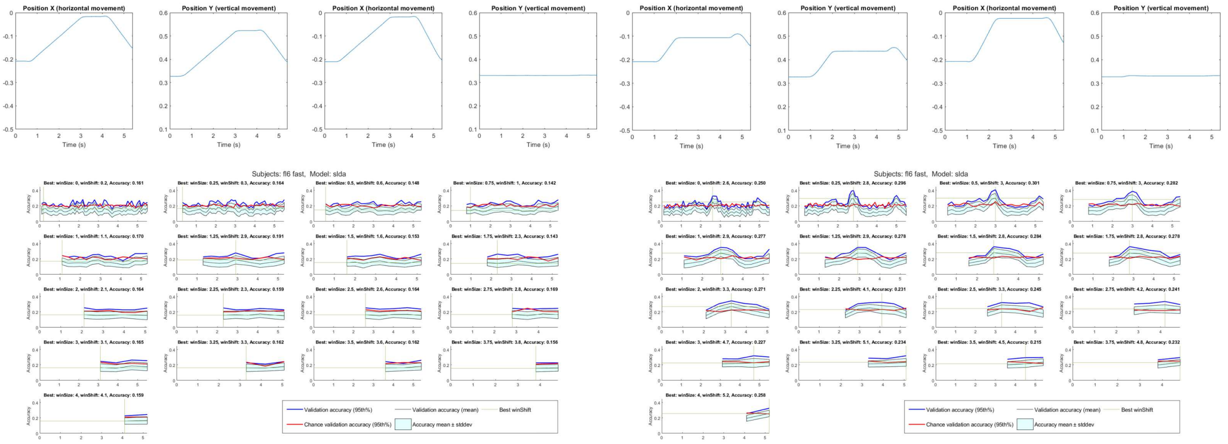

Figure 3.6: Comparison between the outputs of the TWSS from the data of subject FL6 in the "fast" (left) and "slow" conditions. Above them, the kinematic trajectories in the same time range give insight into the difference between the observed movements in the two conditions.

Back to the results of the TWSS, the chosen time windows displayed in Figure 3.5 are generally defined based on results averaged across subjects, and are not specific for them. According to the fact that the neural activity of an individual has very subjective features, the best early and late time windows of a subject may differ from the "average" best ones found, depending on the subjective behavior of the neural signals, on the interpretation and execution of the task by the participant and the level of the attention given to the different phases of the observed movement. Recalling that such values are determined from the subject-specific TWSS evaluation and used in the CTS to determine the test accuracy, Figure 3.7 shows the histogram of how often a certain time interval is included in a subject-specific window. This is done for intervals of 0.25 s, displayed side-to-side for the early and late windows, for SLDA (left) and SVM (right). This helps to get insight on what parts of the movement are the most informative in terms of neural correlates, therefore resulting in higher decoding accuracy and being included in the optimal time window. It can be observed how, despite the subject-specific variability, the most informative portions of the movement for all subjects are 1) right before the robot arrives on the target (2.25 - 2.75 s) and 2) when it is steady on it and starts to move back (3.25 - 4.75 s). Moreover, the portion of movement between 2.75 s and 3.25 s seems to be informative, since it is included often in both types of windows. In fact, despite not being the most frequently included for any of the types of window singularly, such interval approximately coincides with the optimal early window found from the average TWSS.

Below each model type's histogram, a plot displays the performance of each participant in terms of test accuracy using the subject-specific best windows, further validating how each participant exhibits different decoding potential depending on several variables. The plots show the test accuracy with the early window and with the late window, as well as the difference between the two. This is due to the fact, more deeply argued in Chapter 4, that a higher accuracy in the early window compared to the late window is preferred for reasons of applicability and usefulness of the decoded activity.

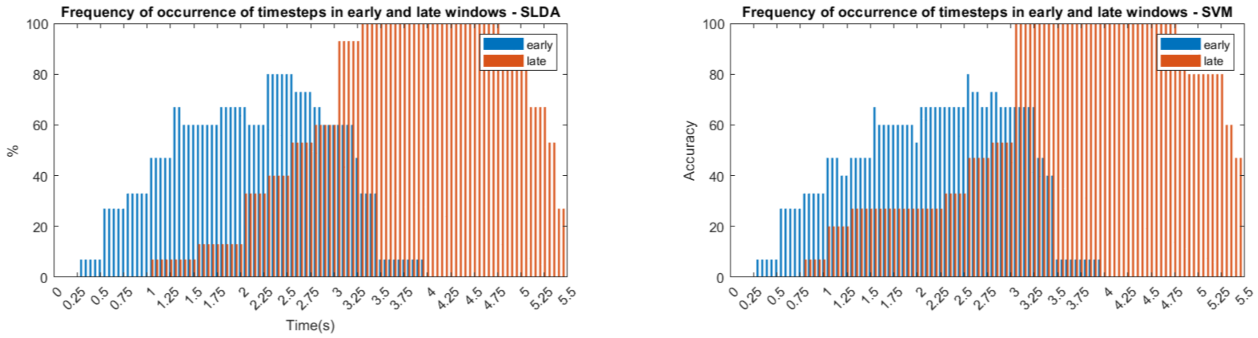

Figure 3.7: Histograms depicting the frequency of occurrence of a certain time interval in the subject's time windows, for SLDA (left) and SVM (right).

Finally, the outputs of each subject's test performance from the CTS with the subject-specific windows are collected in the form of confusion matrices and averaged over subjects. The final result is shown in Figure 3.8, where the averaged confusion matrix is displayed for each type of model and window. A lot of information can be extracted from such numerical representation, including the evaluation measures presented in Subsection 2.4.4 for the classification performance, shown on top of each matrix. At the margins of every matrix can be found the percentages calculated over the same direction. On the inferior margin, the blue and the orange percentages are respectively

$$P_{TP,FP} = \frac{TP}{TP+FP} = (1-F)*100 \textit{ i.e. class precision in percentage}$$
$$P_{FP} = \frac{FP}{TP+FP} = F*100$$

Analogously on the right margin,

$$P_{TP,FN} = \frac{TP}{TP+FN} = H*100 \textit{ i.e. the recall in percentage}$$
$$P_{FN} = \frac{FN}{TP+FN}$$

For better visualization, the class-related precision is displayed in Figure 3.9 on the correspondent target location in the 2D grid for every model and window type. This is useful to investigate the distinct performances of different classes (i.e. targets of the robotic movement shown on the screen) and determine possible correlations between a specific type of movement and its neural encoding.
In order to assess if any class is predicted with a significantly different precision compared to others for every model and window type, the class-related precision was collected for every subject as a distribution that was checked to be gaussian through the Lilliefors test, then class-specific distributions were compared with each other in a One-Way ANOVA test, whose results are reported in Figure 3.10. The One-Way Analysis Of Variance (ANOVA) method is used to compare multiple distributions, testing the null-hypothesis

that all their means are equal, and returning the relative *p-value*, the probability that the null-hypothesis is confirmed. The hypothesis is rejected if the *p-value* is lower that the fixed level of significance, chosen here to be $\alpha = 0.05$, meaning as a consequence that the compared distributions are significantly different.

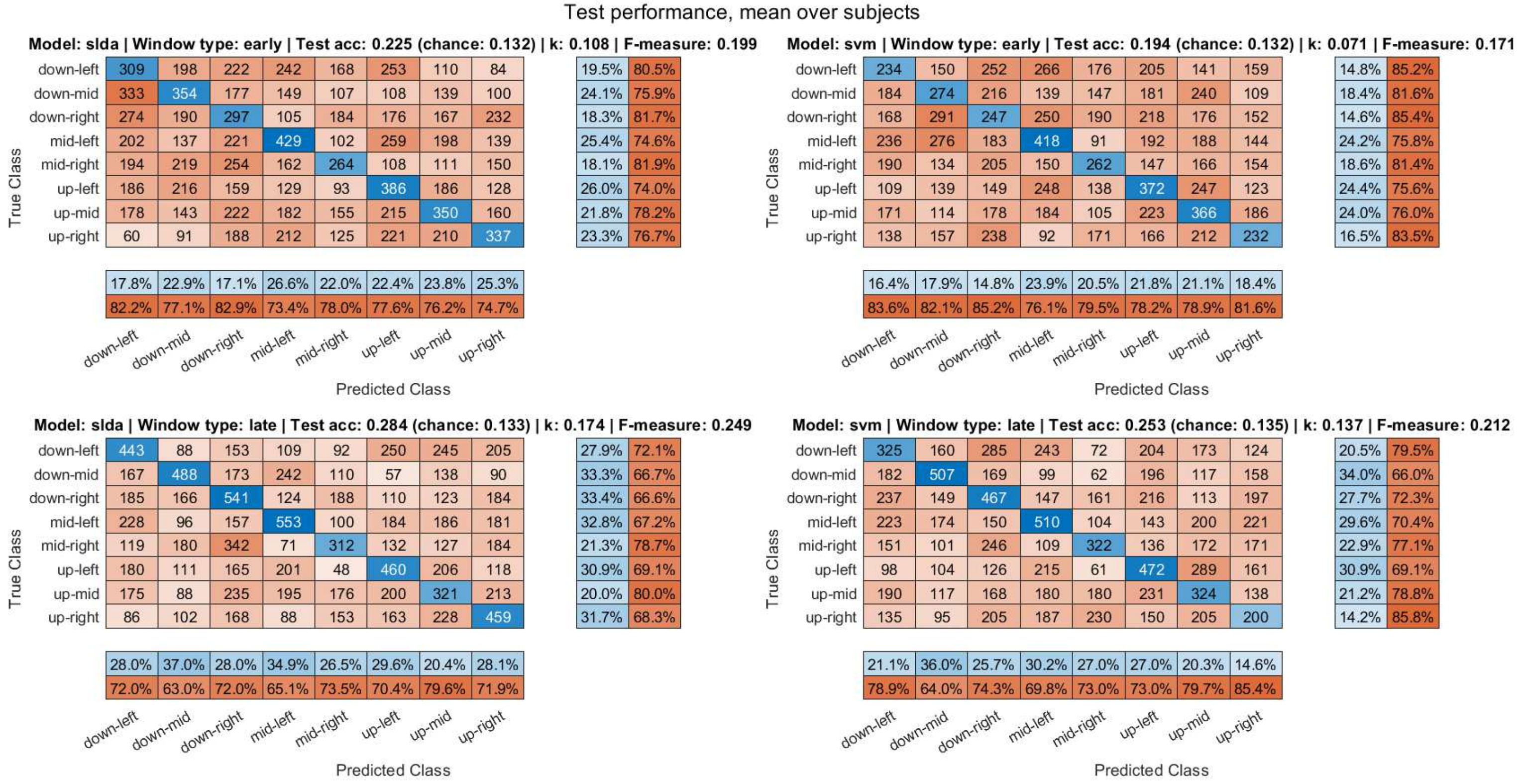

Test performance, mean over subjects

Model: slda | Window type: early | Test acc: 0.225 (chance: 0.132) | k: 0.108 | F-measure: 0.199

True Class	down-left	down-mid	down-right	mid-left	mid-right	up-left	up-mid	up-right		
down-left	309	198	222	242	168	253	110	84	19.5%	80.5%
down-mid	333	354	177	149	107	108	139	100	24.1%	75.9%
down-right	274	190	297	105	184	176	167	232	18.3%	81.7%
mid-left	202	137	221	429	102	259	198	139	25.4%	74.6%
mid-right	194	219	254	162	264	108	111	150	18.1%	81.9%
up-left	186	216	159	129	93	386	186	128	26.0%	74.0%
up-mid	178	143	222	182	155	215	350	160	21.8%	78.2%
up-right	60	91	188	212	125	221	210	337	23.3%	76.7%
	17.8%	22.9%	17.1%	26.6%	22.0%	22.4%	23.8%	25.3%		
	82.2%	77.1%	82.9%	73.4%	78.0%	77.6%	76.2%	74.7%		

Predicted Class

Model: svm | Window type: early | Test acc: 0.194 (chance: 0.132) | k: 0.071 | F-measure: 0.171

True Class	down-left	down-mid	down-right	mid-left	mid-right	up-left	up-mid	up-right		
down-left	234	150	252	266	176	205	141	159	14.8%	85.2%
down-mid	184	274	216	139	147	181	240	109	18.4%	81.6%
down-right	168	291	247	250	190	218	176	152	14.6%	85.4%
mid-left	236	276	183	418	91	192	188	144	24.2%	75.8%
mid-right	190	134	205	150	262	147	166	154	18.6%	81.4%
up-left	109	139	149	248	138	372	247	123	24.4%	75.6%
up-mid	171	114	178	184	105	223	366	186	24.0%	76.0%
up-right	138	157	238	92	171	166	212	232	16.5%	83.5%
	16.4%	17.9%	14.8%	23.9%	20.5%	21.8%	21.1%	18.4%		
	83.6%	82.1%	85.2%	76.1%	79.5%	78.2%	78.9%	81.6%		

Predicted Class

Model: slda | Window type: late | Test acc: 0.284 (chance: 0.133) | k: 0.174 | F-measure: 0.249

True Class	down-left	down-mid	down-right	mid-left	mid-right	up-left	up-mid	up-right		
down-left	443	88	153	109	92	250	245	205	27.9%	72.1%
down-mid	167	488	173	242	110	57	138	90	33.3%	66.7%
down-right	185	166	541	124	188	110	123	184	33.4%	66.6%
mid-left	228	96	157	553	100	184	186	181	32.8%	67.2%
mid-right	119	180	342	71	312	132	127	184	21.3%	78.7%
up-left	180	111	165	201	48	460	206	118	30.9%	69.1%
up-mid	175	88	235	195	176	200	321	213	20.0%	80.0%
up-right	86	102	168	88	153	163	228	459	31.7%	68.3%
	28.0%	37.0%	28.0%	34.9%	26.5%	29.6%	20.4%	28.1%		
	72.0%	63.0%	72.0%	65.1%	73.5%	70.4%	79.6%	71.9%		

Predicted Class

Model: svm | Window type: late | Test acc: 0.253 (chance: 0.135) | k: 0.137 | F-measure: 0.212

True Class	down-left	down-mid	down-right	mid-left	mid-right	up-left	up-mid	up-right		
down-left	325	160	285	243	72	204	173	124	20.5%	79.5%
down-mid	182	507	169	99	62	196	117	158	34.0%	66.0%
down-right	237	149	467	147	161	216	113	197	27.7%	72.3%
mid-left	223	174	150	510	104	143	200	221	29.6%	70.4%
mid-right	151	101	246	109	322	136	172	171	22.9%	77.1%
up-left	98	104	126	215	61	472	289	161	30.9%	69.1%
up-mid	190	117	168	180	180	231	324	138	21.2%	78.8%
up-right	135	95	205	187	230	150	205	200	14.2%	85.8%
	21.1%	36.0%	25.7%	30.2%	27.0%	27.0%	20.3%	14.6%		
	78.9%	64.0%	74.3%	69.8%	73.0%	73.0%	79.7%	85.4%		

Predicted Class

Figure 3.8: Confusion matrices for the four possible combinations of SLDA and SVM with early and late time-window. For each matrix, on the lower margin are displayed the precision (blue) and F (orange) for every class. On the right margin, the value of the recall H (orange). On the upper margin, the title shows the evaluation measures computed in each condition, generalized over subjects and classes.

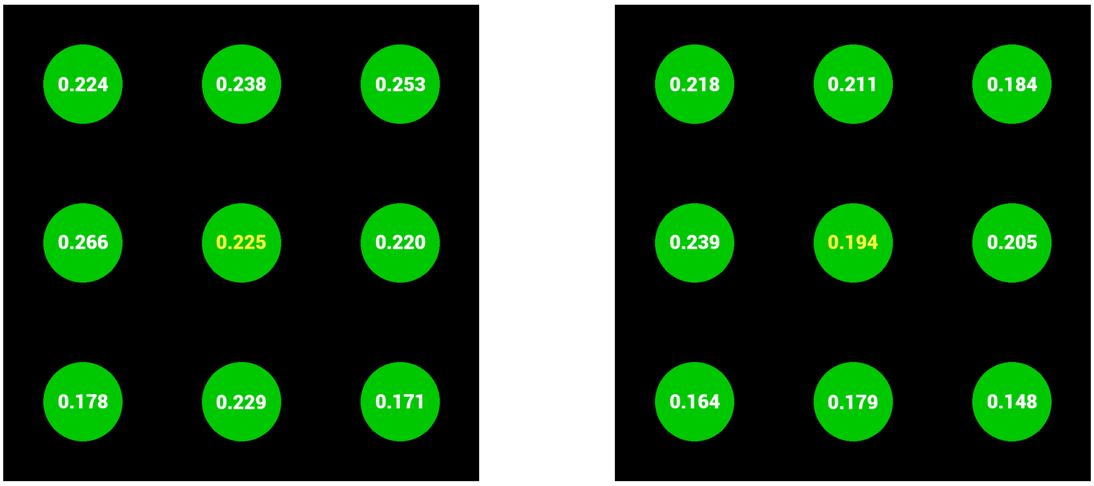
Class-related test precision: SLDA, early window

Class-related test precision: SVM, early window

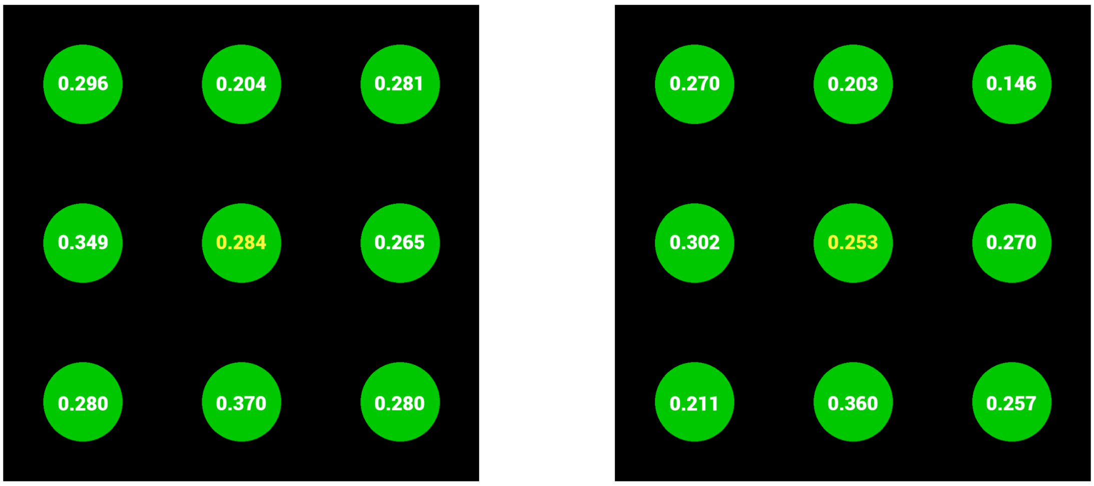
Class-related test precision: SLDA, late window

Class-related test precision: SVM, late window

Figure 3.9: Class-related precision of each class, displayed on the correspondent paradigm target for SLDA with early window (upper left), SVM with early window (upper right), SLDA with late window (lower left) and SVM with late window (lower right). In the middle target, in yellow, the relative test accuracy.

Looking at the overall results, one might question the possible contribution of eye movements in the decoding process, being that the subjects were supposed to trace the movement of the robot with their glance. To answer that, it is possible to go back to

Figure 2.5 to see that eye movements, when not removed correctly, impact most channels depending on their intensity, but mainly the frontal and anterio-frontal locations. Assume having an SLDA model that decodes the target from the EEG of only one channel. Then, assuming the eye movements were not completely removed by the artifact removal preprocessing step, and that they actually give a contribution in decoding the target of the movement from the EEG, such model would have a higher accuracy of classification when decoding only channels in the AF and F rows compared to other rows, or at least close to the maximum accuracy over all channels.

Such process can be implemented to test the hypothesis with the experimental data, running a CTS for all subjects training an SLDA model whose input X_c has $N = 1$, i.e. for channel c, $X_c = X(c, :, :)$. For this process, subject-specific optimal early and late windows were used, and for each of 100 iterations (with different training and test set partition) the accuracy of prediction was collected as the fraction of correct predictions over total predictions, to be averaged over iterations. In the end, having one mean-over-iterations accuracy for each channel and participant, it is possible to average the results over subjects to construct a topoplot of the accuracy for each decoded EEG channel. The outcome of this process is shown in Figure 3.11. It can be observed how there is no significant dominance in accuracy in the anterio-frontal and frontal rows compared to other channels, therefore it is possible to reject the hypothesis that residuals of overt eye movements in the EEG have a contribution in the decoding process.

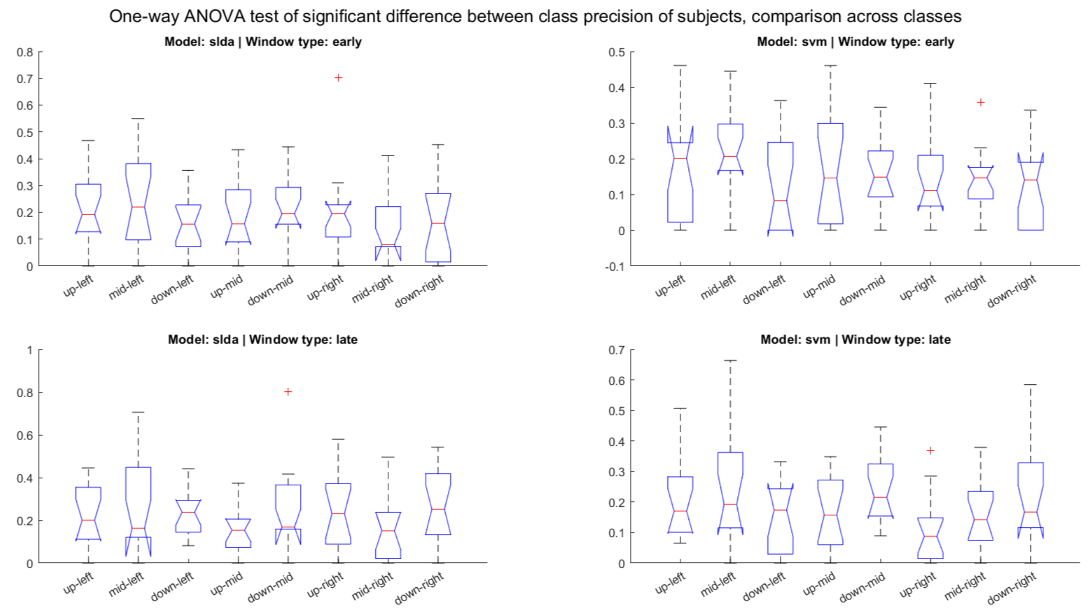

Figure 3.10: Results of the One-Way ANOVA statistical test between the gaussian distributions of the target-specific precision over subjects, compared between targets, for every model and window type

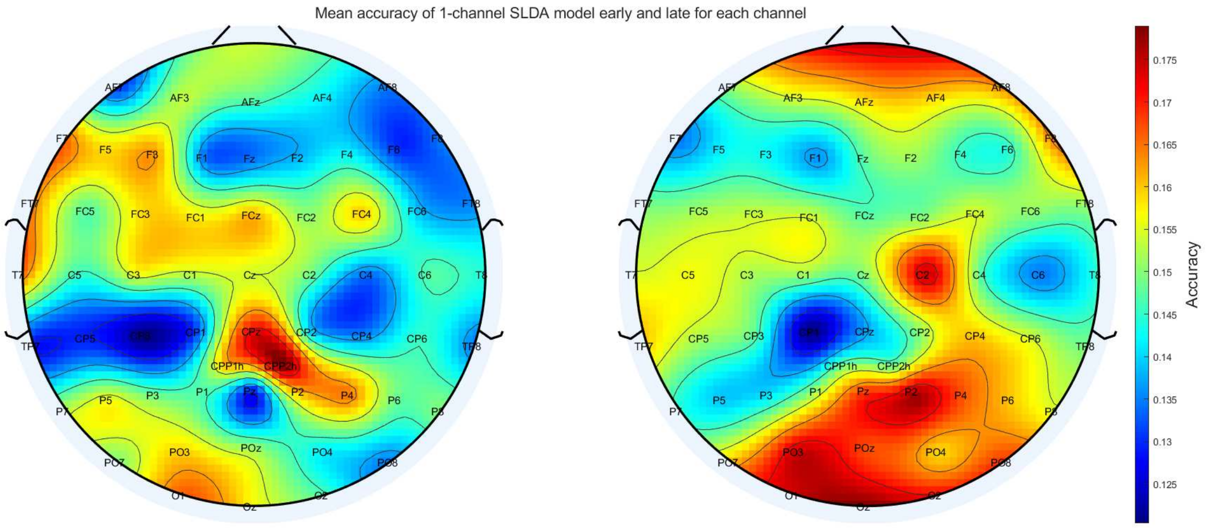

Figure 3.11: Topoplots of the mean accuracy over subjects of the 1-channel SLDA model's predictions using subject-specific optimal early (left) and late (right) windows.

3.2 Regression task

At the end of an RTS, the predicted trajectories of the PLSUKF, the PLSSVM and the PLSRTE can be compared to the true kinematic trajectories, for a qualitative evaluation by directly inspecting the curves, and for a quantitative analysis through the evaluation measures of which at Subsection 2.4.4. In Figure 3.12 the qualitative evaluation can be carried on by inspecting the shapes of the plotted trajectories predicted from the data of the subject with the highest correlation performance. The averaged (over all subjects) Pearson's correlation coefficient between predicted and true trajectories is reported above each plot. Similarly, the chance correlations were obtained by predicting the kinematics from the shuffled trials as described in the RTS algorithm and then averaged over subjects.

Regarding the quantitative analysis, Figure 3.13 shows the distribution of the subjects' performance in terms of correlation coefficient and RMSE for the three types of models used in the decoding. For both correlation and RMSE, each subject's results, averaged over the 50 iterations of the RTS, represent a distribution that is collected and displayed as filled dots on the vertical line related to the type of kinematic and decoder model. On the same line, a circle marks the value of the distribution's median, and a line spans between the 25th and the 75th percentiles. The chance-level correlation is also displayed in the subplot relative to the correlation coefficient, where the black stars between results of the same category mark a statistically significant difference between the performances of the two models. The presence of a significant difference and its level of significance are shown in Figure 3.14, which is the output of the Kruskal-Wallis test with $\alpha = 0.05$, corrected for multiple comparisons and performed over the subjects' performance distributions, which were checked beforehand to be not Gaussian through a Lilliefors test.

The Kruskal-Wallis test is defined as an extension of the One-Way Analysis Of Variance (ANOVA) method: while the latter works under the assumption that the distributions are normal, the Kruskal-Wallis non-parametric test only assumes that the distributions are continuous and of the same type.

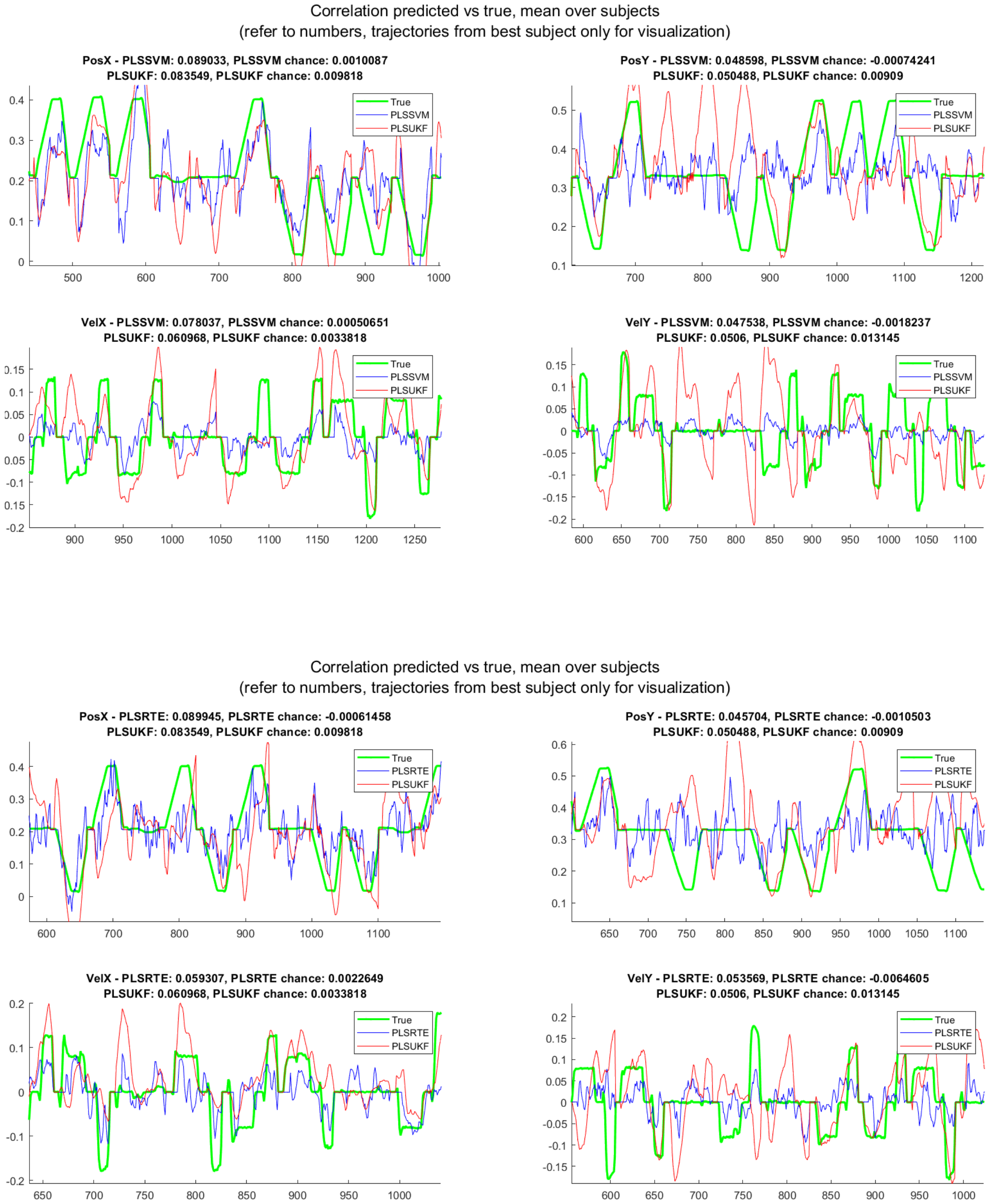

Figure 3.12: Plot of the kinematic trajectories for qualitative evaluation, decoded from the subject whose data resulted in the highest average-over-trials Pearson's correlation coefficient. Above PLSSVM vs PLSUKF, below PLSRTE vs PLSUKF. Above each plot, the model prediction's correlation with respect to the true output, side-to-side with the relative chance-level correlation (averages over subjects). Each subplot is related to a specific type of kinematic: Position X, Position Y, Velocity X and Velocity Y

It can be noted that the PLSSVM and PLSRTE are always, in any type of kinematic trajectory, significantly improving the performance of the PLSUKF in terms of RMSE. Hence, it could be interesting to investigate if such improvement is located in a specific time frame of the observed movement, and to derive which movement characteristics are better decoded by one model or another. To do so, the true trajectories and the predicted kinematics of PLSUKF, PLSSVM and PLSRTE are partitioned along the temporal dimension in windows corresponding to temporal frames of 1 second, shifted by 0.2 seconds from each other. Each correspondent fraction of the true and predicted kinematics is compared and the RMSE is computed restricting to the time window. The result of this computation is shown in Figure 3.15, with a subplot for each kinematics, in which histograms of the results of the three models are placed side-to-side. Interesting conclusions can be derived, for example the fact that the PLSSVM and PLSRTE perform better than (or close to) the PLSUKF in terms of RMSE along the whole movement, and not only during a specific phase of it.

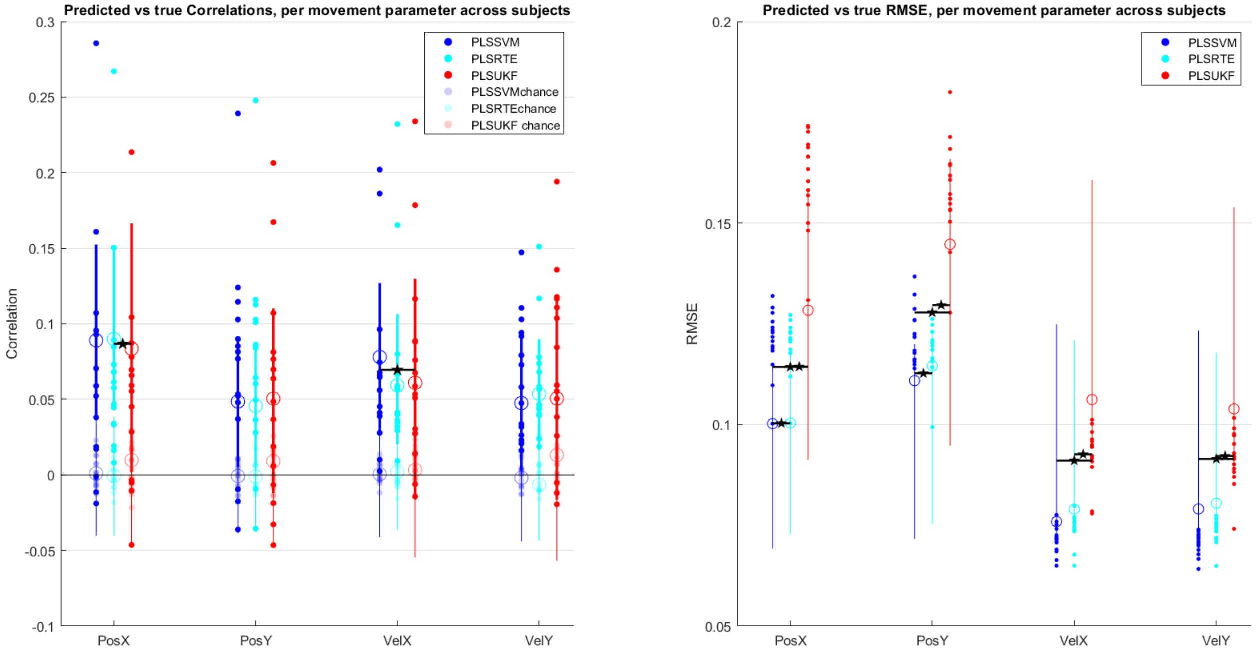

Figure 3.13: Distributions of subject's mean results for each type of performance measure and kinematics (filled dots). For each model, the results of each subject's decoding performance averaged over iterations are represented as a distribution of which the median (empty circle) and the span between the 25th and 75th percentiles (vertical line) are displayed. The black stars mark a significant difference between the performances of two models, as by the Kruskal-Wallis test results below.

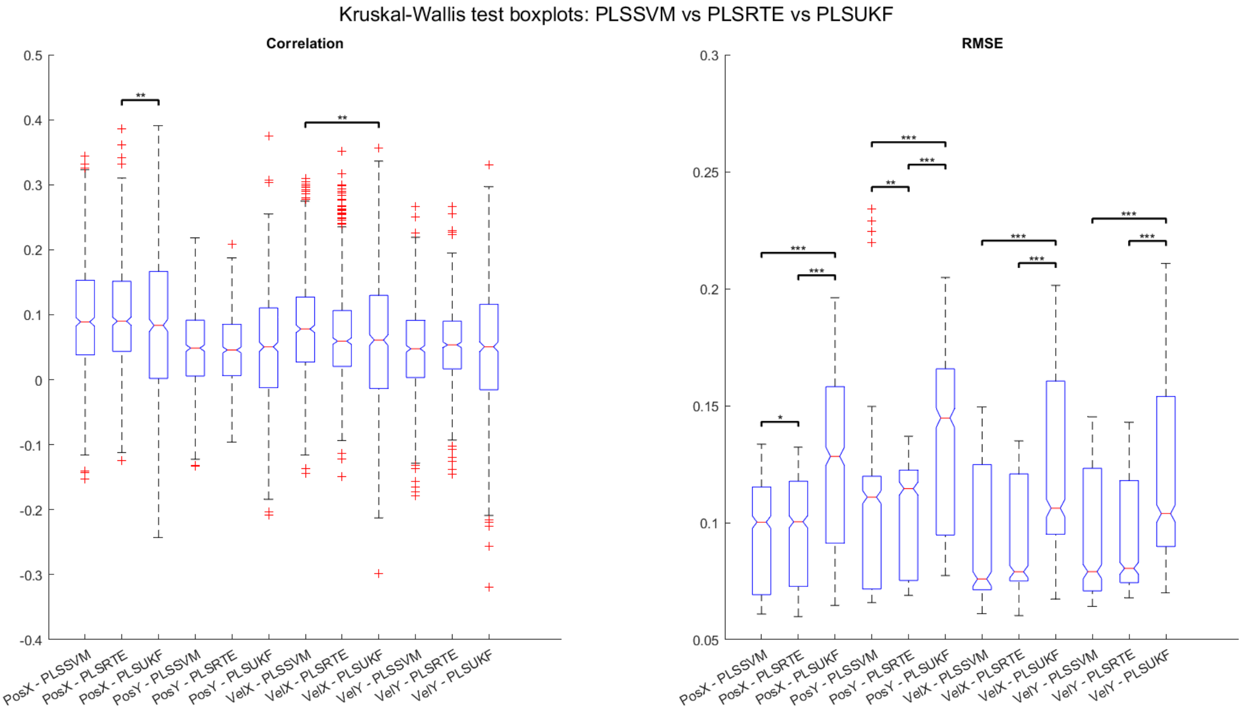

Figure 3.14: Output boxplot of the Kruskal-Wallis test performed on the distributions of the subjects' results for each evaluation measure and type of kinematic. The number of stars displays the level of significance in the difference of two distributions i.e. the performance of two models, based on the relative *p-value*: < 0.05 (1 star), < 0.01 (2 stars) or < 0.001 (3 stars)

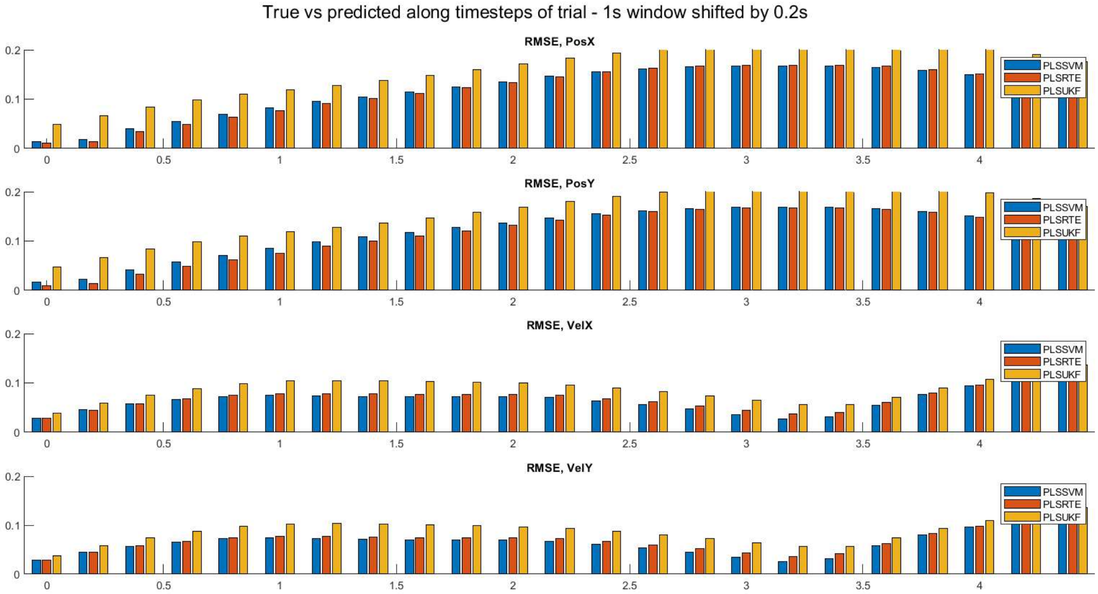

Figure 3.15: RMSE histograms along trial time-steps, comparison between PLSUKF, PLSSVM and PLSRTE for each type of kinematics

3.3 Patterns of Event-related Desynchronization

One of the two outputs of the processing phase of the *robotruns* is solely used to construct the ERDS maps: the "rest" period considered and depicted in Figure 2.4 is a window of 0.2 s before the auditory stimulus is delivered, a fraction of time when the subject has acknowledged the location of the target and is idling, waiting for the task to begin but not already focusing on it. Considering as the trigger of the activity the sound stimulus delivery, the event-related de/synchronization reported in Figure 2.1 is computed for each subject in alpha and beta and then averaged over subjects to detect commonly occurring patterns. The plots are computed at every time step of the EEG with 200 Hz-sampled data, then the most interesting frames are displayed in Figure 3.16. Timings and significant events are reported above the correspondent activation map, which is linked to the correspondent fraction of the kinematic trajectory. Since the activity shown is the average of the activity induced by several different types of trajectories, the one that is displayed is simply a reference of the action's kinematic behavior as a function of the time, which turns useful when associating the activity to the phase of the movement. Figure 3.16 gives insight into the activity elicited by the general observation of movement, starting at the beginning of the action ($\sim$ 0.5 s after the start marker) in the mu and beta band, and its evolution in time along the trial, to be compared with the known effects described by the literature in Section 1.2.

In the mu band, this phenomenon is more intensively located in the central, parietal and parieto-occipital areas of the cortex, specifically in the neighborhoods of CPz and CP2, then briefly in C5, P5-P3 and in the rightmost part of the parieto-occipital regions during the first part of the movement captured by W2. The de-synchronization peak around P4-P6 later stabilizes around the slightly lower PO4 and PO8 during the linear target-directed progression of the movement enclosed in window W3. In this phase, some areas show weaker effects of de-synchronization, precisely around the electrodes C3-FC3 and C4-C6, becoming less distinguishable but being still present during W4, i.e., as the hand gets closer to the target. While the hand is still on the target (window W5), a strong activation is observed in the parieto-occipital areas (PO7, PO8). As the fast movement back to the initial position starts (window W6), synchronization appears bilaterally in the electrodes CP3, CP5, CP4, CP6, switching to strictly contralateral and then to ipsilateral de-synchronization around C4 in the last part of the action.

In the beta band, a strong de-synchronization arises during W2 in the rightmost part of the parieto-occipital regions and in a weaker but distinguishable way in the C4 electrode mainly. Progressing to W3 and W4, the parieto-occipital beta suppression extends to become bilateral, with the central electrodes that appear slightly more synchronized. Finally, as the faster movement back begins (window W6), the synchronization in the fronto-central and parieto-occipital regions gradually fades, and de-synchronization increases around electrodes C4 and CPP2h.

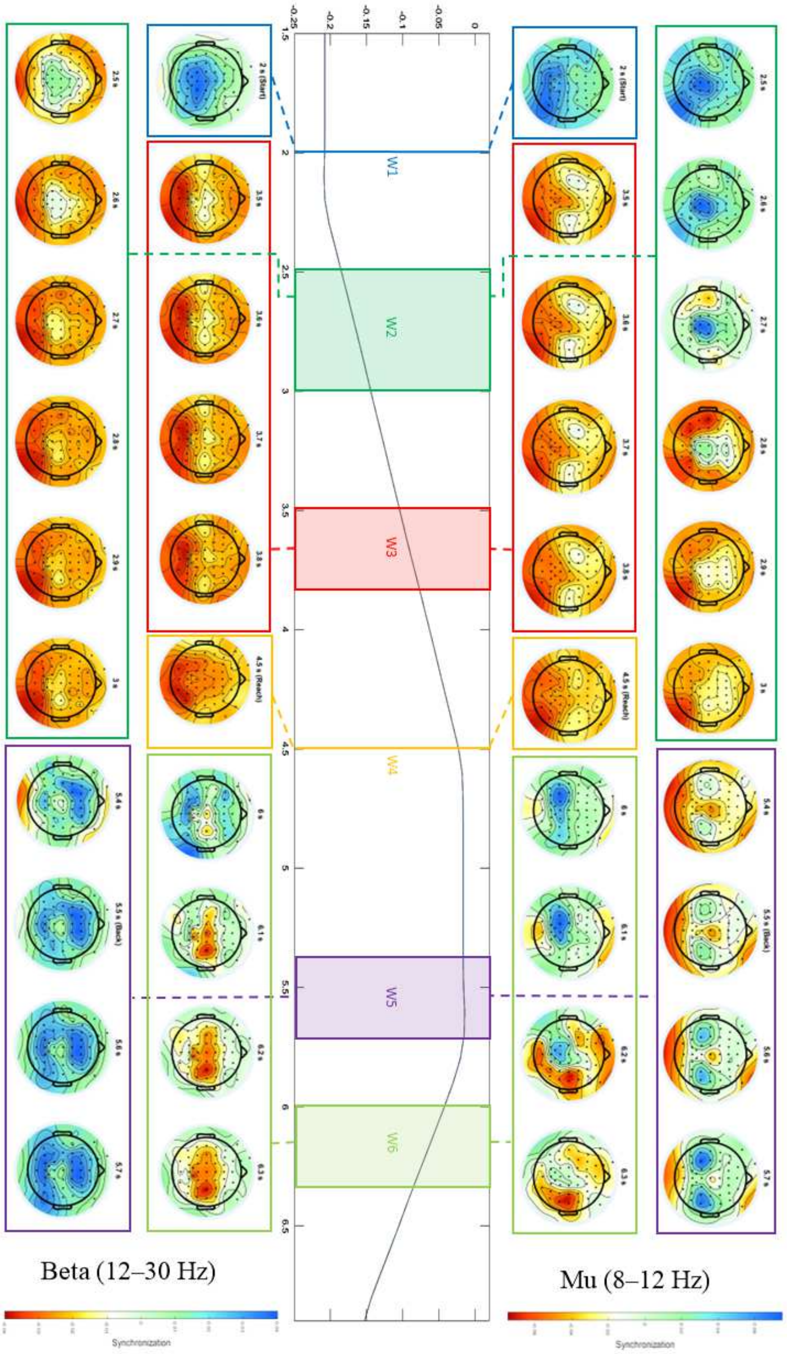

Figure 3.16: Event-related Synchronization maps during the *robotruns* in mu and beta band, averaged across all trials and all subjects and according to the montage in Figure 2.2. The trial's timing are displayed above the correspondent activation maps, sequences are paired to the correspondent phases of the kinematic trajectory. Windows of interest: W1 - Preparation of the movement, subject waiting for JACO to move knowing the destination; W2 - Movement onset; W3 - Movement starts progressing toward the target; W4 - Movement progressing, halfway through; W4 - Movement reaches the destination; W5 - Hand stable on the target; W6 - Movement progressing fast toward the home position;

The ERDS maps are also calculated from the trials divided by their associated movement target, independently for each subject and then averaged over subjects for each target label. This captures the areas and magnitude of activation that depend on the specific type of movement in the space, which shows more interesting features in the mu band than in the beta band. The resulting target-specific time-varying mu suppression maps can be subtracted by their opponent along a certain direction, in order to capture the difference between the activation evoked by movement towards targets that are opposite along that direction. Therefore, by averaging the difference between the upper-left and upper-right (1 and 7) targets, the middle-right and the middle-left (2 and 8) targets, and the lower-right and the lower-left (3 and 9) targets, the change in the activation bound to the difference between left-directed and right-directed movement can be investigated separately from the vertical direction. If the activation related to right-directed movements is subtracted from the one of the left-directed, the channels that exhibit de-synchronization at a specific point in the first case but not in the second case will result in a negative difference in the resulting map and vice versa. Therefore, in a single activation difference map, positive values are associated with a de-synchronization linked to the observation of right-directed movement, and negative values with a de-synchronization linked with left-directed movements. The same can be done in a similar way for the change between upward and downward movements regardless of the horizontal component. The most interesting fractions of a trial's timing (in terms of directional difference of activation) are displayed in Figure 3.17 for the horizontal direction, and in Figure 3.18 for the vertical direction. In both cases, the intervals are paired with the correspondent phase of the movements, visualized as a generic kinematic trajectory in the same fashion as Figure 3.16.

In Figure 3.17, the difference of suppression is investigated along the horizontal direction, recalling that negative values are attributed to de-synchronization induced by movements directed towards targets on the left (and eventually synchronization by targets on the right), and vice versa for positive values. Based on this, the activation maps show de-synchronization increasing during the preparation of the movement captured by window W1 (0.6 s - 1 s) ipsilateral to the direction of the target from the center. At the beginning of the movement (window W2), right-directed movements induce mu-suppression in the ipsilateral central areas, around C2 and C4, whereas left-directed movements have more influence in the ipsilateral parieto-occipital regions. As the robotic arm progresses toward the destination (window W3), left-oriented movements show to produce de-synchronization in the mu band located in the somatosensory left cortex, at locations CPz, CP1 and CPP1h, later shifting towards the same hemisphere's parieto-occipital sulcus. De-synchronization related to right-oriented movements in this phase does not have remarkable features at the beginning, but shows a considerable increase later in the left-hemisphere parieto-occipital sulcus. Finally, during the start of the movement back to the initial position (window W5), it can be observed how mu-suppression related to left-directed movements is located at ipsilateral centro-parietal sites, around C2 and CP5, while the one related to right-directed movements is located in the slightly-contralateral parieto-occipital area, in POz towards PO3. Progressing towards the initial position, in the left target case (which, in the action going back, results in a right-directed movement) mu-suppression is located in the right hemisphere, in the occipital areas, while the same areas in the left hemisphere show de-synchronization in the case of the right target case (left-directed movement back).

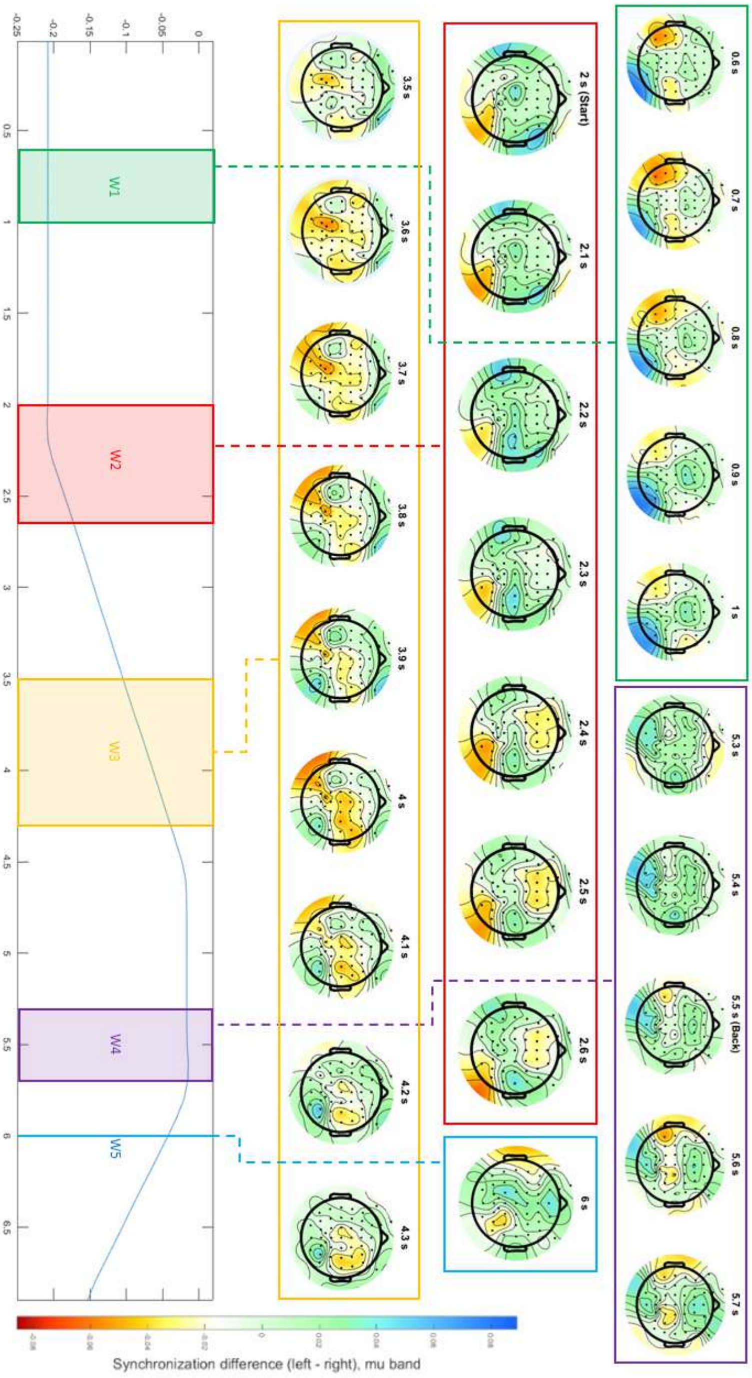

Figure 3.17: Directional event-related Synchronization maps during trials in mu band. The ERS (average across subjects and within the mu band) related to leftmost targets is subtracted by the ERS related to the rightmost counterpart, the resulting differences are averaged to produce the directional activation difference maps along the horizontal direction. Windows of interest: W1 - Preparation of the movement, subject waiting for JACO to move knowing the destination; W2 - Beginning of the movement and start of progression toward the target; W3 - Movement progressing toward the target, halfway through; W4 - Hand stable on the target; W5 - Movement progressing fast toward the home position;

For what concerns the vertical directional difference in de-synchronization, through the inspection of Figure 3.18, and recalling that negative values of synchronization difference in the maps are attributed to upward movements de-synchronization and/or downward synchronization and vice-versa for the positive values, we first notice that the absolute range of difference expressed by the color bar scale is halved compared to the horizontal case. Considering that the scale spans from the maximum to the minimum values in the set of displayed maps, and that the latter includes only maps where differences are more visible, we can conclude that differences in the activity are in general less strong and evident when the target changes along the vertical direction. Despite that, it is possible to observe a directional difference during the movement preparation (window W1, 0.5 - 1 s), with upward movements inducing de-synchronization in the centro-parietal region, bilaterally in CP5 and CP6, and downward movements in the strictly occipital region, slightly more in the right hemisphere. Getting closer to the movement onset (window W2), the negative difference in the left frontal and right parieto-occipital and a positive difference in the somatosensory region leave place for mu-suppression induced in the right parieto-occipital by the upward movement, and in the left parieto-occipital by the downward movement. During the approaching action towards the target, first during W3 the activity exhibits high de-synchronization induced by upward movements in the left somatosensory cortex, later expanding in the adjacent parieto-occipital and then in the centro-parietal region during W4. As the movement back to the initial position starts (window W5), a strong mu-suppression arises induced by the upward movement in CP5 and P5, but in this case, the onset does not exhibit clear activity opposition at different directional conditions, as the downward movement seems to only partly induce de-synchronization in the frontal and centro-parietal regions. During the progression of this movement toward the destination (window W6), a brief distinction can be observed in the mu-suppression, which is localized for the downward movement in the left hemisphere's somatosensory region and in frontal sites, while for the upward movement, it appears in the right hemisphere's parieto-occipital region.

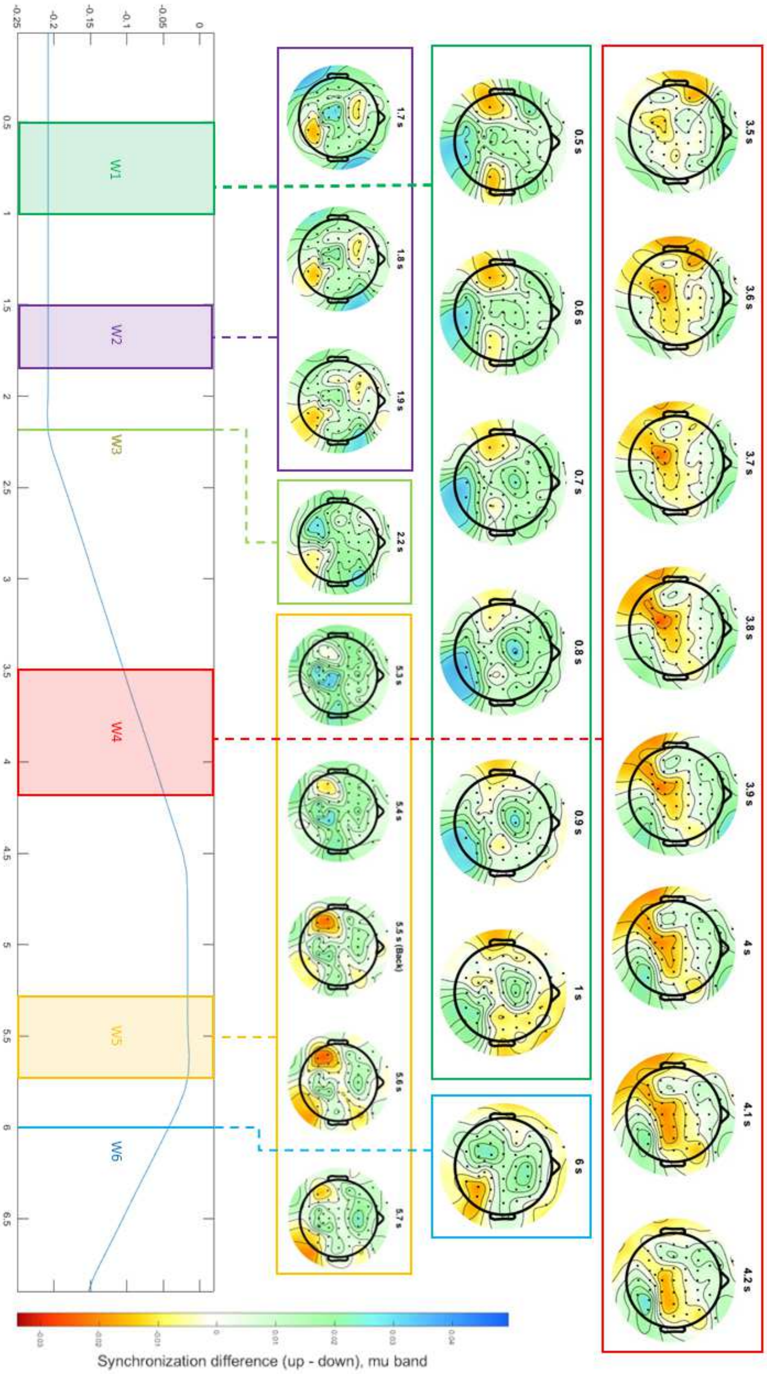

Figure 3.18: Directional event-related synchronization difference maps during trials in mu band. The ERS (average across subjects and within the mu band) related to the uppermost targets is subtracted by the ERS related to the lowermost counterpart, the resulting differences are averaged to produce the directional activation difference maps along the vertical direction. Windows of interest: W1 - Preparation of the movement, subject waiting for JACO to move knowing the destination; W2 - Latest progression of movement preparation; W3 - Movement starts; W4 - Movement progressing toward the target, halfway through; W5 - Hand stable on the target; W6 - Movement back to the home position initiated

The previous analysis of the directional difference is conducted only by visual inspection and does not rely on any quantitative proof yet. In order to support the validity of the reasoning, a statistical analysis is performed: for the horizontal and vertical directions separately, the ERD difference is averaged within the relative windows of interest, producing one topoplot for each of them. Successively, the electrodes are divided in 6 Regions of Interest (ROI), as depicted in Figure 3.19: Regions FCL and FCR comprising the Anterio-Frontal, Frontal and Fronto-central areas of the left and right hemispheres respectively, regions CPL and CPR for the Central and Centro-Parietal areas, and regions POL and POR for the Parietal, Parieto-Occipital and Occipital areas. The De-synchronization directional difference of locations within an ROI is treated as a distribution of values that is compared with the other ROIs' distribution in a One-Way ANOVA test corrected for multiple comparisons. This allows us to obtain a statistical comparison of directional differences within a region on average for each temporal window of interest, and determine where synchronization or de-synchronization is most dominant during that event.

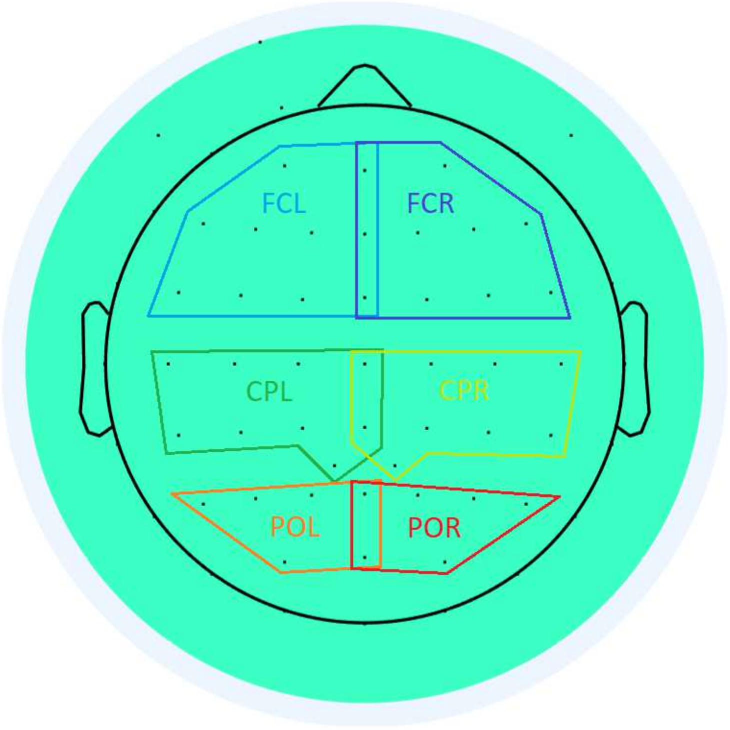

Figure 3.19: Partition in ROIs for the statistical analysis of ERD directional difference. The regions roughly depict the regions of the brain that are affected by approximately separate directional changes along the trials.

Regarding the horizontal direction, the results of the ANOVA test are displayed in Figure 3.20, where the mu-suppression related to left-directed targets is subtracted by the one linked to right-directed targets at each electrode, on average within the relative time window. For clarity, such difference corresponds to the right-targets synchronization subtracted by the left-targets synchronization, so the negative of Figure 3.17, where higher negative values were associated with higher suppression and lower synchronization level. The reason this was done is that the final target of this analysis is the mu-suppression, the key feature of the observation of movement in the EEG. Hence, it is easier to understand from these graphs how its behavior changes with the spatial coordinates of the destination if the suppression (i.e., the de-synchronization) is displayed directly, rather than as the negative of the synchronization as in 3.17.

The figure can be inspected to see that it confirms the intuitions derived from the visual inspection of the synchronization difference: the mu-suppression difference is significantly higher in the ipsilateral parieto-occipital region for right-directed targets (blue area in the W1 topoplots at Figure 3.17), while it is not significantly higher for left-directed targets, but still present in the ipsilateral centro-parietal and parieto-occipital regions. It is interesting to see that all ROIs carry a negative difference regardless of the significant discriminant, meaning that during this phase all areas of the brain might be more active in terms of alpha band de-synchronization when focusing on right-sided targets. Then during the beginning of the action, mu-suppression is significantly higher in the ipsilateral centro-parietal ROI for right-directed reaching actions, and in the ipsilateral parieto-occipital ROI for left-directed reaching actions, and all ROIs now show stronger mu-suppression linked to left-directed movements, regardless of significantly discriminant features. During the target approaching phase captured by window W3, the mu band de-synchronization is significantly higher only in ipsilateral parieto-occipital for right-directed movements, but more weakly than in the previous cases, since the absolute range of difference is also lower (0.2 times the range of W1, 0.13 times the range of W2), and weakly unbalanced toward overall negative values. During window W4 the hand is on the target, and the strongest discriminant is the mu-suppression difference between the centro-parietal left ROI for left-directed movements, and the parieto-occipital left ROI for the right-directed ones. Lastly, as the fast movement back starts, a generally negative difference of mu-suppression is observed, but with no significantly remarkable features.

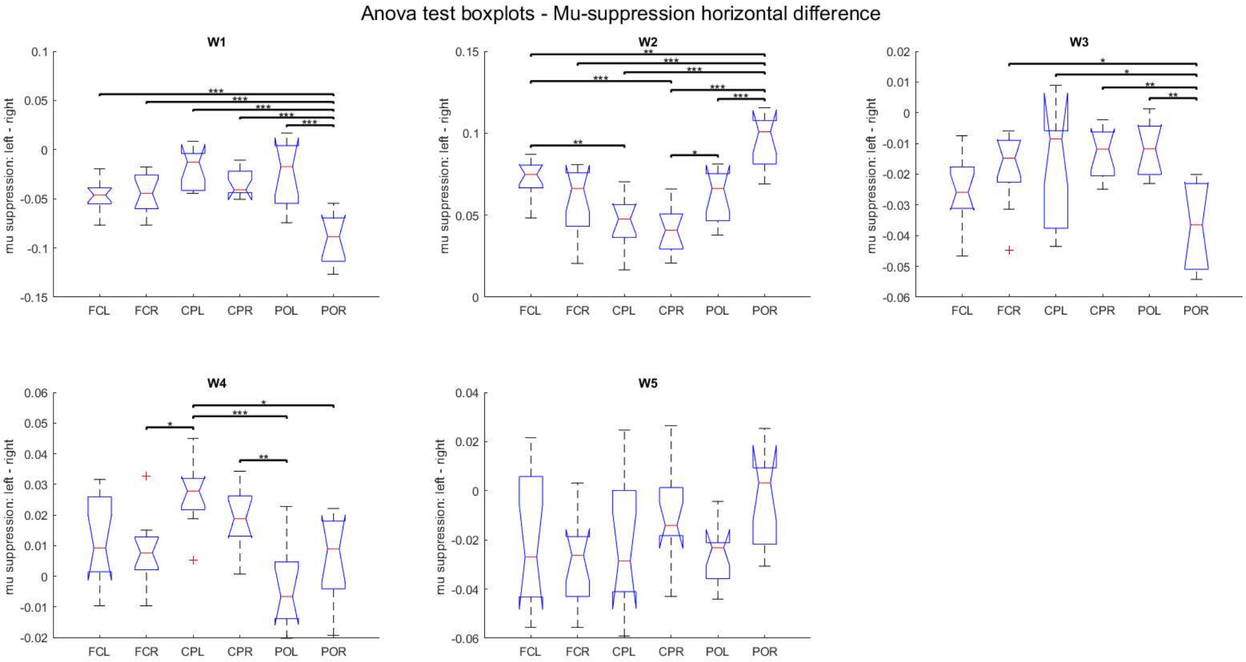

Figure 3.20: Mu-suppression horizontal difference ANOVA test. The windows of interest follow the nomenclature of Figure 3.17, the naming of the ROIs follow the convention at Figure 3.19.

A similar procedure is done for the vertical mu-suppression difference, shown in Figure 3.21. in this case, the preparation of movement induces a generally negative difference, i.e., stronger mu-suppression bound to lower targets, with a significantly stronger contribution by the right parieto-occipital region for lower targets. The latest phase of the preparation captured by W2 shows a different pattern compared to W1, where all ROIs show a similar trend but flipped over the abscissa axis, hence linked to generally stronger mu-suppression for upper targets, and more significantly in the left fronto-central and the right parieto-occipital. The start of the movement marking the W3 interval induces a mu-suppression difference pattern roughly similar to the previous interval. The trend flips again, increasing in the general negativity bound to stronger mu-suppression for down-directed movements especially in the parieto-central and left parieto-occipital ROIs, whereas the strongest positivity bound to mu-suppression induced by the observation of up-directed movements is found significantly higher again in the right parieto-occipital. The stationary fraction of the trial framed by W4 shows no apparently remarkable difference in the mu-suppression relative to different vertical spatial coordinates of the target, instead, the fast movement back seems to elicit significantly stronger mu-suppression only in the left parieto-occipital ROI for up-directed movements.

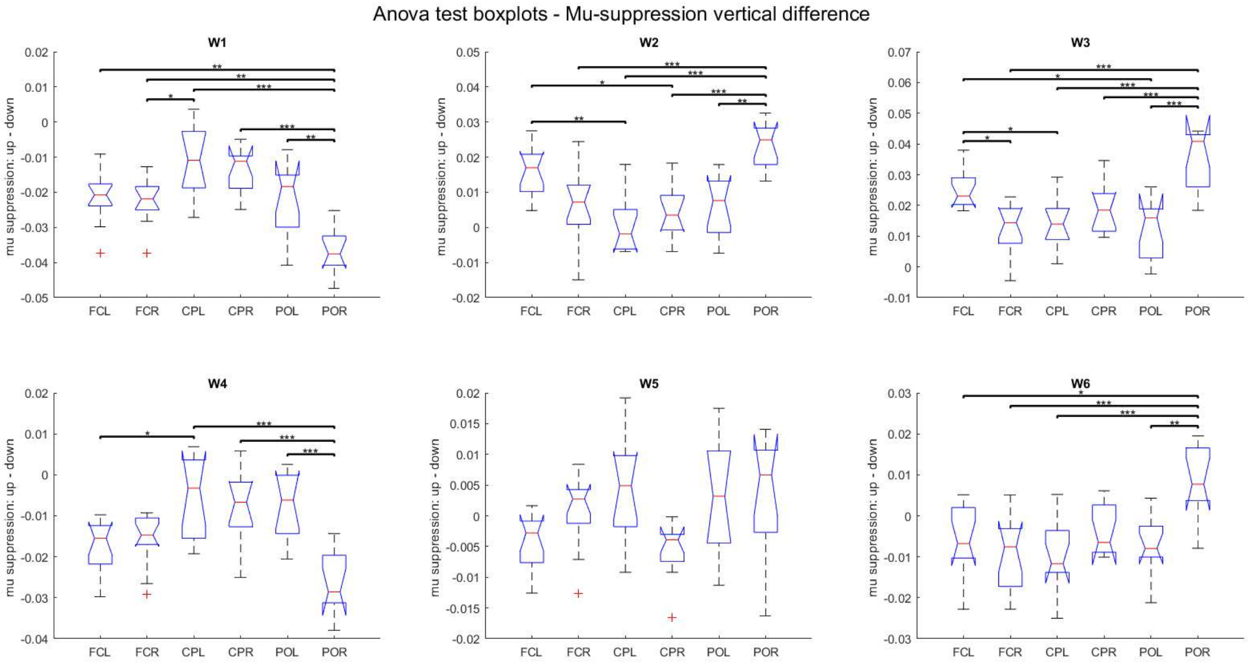

Figure 3.21: Mu-suppression vertical difference ANOVA test. The windows of interest follow the nomenclature of Figure 3.18, the naming of the ROIs follow the convention at Figure 3.19.

CHAPTER 4

Discussion

After having explored the cutting-edge founding principles behind the decoding of the neural activity related to the observation of center-out target-oriented robotic movements, it is possible to draw some conclusions by analyzing the results shown in Chapter 3. The structure of this part is composed of a brief, general discussion on the topic of motor observation and related issues. Then, the discussion shifts toward the results of the decoding task and the ERDS patterns, in the same order as the previous chapter.

Commencing from the current state-of-the-art in the field, it can be said that Motor Observation can be a hard task for decoding, as the movement-related neural activity, elicited by the effect of the HMNs, can be way harder to extract from the EEG compared to other movement-related tasks such as ME/MA or MI. Moreover, it should be kept in mind that fixating the subject's gaze toward a point is a commonly adopted approach in ME/MA and MI tasks to make the decoding of the target cortical activity easier. In the task of Motor Observation this is not allowed, therefore oculomotor and visual processing correlates mix unavoidably with the movement-related neural activity. For this reason, making use of an artifact removal process with a high level of reliability is necessary to allow the correct and total deletion of artifacts that may influence the decoding, either by overshading the less-visible movement-observation-related EEG or by inducing the decoder model to decode oculomotor activity instead of that.

Thanks to the contribution of the Institute of Neuroengineering of the TU Graz in the development and application of techniques that ensure a safe extraction of the hidden activity of interest, it was possible to prove that in this work, what is decoded is indeed the neural movement-observation correlates. The proof of this comes from the inspection of the pre-processing outputs example at Figure 2.5, and from the 1-channel model analysis introduced in Section 3.2 and whose results are displayed in Figure 3.11. It must be said that the latter is too naive to deduce with a significant degree of certainty the location and the causes of the activity used for the target class decoding, but its main purpose is to rather show that the channels where eye artifacts have the most influence do not contain enough information for decoding the target properly when taken singularly.

Classification task Regarding the results of the classification task, for what concerns the effects of the trial's temporal behavior in the decoding reported in Figure 3.7, the early window becomes more important compared to the late window for two main reasons: first, the earlier it is possible to get the most accurate prediction, the better it is when dealing with applications of the decoding, e.g., setting up a baseline for actively commanding the robot with the neural activity. Moreover, the fraction of the trial where the movement is happening, i.e., the early window, is surely correlated to the movement and the effects of its observation in the brain. On the other hand, it is harder to find a direct correlation between the late window and the movement, being that it includes the period of time where the robot is stable at the arrival point and a faster "target-oriented center-in" movement. It could be argued that the movement that goes back to the initial position can be still regarded as a target-oriented action with the target being the central initial position. The participants were instructed to observe that movement as well, because it helped to maintain the focus on the task, moreover, we have seen from the ERDS patterns that similar motor-observation-related behaviors occur during both actions, so at that point the only difference between the two movements would be represented by the action's speed. Having shown in the analysis at Figure 3.6 that this hypothesis is unlikely to be true, it still remains an open question what type of information is decoded to obtain such high accuracy.

Regardless, observing Figures 3.1 and 3.2 it is possible to observe that the accuracy has a high variance, possibly because of the little quantity of data used for the training and evaluation and in the computation of the chance level accuracy. In fact, the scarcity of available data in the TWSS results in a model trained on approximately 0.48 times the total number of trials and validated on 0.12 of them (i.e., one k-fold). This is repeated 5 times for the same fixed random trial partition of k-folds and test set, and averaged over them, then further repeated for 50 different partitions. Due to these low numbers, one instance of a model during a TWSS could easily encounter a bias in the selected random partition, resulting in a more "lucky" or "unlucky" training and validation trials combination and therefore in a higher or lower accuracy respectively. This issue affecting the data explains both the high variance of the validation accuracy and also the overestimated value of the chance-level validation accuracy, estimated as the 95th percentile of a distribution with a high variance.

This effect can be attenuated in two ways: increasing the dimension of the dataset or increasing the number of iterations. The first strategy is adopted with the generalized model in Figures 3.3 and 3.4, where the much higher quantity of available data (15 times more) allows not only to obtain a lower variance in accuracy, but also a "less overestimated" chance accuracy computation, with an approximate decrease of $\sim 27\%$. Since the generalized model by definition must have values of parameters that do not take into account the specificity of an individual's brain activity, a subject-specific model of the type used in the processes originating Figures 3.1 and 3.2 would probably perform better than the generalized in terms of validation accuracy compared to the correspondent chance accuracy if provided with the same quantity of data of the latter.

The second strategy is adopted in the CTS: there, a model instance is trained on 0.8 of the total number of trials and evaluated on 0.2 of them for a considerably higher number of iterations than in the TWSS. Therefore, by increasing the number of samples of the distribution of the test accuracy and chance test accuracy over iterations, its variance is

lowered and so is the final estimation of the chance-level test accuracy, as can be observed from Figure 3.8.
From Figure 3.8 it is possible to extract some more insight: the test accuracy increases by 0.06 by using the late instead of the early window, both for SLDA and SVM (21% increase in the first, 24 % in the second). In both types of windows, SLDA has a 0.03 better accuracy than SVM, and regardless of the combination they all lead to accuracy values that are consistently above chance level. Cohen's kappa and F-measure are in all cases attributed to a slightly better-than-chance predictor, coherently with the results in accuracy, measure with which they also share the increase or decrease trend depending on the model and window type. By inspecting the class-related precision it can be observed how classes that are related to negative Y coordinates, i.e. the ones labeled "down-", seem to be the most mispredicted by the decoding in the early window. This would be sustained by several previous studies on motor decoding, where the vertical coordinate showed to be the most difficult component to decode from the EEG. Still, in this case the One-Way ANOVA test showed in a rigorous way that no class is actually predicted significantly better or worse than any other.

Regression task Relative to the regression part, it can be seen how all models have results that are significantly above chance-level according to the quantitative performance results displayed in Figure 3.13, validating the conclusion that with either PLSSVM, PLSRTE and PLSUKF it is indeed possible to extract from the EEG the continuous kinematic behavior of an observed movement. Regarding the model comparison, the PLSUKF algorithm can be affected by an overshoot problem for this kind of kinematic trajectories, and this can be deduced by inspecting the predicted trajectories in Figure 3.12. It is not new that this particular type of center-out semi-discrete trajectory can be a source of complications in the decoding: some model testing was performed before the experimental data was available to get a starting point in the model comparison for regression, using data kindly made available by Pulferer from the study of Pulferer et al.[53] in the "100% snake condition". While several deep learning architectures like BiLSTM, LSTM and CNN gave promising results with those continuous snake trajectories despite the moderate quantity of data, the center-out trajectories (and possibly, weaker neural activation of motor observation compared to motor imagination) of the current study invalidated the applicability of the previously obtained results in this task and setup. Instead, the PLSUKF model giving good results already in the previous model testing, survived the change of application. Nevertheless, the principle of recurrent update the design of the PLSUKF is based on makes it more suitable for decoding continuous smooth outputs, hence it makes sense that its decoding capabilities are affected by issues such as early-stage overshoot and range exaggeration in the case of semi-discrete targets. The PLSSVM algorithm was designed to solve this issue and enhance the results of the PLSUKF: thanks to the regularization induced by the box constraint — hyperparameter set to favor a less strict separation of the kernel output points by the linear hyperplane — it was possible to obtain predicted trajectories that, despite being affected by more jittering, were closer in range to the true trajectories. The consistent improvement can be noticed qualitatively from the trajectories, and quantitatively from the results of the Kruskal-Wallis test in the correlation and RMSE measures. The attempt at further improving the performance was done by designing the PLSRTE algorithm, using a different non-linear mapping between the latent space features and the kinematics consisting in the decision tree ensembles. Figure 3.13 shows that the PLSRTE significantly improves the decoding of the horizontal position, while the PLSSVM is significantly better in decoding the horizontal velocity. Moreover, the RMSE is better in the case of the trajectories decoded by the PLSSVM compared to the ones of the PLSRTE, despite the moving average filtering that was applied in the second case. Regardless of the difference between them, they both perform better or close than the PLSUKF, significantly improving the decoding in 62,5% of the cases and more consistently in the RMSE, whose median is enhanced by $\sim 23.5\%$ on average. Interestingly, PLSUKF, PLSVM and PLSRTE can be seen to predict trajectories that roughly follow the same trend (See Figure 3.12). This suggests that the part of the algorithms that could affect more consistently the performance is the only common component between them, i.e. the dimensionality reduction performed by the PLS. The task of substituting the Partial Least Squares (PLS) with a more efficient information compression strategy, in order to enhance the decoding of observed kinematic trajectories from the EEG, remains a potential objective for future research.

Patterns of Event-related Desynchronization Lastly, to discuss the Event-related Desynchronization patterns it is possible to inspect the maps in Figure 3.16. It can be observed that the suppression in the mu and beta bands has similar patterns: it starts together with the movement in the rightmost parieto-occipital cortex, the weakest suppression during the target-directed movement is localized bilaterally in the central line, and during the fast movement back the de-synchronization is higher around C4. These results are coherent with the literature analyzed in Section 1.2, where the observation of movement was reported to induce mu suppression mainly in the posterior parietal and occipital regions and less strongly in central areas, linked with the activation of the hMNS, but also to induce beta suppression in the centro-parietal areas.

Whereas these results can be obtained from the average de-synchronization over subjects and targets to assess the general effects of the observation of the robotic movement and compare them with the state-of-the-art literature, a different type of discussion can be drawn from the comparison of the ERDS maps associated to different targets as done in Figures 3.17 and 3.18, with the focus of discriminating activity related to a specific type of directional movement.

The first interesting directional difference can be noticed during the preparation of the movement and could be correlated to the phenomenon of covert visuospatial attention (CVSA), which is the preparatory attentional process of focusing the attention on a region of the visual field without overt eye movements, i.e. general eye movements that physically direct the eyes to a stimulus, like saccades or slow target-tracking movements. From the literature, the EEG correlates of CVSA are attributed to activity in the alpha band, ipsilateral with respect to the cued side (left or right) of attention, moreover the topographical distribution of the alpha-band activity changed if targets were in the upper or lower visual field location [62] [70]. Such behavior can be found in the context of this study during the specified phase of the movement, in which the subjects already knew where the target was located, but their gaze is locked on the robot's hand, waiting for JACO's action. This suggests that, during this interval of time, covert visuospatial attention could be one of the overlapping effects to compose the overall induced brain activity.

Altogether, three main patterns of interest can be found in horizontal suppression difference maps: the first stems from the phenomenon of CVSA, as stated before. The second

is at the onset of both movements, more visible by inspecting the maps at time 2.2 s (1) and 5.6 s (2), where de-synchronization is observed for the right-directed movement (positive/blue values in (1); negative/red in (2)) around C2 and CP5, and in the parieto-occipital cortex in the left-directed case (negative/red values in (1); positive/blue in (2)), contralateral to the direction of the destination of the movement. The third pattern is present as the arm approaches the target, when mu-suppression is present ipsilaterally to the target's side in the parieto-occipital region. This effect is also present during the movement back, inverted in sign (and colors), less visible and more brief in duration. The statistical proof of the existence of these patterns is provided by the ANOVA tests shown in Figure 3.20. Moreover, a consistently significant directional difference of de-synchronization is found in the right parieto-occipital region of the brain, suggesting that it could be the neural complex that is the most stimulated by the variation of the horizontal coordinates of the observed movement's target.
This analysis is sufficient to show the existence of longer-term time-locked mu-suppression behaviors, but it could be argued that due to the temporal averaging within the window of interest such analysis does not properly highlight short-lived features of the de-synchronization that are more noticeable by visual inspection. An example could be made observing the centro-parietal ROIs during window W2, where the de-synchronization linked to right-directed movements switches from the left hemisphere to the right one within the time interval, leaving the single left and right ROIs out of the set of statistically significant differences after the temporal average.

Regarding the vertical differentiation of mu-suppression patterns, by comparing the difference ranges of Figure 3.20 with the ones of the corresponding windows in Figure 3.21 it could be noticed that they are not as intense as in the horizontal case. Activity in the time interval between 0.5 and 1 second could still be attributed to CVSA during the preparation of the movement, but it does not match the patterns described by Worden et al. [70]. One pattern that could be seen as recurring both in the reaching movement and the movement back is the distribution of de-synchronization difference during the progression towards the destination, more evident by comparing the maps at 4 s (3) and 6 s (4). There, the downward movement elicits de-synchronization in contrast to the upward movement (positive/blue values in (3); negative/red in (4)) in the right-hemisphere parieto-occipital region, while for the upward in contrast to the downward (negative/red in (3); positive/blue values in (4)), de-synchronization occurs in the somatosensory cortex and in the left-hemisphere centro-parietal region. As for the horizontal case, the visually inferred conclusions are in agreement with the statistical analysis of Figure 3.21.

Conclusion

Putting all together, the first question this study was meant to answer is how the act of observing robotic movements with specific characteristics (center-out, target-directed) is encoded in neural activity measured with non-invasive electroencephalography. The second was if such activity could be used to improve the performance of the current state of the art in the active control of robotic devices through non-invasive EEG-based brain-computer interfaces.

The first point can be answered through the results of the event-related desynchronization, noticing that the behavior of brain regions excited by the observation of the movement in the alpha and beta bands is coherent with the well-known correlates of the task of Motor Observation from the literature. On top of that, there is a difference in the intensity and in the topographical distribution of mu-band brain activity elicited by movements that differ in direction, depending on the phase of the movement — preparation, onset, or progression. These findings support the conclusion that the mapping between an act of movement and the neural structures that process and encode its observation and their interactions is very complex and takes into account several variables, even when restricting to the movement class of upper-limb, center-out, and target-oriented robotic reaching movements.

Reconstructing such an intricate relationship is, as a matter of fact, the decoding process, approached in this study as a classification or regression task. The former type formalizes a more straightforward and simple mapping between the EEG measured during a trial, i.e. a reaching movement towards a target, and the target of the action. The latter induces a specific spatial information processing and encoding process in the neural ensembles through the observation of the movement of which it is the destination, as seen in the de-synchronization directional difference patterns. The provided evidence, comprising consistently above-chance level results, demonstrates the feasibility of reconstructing this connection. Additionally, it was shown that a non-negligible amount of data can be left out to focus on the informative subset represented by the low frequencies of the EEG. By downsampling the measured activity and using only the portion of the frequency spectrum lower than 5 Hz it is possible to implement significantly more efficient, fast and light systems, characteristics that are not to be despised in BCI applications. Being able to prove that this is feasible by limiting at the same time the loss of information is an important requirement: in this study, it was possible not only to prove that the decoding under these conditions was possible with above-chance results, but that the system could be made even more efficient by further restricting the already frequency-restricted input in the temporal domain too. This was done by showing the existence of favored time frames that, applied to the EEG of a trial, produce the best accuracy of classification. An application of these findings is in the possibility of designing a BCI system that decodes EEG measurements collected with an even low sampling rate, discards the unnecessary samples saving only the few that are included in the time window, and predicts the target of the movement observed during the recording exploiting the strictly necessary computational capabilities, and everything allowing overt eye movements.

A further step is done with the progress from a BCI based on a goal-selection protocol, as the aforementioned target-classification BCI, to one based on a process-control protocol. Implementing such a system required the design of a decoding component that could be able to reconstruct the more complex relationship between the measured electrophysiological activity and the continuous robotic movement as trajectories of position and velocity in the 2D workspace. Given from the literature that this is possible with the same low-frequency EEG used in classification, two novel algorithms were designed to improve the performance of current state-of-the-art EEG-to-kinematics decoding models under the constraints of data scarcity, jagged semi-discrete target trajectories, and moderate computational capabilities. This has surely more tangible applicability, as it allows the direct and fast decoding of the measured low-frequency EEG into the kinematic state of an observed hand translating in the 2D space, through simple and light models that reach qualitatively and quantitatively satisfying prediction performances.

At this point, one could argue that there could be limited usefulness of a BCI that only decodes passively observed movements from the non-invasive brain activity. As shown in Clanton [11] and Collinger et al. [13], building and training a model for the decoding of an observed motor task is the basis of an observation-based calibration phase, first step in the gradual introduction to the complete active control of a robotic device through brain activity. In each session, the model is trained through this process with few data as an initialization step for the successive re-training where the mixed active EEG control data is used. Therefore, having an initialized model that is already good enough to partly decode the brain's activity correlated to motor processing and planning represents an advantageous starting point for the construction of an efficient and accurate decoder system for the active control of robotic devices through non-invasive EEG BCI.

The findings of this study make space for a wide range of possible future studies for improving the adopted methods and protocols. For instance, one critical point of this study was the scarcity of data, which has been putting heavy constraints on the range of models and algorithms that could be exploited for the decoder. Considering that an experimental session of, on average, four hours was needed to obtain one hour of measurements, the future development of non-invasive EEG measurement systems that allow faster setup times could give a significant contribution to the quantity of data collected in a single experimental session. Moreover, the measurement time could be enlarged by changing or modifying the current experimental paradigm, trying to implement more trials or runs while keeping the subjects' focus high and fatigue low. Additionally, in this study, the analysis relied on pre-processing and processing pipelines that ensured obtaining trials of movement-observation-related EEG with little or no artifact residuals. This still required the subjects to force themselves to produce clean-enough signals and attain the eye-stressing eyeruns, which may have increased the subjects' fatigue level, leading to a decrease in the attention, and unavoidably, in the decoding performance. The development of future data processing techniques that, paired with more easy-of-use systems, could allow less strict and stressful measurement requirements, and may positively impact the quality and quantity of the collected data.

Regarding possible improvements in the decoding itself, some reasoning can be deduced from this study, possibly serving as inspiration for future works. Firstly, it is important to mention that the models that were implemented relied on hyperparameters whose values were fixed to obtain the best prediction performance under the constraints put by the temporal feasibility of the optimization process and the complexity of the model. We cannot rule out the possibility that better values for the hyperparameters exist and could be found with a more complete and refined search process, neither we can rule out that algorithms put aside from the digression for a too-poor performance could turn out to be outstandingly accurate after a change of structure and/or combination of hyperparameters.

Furthermore, the data scarcity also led to many algorithms and models (e.g., deep learning techniques) being put aside in favor of more lightweight designs. These were also employed for reasons of computational complexity, since using models with too long training time would have made infeasible processes with many training iterations such as the TWSS, CTS and RTS. It must be said that the high number of iterations was thought of as a strategy to resort the unavoidable training bias consequence of the scarcity of data, and solving the latter issue would automatically rule out the need for many training sessions. Consequently, by obtaining more motor-observation data, the time spent to obtain stable results with simple models trained with few data could be used to train fewer iterations of more complex models with possibly better predictive capabilities.

Lastly, in order to fully answer to the second focal point of the study, it would be necessary to test the results of the observation-based calibration applied as a step toward the complete neural control of the robotic device. In fact, these findings prove that it is possible to extract enough information related to the observation of a robotic movement from the EEG of an observer, but testing if such a principle could be applied in the said way would require the implementation of the active control part. With that, the subject could have a more gradual learning of the task by adding a "passive learning" step, and the decoder model, even of a more complex design, could benefit of the much bigger quantity of data from multiple sessions with several runs and different percentages of neural control, as in Clanton and Collinger et al. Hence, the relevance of this study rather lies in proving that the observation-based calibration used in invasive BCI systems to enhance the performance of the decoder model can be applied to non-invasive BCIs, since it is possible to extract enough information to build a decoder model using only that. Then, future studies could make a step further from these results in designing a BCI system for the active neural control of robotic device, based on the contribution and benefits of the Observation-based Calibration.

Bibliography

[1] P. Avanzini, M. Fabbri-Destro, R. Dalla Volta, E. Daprati, G. Rizzolatti, and G. Cantalupo. The Dynamics of Sensorimotor Cortical Oscillations during the Observation of Hand Movements: An EEG Study. *PLOS ONE*, 7(5):1–10, 2012.

[2] M. Billinger, I. Daly, V. Kaiser, J. Jin, B. Allison, G. Müller-Putz, and C. Brunner. *Is It Significant? Guidelines for Reporting BCI Performance.* 07 2012.

[3] T. J. Bradberry, R. J. Gentili, and J. L. Contreras-Vidal. Reconstructing Three-Dimensional Hand Movements from Noninvasive Electroencephalographic Signals. *Journal of Neuroscience*, 30(9):3432–3437, 2010.

[4] B. Brisson and P. Jolicœur. A psychological refractory period in access to visual short-term memory and the deployment of visual–spatial attention: Multitasking processing deficits revealed by event-related potentials. *Psychophysiology*, 44(2):323–333, 2007.

[5] J. D. Bronzino and D. R. Peterson. *The Biomedical Engineering Handbook: Four volume set.* CRC Press, 2018.

[6] G. Buccino, F. Binkofski, G. R. Fink, L. Fadiga, L. Fogassi, V. Gallese, R. J. Seitz, K. Zilles, G. Rizzolatti, and H.-J. Freund. Action observation activates premotor

and parietal areas in a somatotopic manner: an fMRI study. *European Journal of Neuroscience*, 13(2):400–404, 2001.

[7] G. Buzsaki. *Rhythms of the brain.* Oxford University Press, U.S.A., Oxford ; New York, 1 edition, 2011.

[8] G. Buzsáki. Large-scale recording of neuronal ensembles. *Nature neuroscience*, 7:446–51, 2004.

[9] A. Casson, D. Yates, S. Smith, J. Duncan, and E. Rodriguez-Villegas. Wearable Electroencephalography. *Engineering in Medicine and Biology Magazine, IEEE*, 29:44 – 56, 2010.

[10] R. Chavarriaga, A. Sobolewski, and J. d. R. Millán. Errare machinale est: the use of error-related potentials in brain-machine interfaces. *Frontiers in Neuroscience*, 8, 2014.

[11] S. T. Clanton. Brain-Computer Interface Control of an Anthropomorphic Robotic Arm. 2011.

[12] D. Coch, W. Skendzel, and H. J. Neville. Auditory and visual refractory period effects in children and adults: An ERP study. *Clinical Neurophysiology*, 116(9):2184–2203, 2005.

[13] J. L. Collinger, B. Wodlinger, J. E. Downey, W. Wang, E. C. Tyler-Kabara, D. J. Weber, A. J. McMorland, M. Velliste, M. L. Boninger, and A. B. Schwartz. High-performance neuroprosthetic control by an individual with tetraplegia. *The Lancet*, 381(9866):557–564, 2013.

[14] C. Cortes and V. N. Vapnik. Support-Vector Networks. *Machine Learning*, 20:273–297, 1995.

[15] G. Di Flumeri, P. Aricò, G. Borghini, N. Sciaraffa, A. Di Florio, and F. Babiloni. The Dry Revolution: Evaluation of Three Different EEG Dry Electrode Types in Terms of Signal Spectral Features, Mental States Classification and Usability. *Sensors*, 19(6), 2019.

[16] L. Farwell and E. Donchin. Talking off the top of your head: toward a mental prosthesis utilizing event-related brain potentials. *Electroencephalography and Clinical Neurophysiology*, 70(6):510–523, 1988.

[17] S. Frenkel-Toledo, S. Bentin, A. Perry, D. G. Liebermann, and N. Soroker. Dynamics of the EEG power in the frequency and spatial domains during observation and execution of manual movements. *Brain Research*, 1509:43–57, 2013.

[18] K. Goel, V. Pek, N. A. Shlobin, J.-S. Chen, A. Wang, G. M. Ibrahim, A. Hadjinicolaou, K. Roessler, R. W. Dudley, D. K. Nguyen, R. El-Tahry, A. Fallah, and A. G. Weil. Clinical utility of intraoperative electrocorticography for epilepsy surgery: A systematic review and meta-analysis. *Epilepsia*, 64(2):253–265, 2023.

[19] T. Hastie, R. Tibshirani, and J. Friedman. *The Elements of Statistical Learning.* Springer Series in Statistics. Springer New York Inc., New York, NY, USA, 2001.

[20] G. L. Holmes and R. Khazipov. Basic Neurophysiology and the Cortical Basis of EEG. pages 19–33, 2007.

[21] K. M. Hossain, M. A. Islam, S. Hossain, A. Nijholt, and M. A. R. Ahad. Status of deep learning for EEG-based brain–computer interface applications. *Frontiers in Computational Neuroscience*, 16, 2023.

[22] I. Iturrate, L. Montesano, and J. Minguez. Task-Dependent Signal Variations in EEG Error-Related Potentials for Brain-Computer Interfaces. *Journal of Neural Engineering*, 10(2):026024, 2013.

[23] T. Kaufmann, S. M. Schulz, C. Grünzinger, and A. Kübler. Flashing characters with famous faces improves ERP-based brain–computer interface performance. *Journal of Neural Engineering*, 8:056016, 2011.

[24] R. Kobler, A.-I. Sburlea, and G. Müller-Putz. Tuning characteristics of low-frequency EEG to positions and velocities in visuomotor and oculomotor tracking tasks. *Scientific Reports*, 8, 2018.

[25] R. J. Kobler, A. I. Sburlea, C. Lopes-Dias, A. Schwarz, M. Hirata, and G. R. Müller-Putz. Corneo-retinal-dipole and eyelid-related eye artifacts can be corrected offline and online in electroencephalographic and magnetoencephalographic signals. *NeuroImage*, 218:117000, 2020.

[26] R. J. Kobler, A. I. Sburlea, V. Mondini, M. Hirata, and G. R. Müller-Putz. Distance- and speed-informed kinematics decoding improves M/EEG based upper-limb movement decoder accuracy. *Journal of Neural Engineering*, 17(5):056027, 2020.

[27] R. J. Kobler, A. I. Sburlea, V. Mondini, and G. R. Müller-Putz. HEAR to remove pops and drifts: the high-variance electrode artifact removal (HEAR) algorithm, 2019.

[28] R. J. Kobler, A. I. Sburlea, and G. R. Müller-Putz. A Comparison of ocular Artifact removal Methods for Block Design based Electroencephalography Experiments. In *GBCIC*, 2017.

[29] A. Kreilinger, H. Hiebel, and G. R. Müller-Putz. Single Versus Multiple Events Error Potential Detection in a BCI-Controlled Car Game With Continuous and Discrete Feedback. *IEEE Transactions on Biomedical Engineering*, 63(3):519–529, 2016.

[30] M. Lambooij, W. Ijsselsteijn, M. Fortuin, and I. Heynderickx. Visual Discomfort and Visual Fatigue of Stereoscopic Displays: A Review. *Journal of Imaging Science and Technology - J IMAGING SCI TECHNOL*, 53, 2009.

[31] O. Ledoit and M. Wolf. A well-conditioned estimator for large-dimensional covariance matrices. *Journal of Multivariate Analysis*, 88(2):365–411, 2004.

[32] B. Li, T. Cheng, and Z. Guo. A review of EEG acquisition, processing and application, journal = Journal of Physics: Conference Series. 1907(1):012045, 2021.

[33] F. Lotte, L. Bougrain, A. Cichocki, M. Clerc, M. Congedo, A. Rakotomamonjy, and F. Yger. A review of classification algorithms for EEG-based brain–computer interfaces: a 10 year update. *Journal of Neural Engineering*, 15(3):031005, 2018.

[34] T.-j. Luo, J. Lv, F. Chao, and C. Zhou. Effect of Different Movement Speed Modes on Human Action Observation: An EEG Study. *Frontiers in Neuroscience*, 12, 2018.

[35] E. López-Larraz, L. Montesano, A. Gil-Agudo, and J. Minguez. Continuous decoding of movement intention of upper limb self-initiated analytic movements from pre-movement EEG correlates. *Journal of neuroengineering and rehabilitation*, 11:153, 2014.

[36] V. Martínez-Cagigal, R. J. Kobler, V. Mondini, R. Hornero, and G. R. Muller-Putz. Non-linear online low-frequency EEG decoding of arm movements during a pursuit tracking task. In *2020 42nd Annual International Conference of the IEEE Engineering in Medicine Biology Society (EMBC)*, pages 2981–2985, 2020.

[37] C. M. Michel, M. M. Murray, G. Lantz, S. Gonzalez, L. Spinelli, and R. Grave de Peralta. EEG source imaging. *Clinical Neurophysiology*, 115(10):2195–2222, 2004.

[38] V. Mondini, R. J. Kobler, A. I. Sburlea, and G. R. Müller-Putz. Continuous low-frequency EEG decoding of arm movement for closed-loop, natural control of a robotic arm. *Journal of Neural Engineering*, 17(4):046031, 2020.

[39] S. D. Muthukumaraswamy, B. W. Johnson, and N. A. McNair. Mu rhythm modulation during observation of an object-directed grasp. *Cognitive Brain Research*, 19(2):195–201, 2004.

[40] G. R. Müller-Putz. Chapter 18 - Electroencephalography. In N. F. Ramsey and J. del R. Millán, editors, *Brain-Computer Interfaces*, volume 168 of *Handbook of Clinical Neurology*, pages 249–262. Elsevier, 2020.

[41] G. R. Müller-Putz, R. J. Kobler, J. Pereira, C. Lopes-Dias, L. Hehenberger, V. Mondini, V. Martínez-Cagigal, N. Srisrisawang, H. Pulferer, L. Batistić, and A. I. Sburlea. Feel Your Reach: An EEG-Based Framework to Continuously Detect Goal-Directed Movements and Error Processing to Gate Kinesthetic Feedback Informed Artificial Arm Control. *Frontiers in Human Neuroscience*, 16, 2022.

[42] B. Obermaier, G. Muller, and G. Pfurtscheller. "Virtual keyboard" controlled by spontaneous EEG activity. *IEEE Transactions on Neural Systems and Rehabilitation Engineering*, 11(4):422–426, 2003.

[43] L. Oberman, J. Mccleery, V. Ramachandran, and J. Pineda. EEG evidence for mirror neuron activity during the observation of human and robot actions: Toward an analysis of the human qualities of interactive robots. *Neurocomputing*, 70:2194–2203, 2007.

[44] P. Ofner and G. R. Müller-Putz. Decoding of velocities and positions of 3D arm movement from EEG. In *2012 Annual International Conference of the IEEE Engineering in Medicine and Biology Society*, pages 6406–6409, 2012.

[45] R. Oshana. 4 - Overview of Digital Signal Processing Algorithms. In R. Oshana, editor, *DSP Software Development Techniques for Embedded and Real-Time Systems*, Embedded Technology, pages 59–121. Newnes, Burlington, 2006.

[46] H. Pang, T. Tong, and H. Zhao. Shrinkage-Based Diagonal Discriminant Analysis and Its Applications in High-Dimensional Data. *Biometrics*, 65(4):1021–1029, 2009.

[47] J. Pereira, R. Kobler, P. Ofner, A. Schwarz, and G. R. Müller-Putz. Online detection of movement during natural and self-initiated reach-and-grasp actions from EEG signals. *Journal of Neural Engineering*, 18(4):046095, 2021.

[48] J. Pereira, P. Ofner, A. Schwarz, A.-I. Sburlea, and G. Müller-Putz. EEG neural correlates of goal-directed movement intention. *NeuroImage*, 149, 01 2017.

[49] G. Pfurtscheller, C. Neuper, G. Muller, B. Obermaier, G. Krausz, A. Schlogl, R. Scherer, B. Graimann, C. Keinrath, D. Skliris, M. Wortz, G. Supp, and C. Schrank. Graz-BCI: state of the art and clinical applications. *IEEE Transactions on Neural Systems and Rehabilitation Engineering*, 11(2):1–4, 2003.

[50] J. A. Pineda. The functional significance of mu rhythms: Translating “seeing” and “hearing” into “doing”. *Brain Research Reviews*, 50(1):57–68, 2005.

[51] M. Ploner, J. Gross, L. Timmermann, B. Pollok, and A. Schnitzler. Pain Suppresses Spontaneous Brain Rhythms. *Cerebral Cortex*, 16(4):537–540, 2005.

[52] H. Pulferer, B. Ásgeirsdóttir, V. Mondini, A.-I. Sburlea, and G. Müller-Putz. Learning effects in 2D trajectory inference from low-frequency EEG signals over multiple feedback sessions. 09 2021.

[53] H. S. Pulferer, B. Ásgeirsdóttir, V. Mondini, A. I. Sburlea, and G. R. Müller-Putz. Continuous 2D trajectory decoding from attempted movement: across-session performance in able-bodied and feasibility in a spinal cord injured participant. *Journal of Neural Engineering*, 19(3):036005, may 2022.

[54] Y. Sasaki. The truth of the F-measure. *Teach Tutor Mater*, 01 2007.

[55] R. Scherer, F. Lee, A. Schlogl, R. Leeb, H. Bischof, and G. Pfurtscheller. Toward Self-Paced Brain–Computer Communication: Navigation Through Virtual Worlds. *IEEE Transactions on Biomedical Engineering*, 55(2):675–682, 2008.

[56] A. Schlögl, C. Keinrath, D. Zimmermann, R. Scherer, R. Leeb, and G. Pfurtscheller. A fully automated correction method of EOG artifacts in EEG recordings. *Clinical Neurophysiology*, 118(1):98–104, 2007.

[57] E. W. Sellers and E. Donchin. A P300-based brain–computer interface: Initial tests by ALS patients. *Clinical Neurophysiology*, 117(3):538–548, 2006.

[58] A. J. Smola and B. Schölkopf. A tutorial on support vector regression. *Statistics and computing*, 14(3):199–222, 2004.

[59] R. Srinivasan, D. Tucker, and M. Murias. Estimating the spatial Nyquist of the human EEG. *Behavior Research Methods*, 30:8–19, 1998.

[60] D. Steyrl, R. Scherer, O. Förstner, and G. Müller-Putz. Motor Imagery Brain-Computer Interfaces: Random Forests vs Regularized LDA - Non-linear Beats Linear. In *Proceedings of the 6th International Brain-Computer Interface Conference Graz 2014*, pages 061–1–061–4. Verlag der Technischen Universität Graz, 2014.

[61] M. Teplan. Fundamental of EEG Measurement. *MEASUREMENT SCIENCE REVIEW*, 2, 2002.

[62] L. Tonin, R. Leeb, A. Sobolewski, and J. del R Millán. An online EEG BCI based on covert visuospatial attention in absence of exogenous stimulation. *Journal of Neural Engineering*, 10(5):056007, 2013.

[63] S. Tortora, A. Gottardi, E. Menegatti, and L. Tonin. Continuous Teleoperation of a Robotic Manipulator via Brain-Machine Interface with Shared Control. In *2022 IEEE 27th International Conference on Emerging Technologies and Factory Automation (ETFA)*, pages 1–8, 2022.

[64] B. Urgen, M. Plank, H. Ishiguro, H. Poizner, and A. Saygin. EEG theta and Mu oscillations during perception of human and robot actions. *Frontiers in Neurorobotics*, 7, 2013.

[65] V. N. Vapnik. *The nature of statistical learning theory.* Springer-Verlag New York, Inc., 1995.

[66] M. Velliste, S. Perel, S. Perel, M. C. Spalding, M. C. Spalding, A. S. Whitford, A. S. Whitford, and A. B. Schwartz. Cortical control of a prosthetic arm for self-feeding. *Nature*, 453(7198):1098–1101, 2008.

[67] S. Waldert, H. Preissl, E. Demandt, C. Braun, N. Birbaumer, A. Aertsen, and C. Mehring. Hand Movement Direction Decoded from MEG and EEG . *Journal of Neuroscience*, 28(4):1000–1008, 2008.

[68] J. Wolpaw, N. Birbaumer, W. Heetderks, D. McFarland, P. Peckham, G. Schalk, E. Donchin, L. Quatrano, C. Robinson, and T. Vaughan. Brain-computer interface technology: a review of the first international meeting. *IEEE Transactions on Rehabilitation Engineering*, 8(2):164–173, 2000.

[69] J. R. Wolpaw, J. del R. Millán, and N. F. Ramsey. Chapter 2 - Brain-computer interfaces: Definitions and principles. In N. F. Ramsey and J. del R. Millán, editors, *Brain-Computer Interfaces*, volume 168 of *Handbook of Clinical Neurology*, pages 15–23. Elsevier, 2020.

[70] M. S. Worden, J. J. Foxe, N. Wang, and G. V. Simpson. Anticipatory Biasing of Visuospatial Attention Indexed by Retinotopically Specific -Bank Electroencephalography Increases over Occipital Cortex. *Journal of Neuroscience*, 20(6):RC63–RC63, 2000.

Acknowledgments

Il primo ringraziamento va ai miei genitori, per i sacrifici che avete fatto e che non ho mai dato per scontato. Grazie per avermi permesso di arrivare fino a qui, dandomi sempre il sostegno di cui avevo bisogno e credendo sempre in me.

Ringrazio le persone che ci sono sempre state per me durante buona parte di questo percorso: grazie a Miriam per essere al mio fianco, per condividere con me pensieri, paure ed emozioni, e per esserci sempre quando ne ho bisogno. Grazie a Diego e Andrea, per il tempo passato insieme, per le birre e le risate, per essere miei amici.

Ringrazio il Prof. Tonin per avermi permesso di vivere l'esperienza di Graz e di lavorare a questo progetto, per la sua supervisione e per essere stato sempre gentile e disponibile.

Thanks to the team of the Institute of Neural Engineering of TU Graz, for the amazing experience I had there, for the time spent together and the advices you gave me. Thank to Prof. Müller-Putz for making this possible, and to Kyriaki for assisting me in the development of this study. Thank to all the people who dedicated their time to participate in the experiment with only my gratitude as a reward, it meant a lot to me.